Photochemical Processes in the Atmospheres of Earth and Mars

Thesis by

Hari Nair

In Partial Fulfillment of the Requirements
for the Degree of
Doctor of Philosophy

California Institute of Technology
Pasadena, California

1996
(defended January 22, 1996)

Acknowledgments

All right, now we come to the fun (?) part of writing this thesis. First of all, I'd like to thank my thesis advisor, Yuk Yung, for all of his creativity, good nature, and humor over the years. Thanks to Mark Allen, too, for his guidance, editorial advice (the phrase "didactic gem" comes to mind), and the many conversations we've had while I've been here. Other faculty around the division I'm happy to have known are Andy Ingersoll, for sending me to Hawaii my first year (mahalo!!!), and for opening his home for picnics and Thanksgiving dinner, Dave Stevenson, for the annual backpacking expeditions, Jim Westphal, for showing off all of his nifty little gadgets, and Dewey Muhleman, for teaching all those great classes that I never failed to take. Except maybe once or twice. Kay Campbell and Irma Betters were always very helpful in guiding me around this maze that is Caltech. And of course, I've got to thank all the other people whose paths have crossed mine in the time I've been here. You know, I started to make a list of names, but it got pretty long, so I'll offend you all equally and just say thanks for making it memorable and fun. And I actually got to meet people outside Caltech (yes, it is possible!). Thanks to all of the wonderful folks at Los Angeles Theatresports for welcoming me into the family, even though we all know I have the acting skills of a turnip.

But most of all, I'd like to express my gratitude to my family, for bringing this screwball kid into the world in the first place, and for keeping me interested in whatever I was into at the time. I am who I am because of your love and encouragement.

Abstract

This thesis consists of two chapters concerning photochemical processes in the atmospheres of earth and Mars. The first chapter is a comprehensive study of the photochemistry of the martian atmosphere. Classical models of the Mars atmosphere have neglected an important property of carbon dioxide, namely that the photoabsorption cross section decreases with lower temperature. Accounting for this effect yields a smaller photolysis rate for CO_2 and more importantly, an enhanced photolysis rate for water vapor. Both effects combine to yield carbon monoxide mixing ratios smaller by a factor of four than observations indicate. We propose modifications in the rate coefficients for two key reactions, $CO + OH$ and $OH + HO_2$, in order to resolve this discrepancy. We note that similar revisions have been proposed to reconcile models and observations of ozone in the terrestrial mesosphere. Other investigators have proposed a heterogeneous sink of odd hydrogen radicals on aerosols; we find that such a sink is unnecessary. Finally, we have performed the first time dependent calculation to examine the mechanism by which the escape of atomic oxygen controls the escape flux of hydrogen from the atmosphere. We show that this coupling operates over a time scale of 10^5 years.

In chapter two we investigate the formation and evolution of low ozone anomalies in the northern winter stratosphere using a Lagrangian photochemical model. The UARS spacecraft has observed pockets of low ozone in the 6 to 10 millibar altitude range, where the effects of dynamics and chemistry on the ozone budget are comparable. We employ the Lagrangian model to compute the ozone loss rate within an isolated parcel of air as it travels along a specified trajectory. Since we have decoupled the dynamics and chemistry, disagreement between the model and observations should reflect deficiencies in the chemistry. We find that the model consistently overestimates the ozone loss rate above about 7 millibars altitude, which is a common feature of most current photochemical models. Below 10 millibars altitude, the model is in good agreement with the observations, indicating that the description of chemistry is valid in the low to mid stratosphere.

Table of Contents

List of Figures

Paper I:

Paper II:

List of Tables

Paper I:

Paper II:

A Photochemical Model of the Martian Atmosphere

Hari Nair, Mark Allen†, Ariel D. Anbar, and Yuk L. Yung

Division of Geological and Planetary Sciences
California Institute of Technology
Pasadena, CA 91125

and

R. Todd Clancy

Space Science Institute, Suite 294
1234 Innovation Drive
Boulder, Colorado 80303

Published in modified form in *Icarus*, **111**, 124–150 (1994).

†Also at Earth and Space Sciences Division, Jet Propulsion Laboratory, California Institute of Technology, Pasadena, California 91109.

Contribution number 5336 from the Division of Geological and Planetary Sciences, California Institute of Technology.

Abstract

The factors governing the amounts of CO, O_2, and O_3 in the martian atmosphere are investigated using a minimally constrained, one-dimensional photochemical model. We find that the incorporation of temperature dependent CO_2 absorption cross sections leads to an enhancement in the water photolysis rate, increasing the abundance of OH radicals to the point where the model CO abundance is smaller than observed. Good agreement between models and observations of CO, O_2, O_3, and the escape flux of atomic hydrogen can be achieved, using only gas phase chemistry, by varying the recommended rate constants for the reactions CO + OH and OH + HO_2 within their specified uncertainties. Similar revisions have been suggested to resolve discrepancies between models and observations of the terrestrial mesosphere.

We have performed the first time dependent relaxation calculation to examine the mechanism by which the rate of atomic oxygen escape regulates the hydrogen escape flux and found the timescale for this phenomenon to be on the order of 10^5 years, in agreement with previous estimates. The oxygen escape flux inferred from the observed atomic hydrogen escape is much larger than the expected exospheric escape rate for oxygen. Weathering of the surface may account for the imbalance. Quantification of the escape rates of oxygen and hydrogen from Mars is a worthwhile objective for an upcoming martian upper atmospheric mission.

We also consider the possibility that HO_x radicals may be catalytically destroyed on dust grains suspended in the atmosphere. Good agreement with the observed CO mixing ratio can be achieved via this mechanism, but the resulting ozone column is much higher than the observed quantity. We feel that there is no need to invoke heterogeneous processes to reconcile models and observations at this time.

1. Introduction

The primary constituent of the martian atmosphere is CO_2, which comprises $\sim 95\%$ of the atmosphere (Owen *et al.* 1977). Carbon dioxide is photolyzed by solar ultraviolet light shortward of 2275 Å into carbon monoxide and atomic oxygen:

$$CO_2 + h\nu \;\rightarrow\; CO + O.$$

Since the recombination of CO and O is negligibly slow compared to the combination of O atoms to form O_2, the expected result is that the martian atmosphere should contain significant amounts of CO and O_2, in the ratio 2:1. However, measurements of the atmosphere have revealed a composition quite different from these initial predictions. For more than two decades, atmospheric modelers have sought to explain the observed composition, but good simulations have been achieved only with the adoption of key simplifying assumptions. It is the goal of this paper to present a self-consistent model of martian atmospheric chemistry that can reproduce modern measurements with a minimal number of imposed constraints on the calculated results.

That the martian atmosphere contains only trace amounts of CO and O_2 became clear when Kaplan *et al.* (1969) originally detected CO in a mixing ratio of only $(8 \pm 3) \times 10^{-4}$. This was confirmed by later observations, including the recent measurements of Clancy *et al.* (1990) and Lellouch *et al.* (1991). The detection of molecular oxygen, first by Barker (1972) with a column abundance of 9.5 ± 0.6 cm-amagat (1 cm-amagat $= 2.69 \times 10^{19}$ cm^{-2}) and later by Carleton and Traub (1972; 10.4 ± 1.0 cm-amagat) and Trauger and Lunine (1983; 8.5 cm-amagat), yields mixing ratios of $1.0 - 1.2 \times 10^{-3}$, for a CO_2 column abundance of 83 m-amagat. The measured CO/O_2 ratio hence is less than one.

Thus the outstanding problem in martian photochemistry is to explain the apparent stability of the CO_2 atmosphere in light of the slow direct recombination of CO and O. This problem was considered to be resolved by the classic papers of McElroy and Donahue (1972) and Parkinson and Hunten (1972). Briefly, the radical species H, OH, and HO_2 – collectively known as odd hydrogen or HO_x – produced either via photolysis of water vapor or reaction of electronically excited $O(^1D)$ atoms with H_2 or H_2O, catalyze the recombination of CO and O as follows:

$$\begin{array}{rrcl} & H + O_2 + M & \rightarrow & HO_2 + M \\ & O + HO_2 & \rightarrow & OH + O_2 \\ & CO + OH & \rightarrow & CO_2 + H \\ \hline \text{net} & CO + O & \rightarrow & CO_2 \end{array} \qquad \begin{array}{rcl} H + O_3 & \rightarrow & OH + O_2 \\ O + O_2 + M & \rightarrow & O_3 + M \\ CO + OH & \rightarrow & CO_2 + H \\ \hline CO + O & \rightarrow & CO_2 \end{array}$$

(McElroy and Donahue 1972) and

$$\begin{array}{rrcl} & 2\,(H + O_2 + M & \rightarrow & HO_2 + M) \\ & HO_2 + HO_2 & \rightarrow & H_2O_2 + O_2 \\ & H_2O_2 + h\nu & \rightarrow & OH + OH \\ & 2\,(CO + OH & \rightarrow & CO_2 + H) \\ \hline \text{net} & 2\,CO + O_2 & \rightarrow & 2\,CO_2 \end{array}$$

(Parkinson and Hunten 1972). However, neither of these models provides an entirely satisfactory production mechanism for the OH radical. The McElroy and Donahue model requires very large eddy diffusion coefficients in order to rapidly transport O atoms downward to react with HO_2. Their eddy diffusivity coefficients are on the order of 10^8 cm^2 s^{-1}, far higher than the values of $10^5 - 10^6$ cm^2 s^{-1} inferred for similar pressure levels in the terrestrial atmosphere (e.g., Allen *et al.* 1981, Strobel *et al.* 1987, Bevilacqua *et al.* 1990). Furthermore, analyses of dust and ice hazes in the atmosphere indicate eddy diffusion coefficients also on the order of $10^5 - 10^6$ cm^2 s^{-1} (e.g., Chassefière *et al.* 1992, Korablev *et al.* 1993a). On the other hand, the Parkinson and Hunten model employs a more moderate eddy diffusivity profile, but requires a globally averaged water abundance two to three times the observed mean water abundance (Atreya and Gu, 1994) in order to produce enough H_2O_2 to serve as a source of OH.

In the aforementioned papers, and others also examining the CO_2 stability problem (e.g., Liu and Donahue 1976, Kong and McElroy 1977a, Izakov and Krasitskii 1977), the CO_2 photodissociation cross section values were assumed to be independent of the atmospheric temperature. However, as first shown by DeMore and Patapoff (1972) and later by Lewis and Carver (1983) over a wider wavelength and temperature range, these cross sections decrease significantly with decreasing temperature, with up to an order of magnitude change from ~ 370 to $\sim 200\,\mathrm{K}$ longward of ~ 1750 Å. DeMore and Patapoff suggested that their results should have a significant impact on martian photochemical calculations. Since CO_2 is the dominant opacity source in the region of the spectrum where H_2O is dissociated, decreasing the CO_2 cross section leads to an increase in the photolysis rate of water vapor. Parisot and Zucconi (1984) estimated a factor of ten increase in the H_2O photolysis rate when the temperature dependence of the CO_2 absorptivity is incorporated, based on the extrapolation of the DeMore and Patapoff data to longer wavelengths.

Shimazaki and Shimuzu (1979), Shimazaki (1981), and Shimazaki (1989) accounted for the temperature dependence of the CO_2 cross section by dividing the photodissociation coefficient by a factor of two, as suggested by DeMore and Patapoff (1972). Shimazaki (1989) found that the equilibrium abundance of CO in his model could only be increased to match observations by decreasing the assumed atmospheric H_2O profile. However, it was only recently when Anbar *et al.* (1993a) examined the implications of the Lewis and Carver CO_2 cross section measurements on calculated photodissociation rate coefficients that a direct connection was made between the CO_2 stability issue and the temperature dependent CO_2 cross sections. In the current work, the photochemical calculations incorporate the most recent CO_2 cross section measurements.

Krasnopolsky (1991), Nair *et al.* (1991, 1992), Allen *et al.* (1993), Krasnopolsky (1993b), and Atreya and Gu (1994) presented models incorporating the temperature dependent cross sections of Lewis and Carver, all agreeing that the predicted CO amounts were too low in the models. The preferred model of Krasnopolsky (1993b) included nitrogen and sulfur chemistry, reduced photodissociation cross sections for water vapor, and the inclusion of a sink of HO_x radicals on aerosol surfaces to bring the model results into better agreement with the observations. Atreya and Gu (1994) also suggested that the incorporation of heterogeneous reactions in the model may be necessary to balance the production and loss rates of CO_2. Alternatively, Nair *et al.* (1992) and Allen *et al.* (1993) proposed that limited changes in key rate coefficients may be sufficient to allow a purely gas phase model to reproduce the observations. One of the objectives of this paper is to expand on this possibility.

A related problem in the photochemistry of the martian atmosphere is that the CO/O_2 ratio is ~ 0.6, rather than 2, as expected for photolysis products from CO_2. The resolution lies in the requirement for a steady-state atmosphere that the elemental escape fluxes of hydrogen and oxygen, in the absence of surface interactions, are in the ratio 2:1, the stoichiometric ratio found in the water molecule (McElroy 1972). McElroy further suggested that the relative abundances of O_2 and CO adjust themselves such that the hydrogen and oxygen escape fluxes are always in a 2:1 ratio. This mechanism will be discussed in detail in a later section.

The abundances of CO and O_2 are regulated by the concentrations of odd hydrogen radicals, which are in turn heavily dependent upon the total amount and vertical distribution of water. The column water vapor abundance is a variable function of latitude and season. Typical amounts observed during the Viking era were ~ 10 precipitable μm (Jakosky and Farmer 1982), where 1 pr. $\mu\mathrm{m} = 3.34 \times 10^{18}\ \mathrm{cm}^{-2}$. Early photochemical models often concentrated the bulk of the atmospheric water into the first 10 km above the surface (e.g., Liu and Donahue 1976, Kong and McElroy 1977a). High values of the eddy diffusion coefficient were required in order to bring atomic oxygen down to react with HO_2 before large amounts of O_2 were able to form. More recent photochemical models have assumed a more uniformly mixed water profile to higher altitudes (e.g., Krasnopolsky and Parshev 1979, Shimazaki 1989, Kranopolsky 1993b, Atreya and Gu 1994). More moderate values of the eddy diffusion coefficient on the order of $10^6\,\mathrm{cm}^2\,\mathrm{s}^{-1}$ were found to be satisfactory in this case. Post Viking studies of the vertical profile of water vapor suggest that water is uniformly mixed in the lower 10 to 30 km of the atmosphere and then drops rapidly above the altitude at which condensation first occurs (Jakosky 1985). Observations of the vertical distribution of water vapor by the *Phobos 2* spacecraft (Krasnopolsky *et al.* 1991), as well as by the Very Large Array (Clancy *et al.* 1992, Grossman *et al.* 1993, Clancy *et al.* 1993) support this argument.

The ozone density is directly related to the abundance of HO_x radicals. Odd oxygen, defined here as the family containing O and O_3, is rapidly destroyed by HO_x in reactions such as

$$\begin{aligned} O_3 + H &\rightarrow O_2 + OH \\ O + HO_2 &\rightarrow O_2 + OH \\ O + OH &\rightarrow O_2 + H. \end{aligned}$$

Since O and O_3 rapidly interconvert during the martian day, the ozone abundance is anticorrelated with the water abundance. Mariner 9 observations indicated an ozone amount below the detection limit of $3\,\mu\mathrm{m} - \mathrm{amagat}$ ($1\ \mu\mathrm{m} - \mathrm{amagat} = 2.69 \times 10^{15}$ $\mathrm{cm}^{-2} = 0.1\,\mathrm{Dobson\ Unit}$) over the northern polar cap during the summer (Barth *et al.* 1973), when Viking orbiter measurements of the water column amount in the atmosphere showed that water vapor was at a maximum (Jakosky and Farmer 1982). During northern winter, Mariner 9 measured an ozone column abundance as large as $57\,\mu\mathrm{m} - \mathrm{amagat}$ and Viking found that water fell to very low levels.

Model simulations of O_3 observations are quite sensitive to assumptions about atmospheric water levels. For example, the *Mars 5* spacecraft reported a value of $\sim 10^{10}$ cm^{-3} close to 40 km altitude at the morning terminator and a value three times less at the evening terminator (Krasnopolsky *et al.* 1977). To account for this high ozone density, Shimazaki (1981) suggested that a low amount of water vapor in the atmosphere, possibly due to cold temperatures, was the cause for the ozone peak. Rodrigo (1990) employed a water profile that was severely undersaturated in the middle atmosphere, and found model nighttime ozone amounts in agreement with the *Mars 5* measurements. More recently, Blamont and Chassefière (1993) presented vertical profiles of ozone detected by the *Phobos 2* orbiter at local sunset, which indicated a peak value of $\sim 10^8$ cm^{-3} s^{-1} around 42-45 km altitude, far smaller than the *Mars 5* measurements. They were able to match this observation by using larger water amounts than those employed by Rodrigo *et al.* (1990). Measurements at other times failed to detect any ozone, which Blamont and Chassefière (1993) suggested was due to a warmer and more humid atmosphere.

Simultaneous measurements of ozone and water are thereby extremely useful in constraining the abundance of HO_x species and, when combined with near simultaneously observed CO abundances, provide an excellent test of model simulations of martian atmospheric chemistry. For comparison with our photochemical model results, we shall adopt the two sets of measurements detailed in Table I, each set consisting of observations of H_2O, CO, and O_3 obtained at the same epoch, along with an O_2 mixing ratio of $(1.2 \pm 0.2) \times 10^{-3}$, assumed to be constant with time. A fourth quantity to be matched is the atomic hydrogen escape flux of 1.8×10^8 cm^{-2} s^{-1} as determined by Anderson and Hord (1971) from Mariner Lyman-α dayglow observations.

The ideal atmospheric model should have few imposed conditions on the calculated results to minimize the possibility that the results do not simply reflect the

Table I
Observed abundances of H_2O, CO, O_2, and O_3

Date	L_s (°)	$\int[H_2O]\,dz$ (pr. μm)	f_{CO} ($\times 10^4$)	f_{O_2} ($\times 10^3$)	$\int[O_3]\,dz$ (μm – amagat)
				1.2 ± 0.2^a	
6/88	207	8.8 ± 1^b	6 ± 1.5^c		1.5 ± 0.5^d
12/90	345	3.0 ± 0.8^e	8 ± 1.5^f		$\leq 2^f$

f denotes mixing ratio and $\int[\,]\,dz$ denotes column density. One pr. μm is equivalent to a column density of 3.34×10^{18} cm^{-2}. One μm – amagat is equivalent to a column density of 2.69×10^{15} cm^{-2}.
[a] Barker (1972) ($314° \leq L_s \leq 351°$), Carleton and Traub (1972) ($298° \leq L_s \leq 11°$), Owen *et al.* (1977) ($100° \leq L_s \leq 120°$), Trauger and Lunine (1983) ($L_s = 93°$)
[b] Rizk *et al.* (1991)
[c] Clancy *et al.* (1990); obtained 11/88 at $L_s = 305°$
[d] Espenak *et al.* (1991)
[e] Clancy *et al.* (1992)
[f] R.T. Clancy, private communication

initial assumptions. A traditional atmospheric chemistry model does require some description of the buffering of the near-surface abundances of CO_2 and H_2O, the escape of species from the atmosphere, and condensation of water vapor in the cold lower atmosphere. However, nearly all previously published models of martian atmospheric photochemistry have additionally prescribed one or more of the following parameters: the vertical distribution of CO_2, CO, O_2, H_2O above the condensation level, HO_x, or the mixing ratios of photochemically derived species at the surface. Only if heterogeneous surface chemistry controlled the atmospheric abundances would prescribing the surface concentrations be valid; there is no evidence at this time that such is the case for any of these species, although this assumption will be addressed in a later section. Some model calculations have prescribed close to the minimal set of conditions, including Izakov and Krasitskii (1977) and Shimazaki (1989). In the latter work, the observed CO abundance was not reproduced unless unreasonably low water amounts were assumed. In the present work, we will show how a minimally constrained photochemical model can reproduce available observations.

Over the past decade, there have been significant revisions in the measured reaction rate coefficients for chemical processes important in the terrestrial middle atmosphere (see most recently DeMore *et al.* 1992). Thus it is of value to critically reexamine martian photochemistry in the context of the revised rate coefficients, the temperature dependence of the CO_2 cross section, and the near simultaneous observations of carbon monoxide, ozone and water. The possible role of heterogeneous chemistry will also be considered.

2. The photochemical model

We have employed a one-dimensional photochemical model similar to that used by Yung *et al.* (1988) to study the photochemistry of HDO on Mars. The Caltech/JPL photochemical model solves the one-dimensional continuity equation for the species of interest:

$$\frac{\partial n_i}{\partial t} + \frac{\partial \Phi_i}{\partial z} = P_i - L_i$$

where n_i, Φ_i, P_i, and L_i are the concentration, vertical diffusive flux, and chemical production and loss terms respectively for species i (Allen *et al.* 1981). In most cases, steady-state conditions are assumed such that $\partial n_i/\partial t = 0$. The vertical flux is given by

$$\Phi_i = -D_i \left(\frac{dn_i}{dz} + \frac{n_i}{H_i} + \frac{n_i(1+\alpha)}{T}\frac{dT}{dz} \right) - K \left(\frac{dn_i}{dz} + \frac{n_i}{H} + \frac{n_i}{T}\frac{dT}{dz} \right)$$

where D_i is the molecular diffusion coefficient of species i through the background atmosphere, H_i is the scale height of species i, T is the temperature, α is the thermal diffusion factor (which we take to be zero), K is the eddy diffusion coefficient, and H is the scale height of the background atmosphere.

Our model atmosphere is composed of 121 levels of 2 km vertical extent, with the lower boundary at 0 km and the upper boundary at 240 km. Figure 1a shows our adopted temperature and total number density profiles. We have utilized the

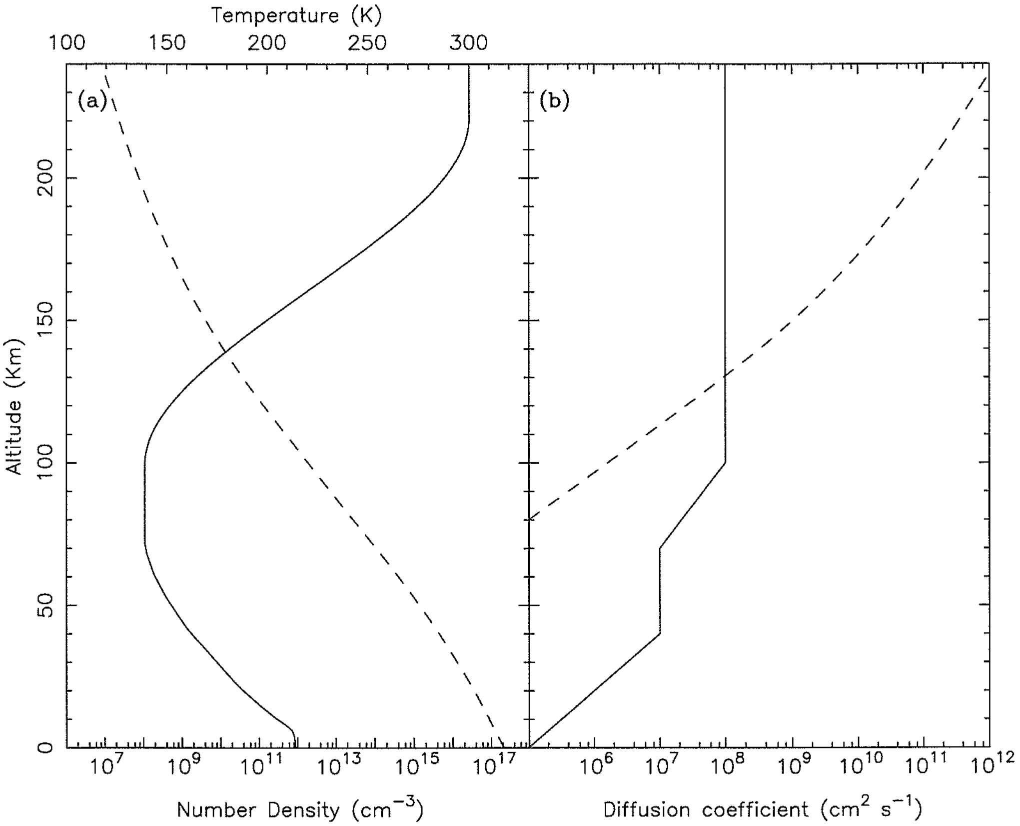

Figure 1. Adopted physical parameters for the model Mars atmosphere. (a) Temperature (solid line) and total number density (dashed line) profiles. (b) Eddy diffusion profile (solid line) and the molecular diffusion coefficient of atomic oxygen in the background atmosphere (dashed line)

COSPAR temperature profile (Seiff 1982) below 100 km and set the exospheric temperature to be 300 K, following Stewart and Hanson (1982). The temperature profile of the upper atmosphere was then found by fitting a spline curve to the COSPAR data and the exospheric temperature. The density structure of the atmosphere was computed assuming the condition of hydrostatic equilibrium. The pressure at the surface was taken to be 6.36 mbar, in agreement with Seiff (1982). The total number density was recomputed to be self consistent with the abundances computed for individual species, although little deviation from the initially assumed density profile was found.

Table II
List of reactions in the model Mars atmosphere

Reaction					Rate Coefficient	Reference
R1	$O_2 + h\nu$	$\longrightarrow$	$2\,O$		$1.4 \times 10^{-10}, 1.8 \times 10^{-7}$	1
R2		$\longrightarrow$	$O + O(^1D)$		$0, 1.0 \times 10^{-6}$	1
R3	$O_3 + h\nu$	$\longrightarrow$	$O_2 + O$		$2.5 \times 10^{-4}, 3.6 \times 10^{-4}$	2
R4		$\longrightarrow$	$O_2 + O(^1D)$		$1.5 \times 10^{-3}, 2.2 \times 10^{-3}$	2
R5		$\longrightarrow$	$3\,O$		$7.8 \times 10^{-10}, 2.0 \times 10^{-6}$	2
R6	$H_2 + h\nu$	$\longrightarrow$	$2\,H$		$0, 1.7 \times 10^{-6}$	3
R7	$OH + h\nu$	$\longrightarrow$	$O + H$		$4.8 \times 10^{-13}, 5.0 \times 10^{-6}$	4
R8	$HO_2 + h\nu$	$\longrightarrow$	$OH + O$		$1.1 \times 10^{-4}, 1.7 \times 10^{-4}$	5
R9	$H_2O + h\nu$	$\longrightarrow$	$H + OH$		$2.1 \times 10^{-11}, 3.5 \times 10^{-6}$	6
R10		$\longrightarrow$	$H_2 + O(^1D)$		$0, 2.4 \times 10^{-7}$	6
R11		$\longrightarrow$	$2\,H + O$		$0, 2.8 \times 10^{-7}$	6
R12	$H_2O_2 + h\nu$	$\longrightarrow$	$2\,OH$		$2.0 \times 10^{-5}, 3.2 \times 10^{-5}$	7
R13	$CO_2 + h\nu$	$\longrightarrow$	$CO + O$		$7.8 \times 10^{-13}, 6.7 \times 10^{-7}$	8
R14		$\longrightarrow$	$CO + O(^1D)$		$0, 2.4 \times 10^{-7}$	8
R15	$2\,O + M$	$\longrightarrow$	$O_2 + M$		$1.1 \times 10^{-27}\ T^{-2.0}$	5
R16	$O + O_2 + N_2$	$\longrightarrow$	$O_3 + N_2$		$5.0 \times 10^{-35}\ e^{724/T}$	9
R17	$O + O_2 + CO_2$	$\longrightarrow$	$O_3 + CO_2$		$1.3 \times 10^{-34}\ e^{724/T}$	See text
R18	$O + O_3$	$\longrightarrow$	$2\,O_2$		$8.0 \times 10^{-12}\ e^{-2060/T}$	5
R19	$O + CO + M$	$\longrightarrow$	$CO_2 + M$		$1.6 \times 10^{-32}\ e^{-2184/T}$	10
R20	$O(^1D) + O_2$	$\longrightarrow$	$O + O_2$		$3.2 \times 10^{-11}\ e^{70/T}$	5
R21	$O(^1D) + O_3$	$\longrightarrow$	$2\,O_2$		1.2×10^{-10}	5
R22		$\longrightarrow$	$O_2 + 2\,O$		1.2×10^{-10}	5
R23	$O(^1D) + H_2$	$\longrightarrow$	$H + OH$		1.0×10^{-10}	5
R24	$O(^1D) + CO_2$	$\longrightarrow$	$O + CO_2$		$7.4 \times 10^{-11}\ e^{120/T}$	5
R25	$O(^1D) + H_2O$	$\longrightarrow$	$2\,OH$		2.2×10^{-10}	5
R26	$2\,H + M$	$\longrightarrow$	$H_2 + M$		$3.8 \times 10^{-29}\ T^{-1.3}$	11
R27	$H + O_2 + M$	$\longrightarrow$	$HO_2 + M$	$k_0 =$	$1.3 \times 10^{-27}\ T^{-1.6}$	5
				$k_\infty =$	7.5×10^{-11}	
R28	$H + O_3$	$\longrightarrow$	$OH + O_2$		$1.4 \times 10^{-10}\ e^{-470/T}$	5
R29	$H + HO_2$	$\longrightarrow$	$2\,OH$		7.3×10^{-11}	12
R30		$\longrightarrow$	$H_2 + O_2$		6.5×10^{-12}	12
R31		$\longrightarrow$	$H_2O + O$		1.6×10^{-12}	12
R32	$O + H_2$	$\longrightarrow$	$OH + H$		$1.6 \times 10^{-11}\ e^{-4570/T}$	5
R33	$O + OH$	$\longrightarrow$	$O_2 + H$		$2.2 \times 10^{-11}\ e^{120/T}$	5
R34	$O + HO_2$	$\longrightarrow$	$OH + O_2$		$3.0 \times 10^{-11}\ e^{200/T}$	5
R35	$O + H_2O_2$	$\longrightarrow$	$OH + HO_2$		$1.4 \times 10^{-12}\ e^{-2000/T}$	5
R36	$2\,OH$	$\longrightarrow$	$H_2O + O$		$4.2 \times 10^{-12}\ e^{-240/T}$	5
R37	$2\,OH + M$	$\longrightarrow$	$H_2O_2 + M$	$k_0 =$	$1.7 \times 10^{-28}\ T^{-0.8}$	5
				$k_\infty =$	1.5×10^{-11}	
R38	$OH + O_3$	$\longrightarrow$	$HO_2 + O_2$		$1.6 \times 10^{-12}\ e^{-940/T}$	5
R39	$OH + H_2$	$\longrightarrow$	$H_2O + H$		$5.5 \times 10^{-12}\ e^{-2000/T}$	5
R40	$OH + HO_2$	$\longrightarrow$	$H_2O + O_2$		$4.8 \times 10^{-11}\ e^{250/T}$	5
R41	$OH + H_2O_2$	$\longrightarrow$	$H_2O + HO_2$		$2.9 \times 10^{-12}\ e^{-160/T}$	5
R42	$OH + CO$	$\longrightarrow$	$CO_2 + H$		$1.5 \times 10^{-13}\ (1 + 0.6\,P_{atm})$	5
R43	$HO_2 + O_3$	$\longrightarrow$	$OH + 2\,O_2$		$1.1 \times 10^{-14}\ e^{-500/T}$	5
R44	$2\,HO_2$	$\longrightarrow$	$H_2O_2 + O_2$		$2.3 \times 10^{-13}\ e^{600/T}$	5

TABLE II — *Continued*

	Reaction				Rate Coefficient	Reference
R45	$2\,HO_2 + M$	$\longrightarrow$	$H_2O_2 + O_2 + M$		$4.3 \times 10^{-33}\, e^{1000/T}$	5
R46	N_2	$\longrightarrow$	$2\,N$			See text
R47		$\longrightarrow$	$2\,N(^2D)$			See text
R48	$NO + h\nu$	$\longrightarrow$	$N + O$		$3.1 \times 10^{-12}, 1.2 \times 10^{-6}$	13
R49	$NO_2 + h\nu$	$\longrightarrow$	$NO + O$		$1.6 \times 10^{-3}, 2.4 \times 10^{-3}$	5
R50	$NO_3 + h\nu$	$\longrightarrow$	$NO_2 + O$		$5.3 \times 10^{-2}, 7.2 \times 10^{-2}$	14
R51		$\longrightarrow$	$NO + O_2$		$4.4 \times 10^{-3}, 6.0 \times 10^{-3}$	14
R52	$N_2O + h\nu$	$\longrightarrow$	$N_2 + O(^1D)$		$4.5 \times 10^{-8}, 1.8 \times 10^{-6}$	5
R53	$N_2O_5 + h\nu$	$\longrightarrow$	$NO_2 + NO_3$		$1.2 \times 10^{-4}, 2.0 \times 10^{-4}$	5
R54	$HNO_2 + h\nu$	$\longrightarrow$	$OH + NO$		$3.1 \times 10^{-4}, 4.2 \times 10^{-4}$	5
R55	$HNO_3 + h\nu$	$\longrightarrow$	$NO_2 + OH$		$1.7 \times 10^{-5}, 4.2 \times 10^{-5}$	5
R56	$HO_2NO_2 + h\nu$	$\longrightarrow$	$HO_2 + NO_2$		$8.7 \times 10^{-5}, 1.4 \times 10^{-4}$	5
R57	$N + O_2$	$\longrightarrow$	$NO + O$		$1.5 \times 10^{-11}\, e^{-3600/T}$	5
R58	$N + O_3$	$\longrightarrow$	$NO + O_2$		1.0×10^{-16}	15
R59	$N + OH$	$\longrightarrow$	$NO + H$		$3.8 \times 10^{-11}\, e^{85/T}$	15
R60	$N + HO_2$	$\longrightarrow$	$NO + OH$		2.2×10^{-11}	16
R61	$N + NO$	$\longrightarrow$	$N_2 + O$		3.4×10^{-11}	5
R62	$N + NO_2$	$\longrightarrow$	$N_2O + O$		3.0×10^{-12}	5
R63	$N(^2D) + O$	$\longrightarrow$	$N + O$		6.9×10^{-13}	17
R64	$N(^2D) + CO_2$	$\longrightarrow$	$NO + CO$		3.5×10^{-13}	18
R65	$N(^2D) + N_2$	$\longrightarrow$	$N + N_2$		1.7×10^{-14}	19
R66	$N(^2D) + NO$	$\longrightarrow$	$N_2 + O$		6.9×10^{-11}	17
R67	$O + NO + M$	$\longrightarrow$	$NO_2 + M$	$k_0 =$	$1.2 \times 10^{-27}\, T^{-1.5}$	5
				$k_\infty =$	3.0×10^{-11}	
R68	$O + NO_2$	$\longrightarrow$	$NO + O_2$		$6.5 \times 10^{-12}\, e^{120/T}$	5
R69	$O + NO_2 + M$	$\longrightarrow$	$NO_3 + M$	$k_0 =$	$2.0 \times 10^{-26}\, T^{-2.0}$	5
				$k_\infty =$	2.2×10^{-11}	
R70	$O + NO_3$	$\longrightarrow$	$O_2 + NO_2$		1.0×10^{-11}	5
R71	$O + HO_2NO_2$	$\longrightarrow$	$OH + NO_2 + O_2$		$7.8 \times 10^{-11}\, e^{-3400/T}$	5
R72	$O(^1D) + N_2$	$\longrightarrow$	$O + N_2$		$1.8 \times 10^{-11}\, e^{110/T}$	5
R73	$O(^1D) + N_2 + M$	$\longrightarrow$	$N_2O + M$		$2.8 \times 10^{-35}\, T^{-0.6}$	5
R74	$O(^1D) + N_2O$	$\longrightarrow$	$2\,NO$		6.7×10^{-11}	5
R75		$\longrightarrow$	$N_2 + O_2$		4.9×10^{-11}	5
R76	$NO + O_3$	$\longrightarrow$	$NO_2 + O_2$		$2.0 \times 10^{-12}\, e^{-1400/T}$	5
R77	$NO + HO_2$	$\longrightarrow$	$NO_2 + OH$		$3.7 \times 10^{-12}\, e^{240/T}$	5
R78	$NO + NO_3$	$\longrightarrow$	$2\,NO_2$		$1.7 \times 10^{-11}\, e^{150/T}$	5
R79	$H + NO_2$	$\longrightarrow$	$OH + NO$		$2.2 \times 10^{-10}\, e^{-182/T}$	20
R80	$H + NO_3$	$\longrightarrow$	$OH + NO_2$		1.1×10^{-10}	21
R81	$OH + NO + M$	$\longrightarrow$	$HNO_2 + M$	$k_0 =$	$4.8 \times 10^{-24}\, T^{-2.6}$	5
				$k_\infty =$	$2.6 \times 10^{-10}\, T^{-0.5}$	
R82	$OH + NO_2 + M$	$\longrightarrow$	$HNO_3 + M$	$k_0 =$	$5.5 \times 10^{-22}\, T^{-3.2}$	5
				$k_\infty =$	$4.0 \times 10^{-8}\, T^{-1.3}$	
R83	$OH + NO_3$	$\longrightarrow$	$HO_2 + NO_2$		2.3×10^{-11}	15
R84	$OH + HNO_2$	$\longrightarrow$	$H_2O + NO_2$		$1.8 \times 10^{-11}\, e^{-390/T}$	15
R85	$OH + HNO_3$	$\longrightarrow$	$NO_3 + H_2O$		$7.2 \times 10^{-15}\, e^{785/T}$	5
R86	$OH + HO_2NO_2$	$\longrightarrow$	$H_2O + NO_2 + O_2$		$1.3 \times 10^{-12}\, e^{380/T}$	5

TABLE II — *Continued*

	Reaction				Rate Coefficient	Reference
R87	$HO_2 + NO_2 + M$	$\longrightarrow$	$HO_2NO_2 + M$	$k_0 =$	$3.8 \times 10^{-23}\ T^{-3.2}$	5
				$k_\infty =$	$1.4 \times 10^{-8}\ T^{-1.4}$	
R88	$HO_2 + NO_3$	$\longrightarrow$	$O_2 + HNO_3$		9.2×10^{-13}	22
R89	$NO_2 + O_3$	$\longrightarrow$	$NO_3 + O_2$		$1.2 \times 10^{-13}\ e^{-2450/T}$	5
R90	$NO_2 + NO_3 + M$	$\longrightarrow$	$N_2O_5 + M$	$k_0 =$	$2.5 \times 10^{-19}\ T^{-4.3}$	5
				$k_\infty =$	$2.6 \times 10^{-11}\ T^{-0.5}$	
R91	$NO_2 + NO_3$	$\longrightarrow$	$NO + NO_2 + O_2$		$8.2 \times 10^{-14}\ e^{-1480/T}$	5
R92	$O + h\nu$	$\longrightarrow$	$O^+ + e^-$		$0, 1.1 \times 10^{-7}$	23
R93	$O_2 + h\nu$	$\longrightarrow$	$O_2^+ + e^-$		$0, 2.5 \times 10^{-7}$	1
R94	$CO_2 + h\nu$	$\longrightarrow$	$CO_2^+ + e^-$		$0, 3.3 \times 10^{-7}$	8
R95		$\longrightarrow$	$CO + O^+ + e^-$		$0, 2.8 \times 10^{-8}$	8
R96	$O_2^+ + e^-$	$\longrightarrow$	$2\,O$		$6.6 \times 10^{-5}\ T_e^{-1.0}$	24
R97	$CO_2^+ + e^-$	$\longrightarrow$	$CO + O$		3.8×10^{-7}	24
R98	$O^+ + CO_2$	$\longrightarrow$	$O_2^+ + CO$		9.6×10^{-10}	25
R99	$O + CO_2^+$	$\longrightarrow$	$O_2^+ + CO$		1.6×10^{-10}	25
R100		$\longrightarrow$	$O^+ + CO_2$		9.6×10^{-11}	28
R101	$CO_2H^+ + e^-$	$\longrightarrow$	$CO_2 + H$		3.0×10^{-7}	26
R102	$CO_2^+ + H_2$	$\longrightarrow$	$CO_2H^+ + H$		4.7×10^{-10}	25
R103	$HO_2 + \text{grain}$	$\longrightarrow$	$(HO_2)_{\text{grain}}$			See text
R104	$(HO_2)_{\text{grain}} + OH$	$\longrightarrow$	$H_2O + O_2$			See text

Units are s^{-1} for photolysis reactions, $cm^3\ s^{-1}$ for two-body reactions, and $cm^6\ s^{-1}$ for three-body reactions. Photolysis rate coefficients are given at the ground and at the top of the model atmosphere (240 km). k_0 and k_∞ are the low and high pressure rate coefficients, respectively, for three-body reactions.

References: (1) See references in Yung *et al.* (1988) and Anbar *et al.* (1993a), also Nicolet (1984), Lee *et al.* (1977), Samson *et al.* (1982); (2) See references in Anbar *et al.* (1993a), also Taherian and Slanger (1985), Turnipseed *et al.* (1991), Wine and Ravishankara (1982), Brock and Watson (1980), Sparks *et al.* (1980), Fairchild *et al.* (1978); (3) Mentall and Gentieu (1970), R. Gladstone, private communication; (4) Nee and Lee (1984), van Dishoeck and Dalgarno (1984), van Dishoeck *et al.* (1984); (5) Demore *et al.* (1990); (6) See references in Anbar *et al.* (1993a), also Philips *et al.* (1977); (7) Schürgers and Welge (1968), Demore *et al.* (1990); (8) See references in Yung *et al.* (1988) and Anbar *et al.* (1993a), also Kronebusch and Berkowitz (1976), Masuoka and Samson (1980); (9) Lin and Leu (1982); (10) Baulch *et al.* (1976); (11) Tsang and Hampson (1986); (12) DeMore *et al.* (1990), Keyser (1986); (13) Allen and Frederick (1982); (14) DeMore *et al.* (1990), Magnotta and Johnston (1980); (15) Atkinson *et al.* (1989); (16) Brune *et al.* (1983); (17) Fell *et al.* (1990); (18) Piper *et al.* (1987); (19) Schofield (1979); (20) Ko and Fontijn (1991); (21) Boodaghians *et al.* (1988); (22) Hall *et al.* (1988), Mellouki *et al.* (1988); (23) Samson and Pareek (1985); (24) McElroy *et al.* (1977); (25) Anicich and Huntress (1986), Anicich (1993); (26) Kong and McElroy (1977a).

We simultaneously solve the continuity equations for 27 species: O, $O(^1D)$, O_2, O_3, N, $N(^2D)$, N_2, N_2O, NO, NO_2, NO_3, N_2O_5, HNO_2, HNO_3, HO_2NO_2, H, H_2, H_2O, OH, HO_2, H_2O_2, CO, CO_2, O^+, O_2^+, CO_2^+, and CO_2H^+. The electron density is taken to be equal to the total ion concentration to ensure electrical neutrality. Table II is the list of reactions along with their recommended rate constants that we have employed in our model. Chemical kinetics data (rate coefficients and cross sections) are taken chiefly from the JPL90 compilation (DeMore *et al.* 1990). Most rate constants for three-body reactions are measured using air as the third body. However, CO_2 is known to be a more efficient third body than air (see discussion in Lindner 1985, 1988). Based upon the third body effect of CO_2 in the reaction $O + O_2 + M$, as shown in in Table III, we have increased the rate constants of reactions with CO_2 as a third body by a factor of 2.5. The sensitivity of the model to this assumption will be discussed in a later section. The rate constant for R17 was chosen by increasing the rate constant of R16 from Lin and Leu (1982) a factor of 2.5. Rate coefficients for three-body reactions were computed as a function of local atmospheric density from the limiting low and high pressure values (k_0 and k_∞, respectively) using the formulation in JPL90. Branching ratios for the reaction $H + HO_2$ were taken from Keyser (1986). The temperature dependence of the CO_2 absorption cross sections was parameterized by the method of Anbar *et al.* (1993a), assuming that the cross sections at temperatures below 202 K are equal to the cross section at 202 K and also that the cross sections longward of 1975 Å have the same temperature dependence as for the 1925-1975 Å interval. We will also consider cases where we extrapolate the temperature dependence to below 202 K. We account for electron impact ionization by the method suggested by Krasnopolsky (1986), where the photoionization cross section of CO_2 is increased for wavelengths below 400 Å to account for secondary ionization by photoelectrons.

The rate of vertical transport in the atmosphere is parameterized by the sum of eddy and molecular diffusion. Nier and McElroy (1977) derived eddy diffusion coefficients (K) on the order of $10^7 - 10^9$ cm^2 s^{-1} for the atmosphere above 100 km,

Table III
Third-body effect on the rate of ozone formation

M	k (10^{-34} cm^6 s^{-1})	Reference
N_2	5.6	Kaufman and Kelso (1967)
	5.7 ± 0.2	Lin and Leu (1982)
O_2	6.5	Kaufman and Kelso (1967)
	5.4 ± 0.3	Bevan and Johnson (1972)
	6.0 ± 0.3	Lin and Leu (1982)
Air	6.0 ± 0.5	DeMore *et al.* (1990)
CO_2	15	Kaufman and Kelso (1967)
	13.3 ± 1.2	Bevan and Johnson (1972)

based upon neutral mass spectrometer measurements by the Viking landers during their respective descents. Shimazaki (1989) found that a value of 5×10^7 cm^2 s^{-1} was satisfactory in the upper atmosphere to match the atomic oxygen measurements made by Mariners 6, 7, and 9 (Strickland *et al.* 1972, 1973). Rodrigo *et al.* (1990) chose values between $10^7 - 10^9$ cm^2 s^{-1} based on observed CO abundances. Krasnopolsky (1993b) and Atreya and Gu (1994) assume eddy diffusion coefficients above 100 km vary in inverse proportion to the square root of atmospheric density and also find values between 10^7 cm^2 s^{-1} at 100 km, increasing to 10^9 cm^2 s^{-1} at 200 km. Thus most estimates of the eddy diffusion coefficient in the upper atmosphere are in reasonable agreement.

However, the value of K in the lower atmosphere is highly uncertain. Kahn (1990) suggested that the value of the eddy diffusion coefficient may vary by up to three orders of magnitude, depending upon season and local conditions. As briefly discussed in the introduction, some photochemical models, such as those of McElroy and Donahue (1972), Liu and Donahue (1976), Kong and McElroy (1977a), and Yung *et al.* (1988) concentrated the bulk of their water near the surface, requiring eddy diffusion coefficients on the order of 10^8 cm^2 s^{-1}. Other models, for example those of Krasnopolsky and Parshev (1979), Shimazaki (1989), Krasnopolsky (1993b), and Atreya and Gu (1994), with more well-mixed water profiles, required values of K on the order of $10^5 - 10^7$ cm^2 s^{-1}, more in agreement with aerosol studies, such as Anderson and Leovy (1978), Toon *et al.* (1977), Chassefière *et al.* (1992), and Korablev (1993a).

In light of these uncertainties, we have employed the profile shown in Fig. 1b, where the eddy diffusion coefficient (solid line) at the ground is 10^5 cm^2 s^{-1}, increases exponentially to 10^7 cm^2 s^{-1} at 40 km, remains constant until 70 km, where it again increases to 10^8 cm^2 s^{-1} at 100 km. The profile below 40 km is consistent with the values suggested by aerosol studies for the lower atmosphere. The values between 40 and 70 km were chosen to better reproduce the mixing ratio of O_2, which will be discussed in the next section. The eddy diffusion coefficients above 100 km were chosen to match the abundance of atomic oxygen in the thermosphere. Both the bulk mixing ratio of O_2 and the high altitude abundance of O are anticorrelated with the vigor of vertical motion (McElroy and Hunten 1970, McElroy and McConnell 1971).

As the density decreases with altitude, turbulent motions become ineffective at keeping the atmosphere well mixed and individual constituents tend to assume their own scale heights. In the upper regions of the atmosphere, transport is dominated by molecular diffusion, where the value of the molecular diffusion coefficient D is dependent upon the species under consideration and the composition of the surrounding gas. The dashed line in Fig. 1b shows the molecular diffusion coefficient for atomic oxygen in the background atmosphere. The method used to compute molecular diffusion coefficients is described in appendix I. We have also included the effects of ambipolar diffusion for ions, using the formulations given in Atreya (1986). Electron temperatures were taken from Fox (1993a) and ion temperatures were taken from

Hanson *et al.* (1977).

Water and hydrogen peroxide are potentially condensible species in our model. The partial pressure of H_2O_2 never exceeds the saturation vapor pressure, given by the expression in Lindner (1985, 1988), in any of the models we consider, but water becomes supersaturated above ~ 30 to 40 km. We simulate the effects of condensation by imposing the constraint that the partial pressure of water never exceeds the saturation vapor pressure, given by

$$\log_{10} P_{sat} = \frac{-2445.5646}{T} + 8.2312 \log_{10} T - 0.01677006\, T$$
$$+ 1.20514 \times 10^{-5}\, T^2 - 6.757169$$

where P_{sat} is in mm Hg and T is in degrees Kelvin (Washburn 1924). Our water profiles (Fig. 2a) are similar in character to those employed by Shimazaki (1989), Krasnopolsky (1993b), and Atreya and Gu (1994), where water vapor is assumed to be well mixed up to the altitude where condensation first occurs. Above this point, the scale height is fixed to a value of 4.2 km such that the water vapor profile roughly follows the saturation curve. This agrees quite well with the mean scale height of 3.8 km for water in the 12 to 45 km altitude range found from *Phobos 2* observations (Krasnopolsky *et al.* 1991). The water vapor abundance above ~ 60 km is calculated consistently with the other species, as it is undersaturated above this level. Two water profiles were considered, one with an integrated column abundance of 3.0 pr. μm, in agreement with the recent observations of Clancy *et al.* (1992), and one with an integrated abundance of 8.8 pr. μm, in agreement with the measurements of Rizk *et al.* (1991) for $L_s = 208°$.

Figure 2b shows the production rates of nitrogen atoms that we have prescribed in our model as a function of altitude. Atomic nitrogen can be produced in the ground state, $N(^4S)$, or in the electronically excited $N(^2D)$ or $N(^2P)$ states chiefly by electron

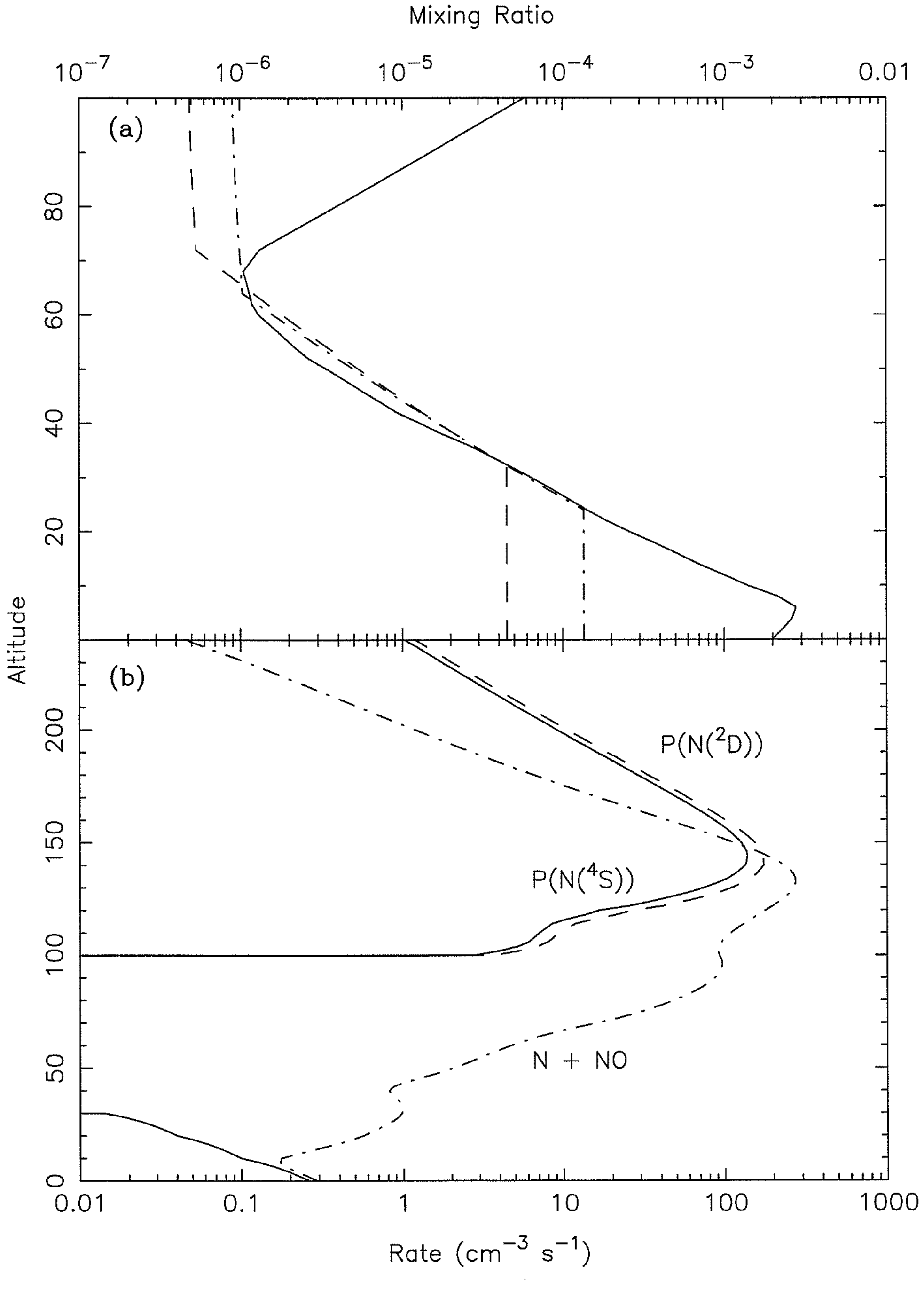

Figure 2. More adopted physical parameters for the model Mars atmosphere. (a) The dashed line is a low water profile, with an integrated column abundance of 3 pr. μm. The dot-dashed line is a high water profile with an integrated abundance of 8.8 pr. μm. The solid line represents the saturation curve for water with our adopted temperature profile. (b) production and loss rates for odd nitrogen. The rate for N + NO is an output from our standard model, discussed in section III.

impact and dissociative recombination:

$$N_2 + e^- \longrightarrow N + N + e^-$$

and

$$N_2^+ + e^- \longrightarrow N + N.$$

We have used production rates kindly provided by Jane Fox (private communication, 1992). Since N(^{2}P) chemistry is not included in our photochemical model, the N(^{2}D) production rate is taken to be the sum of the N(^{2}D) and N(^{2}P) production rates computed by Fox. We also include a source of nitrogen atoms near the surface due to cosmic rays, as described by Yung *et al.* (1977).

Solar flux values at 1 AU were taken from from Torr and Torr (1985), Mount and Rottman (1981,1982), and the WMO (1985), and were scaled to 1.52 AU. In order to represent average solar conditions, we took the mean of solar minimum and maximum fluxes shortward of 1800 Å. The transmission for a spherical atmosphere was diurnally averaged for 30° latitude at the equinox. The principal absorbers in the atmosphere were assumed to be O_2, O_3, NO_2, H_2O, and CO_2. Dust free conditions were assumed, and Rayleigh scattering is accounted for by the radiative transfer model described in Michelangeli *et al.* (1992). Reflection from the surface is also accounted for; we assume an albedo of 0.04 from 1000 to 4000 Å and 0.2 from 7000 Å to 8000 Å, with a linear increase in the intermediate region, as suggested by Lindner (1985). Calculations incorporating heterogeneous chemistry will be discussed in a later section.

The lower boundary conditions are mixing ratios of 2.7×10^{-2} for N_2, either 4.5×10^{-5} or 1.35×10^{-4} for H_2O, and fixed concentrations of 2.05×10^{17} cm^{-3} for CO_2 and zero for the ions. Upper boundary conditions are H and H_2 effusion velocities of 3.1×10^3 cm s^{-1} and 3.4×10^1 cm s^{-1} respectively. These velocities were calculated following the expression for Jeans escape in Hunten (1973). We also impose an escape flux of atomic oxygen at the upper boundary of 1.2×10^8 $\mathrm{cm^{-2}\ s^{-1}}$. This boundary condition is discussed more fully later. Zero fluxes were assumed for all other species as upper and lower boundary conditions.

3. The photochemistry of the lower atmosphere

3.1 Chemistry of CO_2 photolysis products

In order to quantitatively demonstrate the relative importance of key influences on the abundances of atmospheric constituents and to test our photochemical model, we have performed a series of model calculations as summarized in Table IV. In the first case, we have assumed a completely dry atmosphere, composed purely of CO_2 and its photolysis products, with no escape assumed for any species through the upper boundary. This is the classical model where CO_2 is reformed by the spin forbidden reaction

$$\text{(R19)} \qquad CO + O + M \longrightarrow CO_2 + M.$$

In this scenario, we find large ($\sim$ 100 times larger than observed) abundances for CO and O_2 in the ratio 2:1, as expected. Note that CO and O_2 are still minor constituents and that the atmosphere is photochemically stable. In the second case, we have introduced 8.8 pr. μm of water vapor into the model. Now the mixing ratios for CO and O_2 fall drastically to values more in agreement with the observed quantities (*cf* Table I), demonstrating the importance of HO_x catalyzed recombination for controlling the abundances of photochemically produced species. In this case, the CO/O_2 ratio is roughly one due to the large amount of H_2 in the model and concurrently liberated oxygen. One sees that the relation

$$[CO] + [H_2] = 2[O_2]$$

Table IV

Steady-state model results for simple test cases

	Input parameters			Model results				
Case	Column H_2O (pr. μm)	ϕ_O (10^8 cm^{-2} s^{-1})	NO_x	f_{CO}	f_{O_2}	f_{CO}/f_{O_2}	f_{H_2}	$\phi_H + 2\,\phi_{H_2}$ (10^8 cm^{-2} s^{-1})
1	0	0	no	7.27×10^{-2}	3.63×10^{-2}	2.0	0	0
2	8.8	0	no	2.90×10^{-4}	3.36×10^{-4}	0.8	3.86×10^{-4}	0
3	8.8	1.2	no	1.52×10^{-4}	1.84×10^{-3}	0.1	3.60×10^{-5}	2.4
4	8.8	1.2	yes	1.23×10^{-4}	1.27×10^{-3}	0.1	3.63×10^{-5}	2.4

Note: ϕ denotes escape flux and f denotes surface mixing ratio, boundary conditions are $[CO_2] = 2.05 \times 10^{17}$ cm^{-3} for all cases, $[H_2O] = 2.85 \times 10^{13}$ cm^{-3} for cases 2, 3, and 4, with the respective profiles initialized as described in the text. Altitude profiles of all other species were initialized to zero.

holds in this case. Next, we allow H and H_2 to escape thermally and O to escape with a flux of 1.2×10^8 cm^{-2} s^{-1}. The introduction of escape of light atoms from the atmosphere leads to a CO/O_2 ratio less than one and a ratio of escaping H atoms to O atoms of 2:1, in agreement with the argument of McElroy (1972). Finally, the inclusion of NO_x chemistry produces OH while breaking the O-O bond through the reaction

$$\text{(R77)} \qquad NO + HO_2 \longrightarrow NO_2 + OH,$$

leading to lowered abundances of CO and O_2. This is our standard, high water case.

Figure 3 shows the calculated mixing ratios of the major and minor species in our standard, high water model. Although the model contains over one hundred reactions, only a relatively small number of them are important in determining these profiles. We may identify the key reactions in the lower atmosphere, in particular those governing the CO/O_2 ratio and the concentration of ozone, by constructing simple, steady-state, analytical formulas similar to those developed for ozone on Mars (Barth 1985) and in the terrestrial upper atmosphere (Allen *et al.* 1984).

As discussed in the introduction, CO is catalytically oxidized to CO_2 in the presence of HO_x radicals. The various schemes that have been proposed differ mainly in the production pathways for the OH radical. Other catalytic cycles may also be devised, such as

$$\begin{array}{lrcl}
\text{(R27)} & H + O_2 + M & \longrightarrow & HO_2 + M \\
\text{(R77)} & NO + HO_2 & \longrightarrow & OH + NO_2 \\
\text{(R68)} & O + NO_2 & \longrightarrow & NO + O_2 \\
\text{(R42)} & CO + OH & \longrightarrow & CO_2 + H \\
\hline
\text{net} & CO + O & \longrightarrow & CO_2.
\end{array}$$

Figure 4a shows the rates of the important reactions in these cycles. Since most of the OH is produced by R34, we see that the three reactions

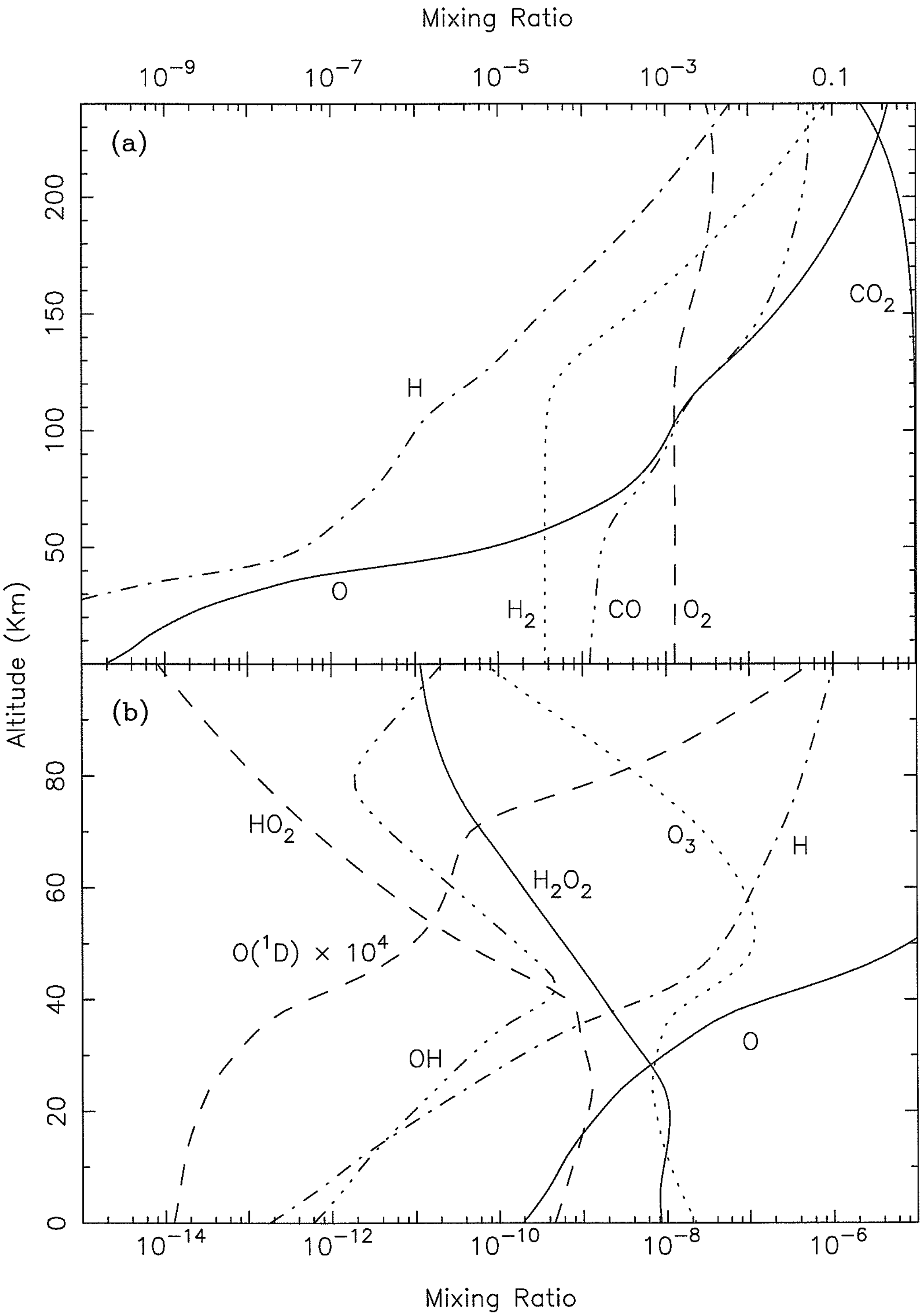

Figure 3. Altitude versus mixing ratio profiles for (a) major CHO and (b) HO_x and O_x species in our standard model. The integrated water abundance is 8.8 pr. μm.

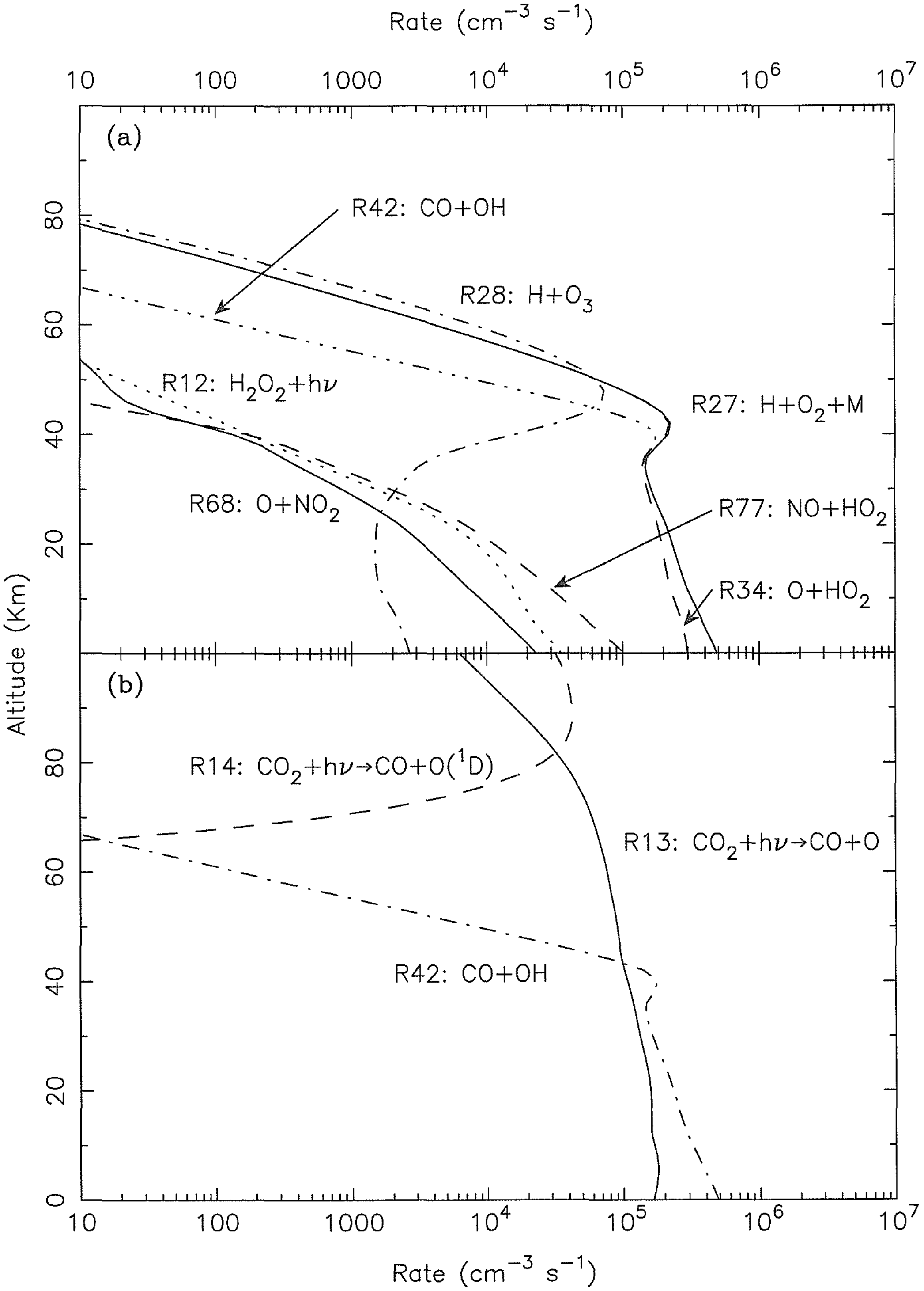

Figure 4. Rates of key reactions important for the stability of CO_2. (a) Rates of key reactions in the catalytic oxidation of CO. (b) Production and loss rates for CO_2.

(R27) $H + O_2 + M \longrightarrow HO_2 + M$
(R34) $O + HO_2 \longrightarrow OH + O_2$
(R42) $CO + OH \longrightarrow CO_2 + H$

which make up the primary scheme proposed by McElroy and Donahue (1972), form the dominant catalytic cycle in the oxidation of CO to CO_2. These rapid reactions also determine the partitioning of HO_x between H, OH, and HO_2 in the lower atmosphere. For example, the OH/HO_2 ratio may be determined by balancing the rates of R34 and R42:

$$\frac{[OH]}{[HO_2]} = \frac{k_{34}[O]}{k_{42}[CO]}. \tag{1}$$

The production and loss pathways for CO_2 are shown in Fig. 4b. Carbon dioxide is chiefly lost through photolysis:

(R13) $CO_2 + h\nu \longrightarrow CO + O$

and is reformed via R42. Equating the production and loss of CO, and noting that the rate of R42 is essentially equivalent to the rates of R27 and R34 (Fig. 4a), we may write the following equalities:

$$\begin{aligned} J_{13}[CO_2] &= k_{27}[H][O_2][M] && (2a)\\ &= k_{34}[O][HO_2] && (2b)\\ &= k_{42}[CO][OH]. && (2c) \end{aligned}$$

These equalities are strictly true only when integrated over the column, since CO is not in local photochemical steady state. As seen in Fig. 4b, a substantial quantity of CO is produced above 40 km, while oxidation to CO_2 occurs almost entirely below 40 km. However, we shall assume that these equalities are true in the lower atmosphere for the purpose of simplicity.

Figure 5a shows the reactions controlling the abundance of HO_x in the lower atmosphere. Odd hydrogen radicals are produced predominantly via water photolysis

(R9) $H_2O + h\nu \longrightarrow H + OH$

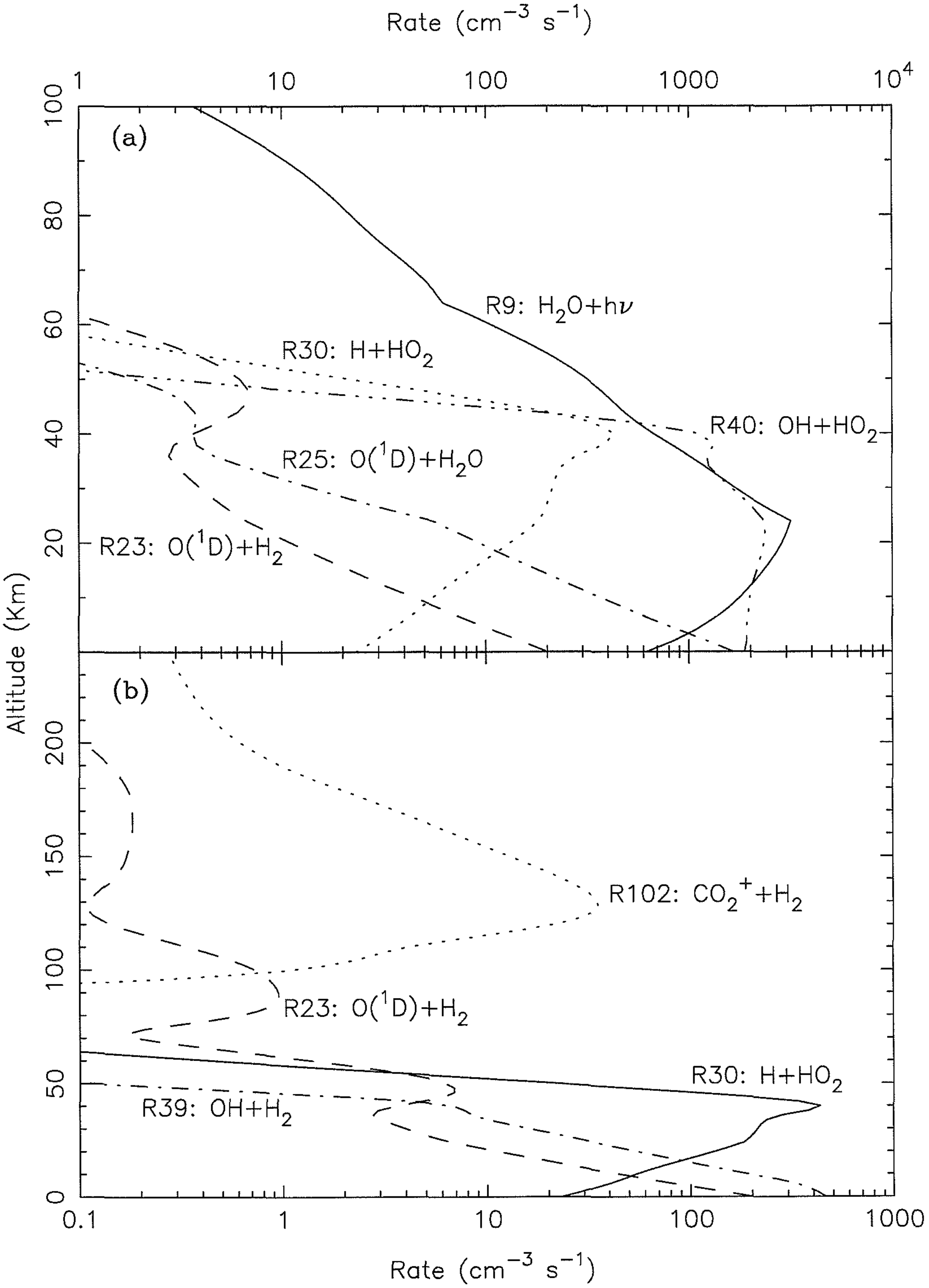

Figure 5. Rates of odd hydrogen reactions. (a) Production and loss rates for HO_x. (b) Production and loss rates for H_2.

and the reaction of water with $O(^1D)$:

(R25) $$O(^1D) + H_2O \longrightarrow 2\,OH.$$

Although R25 dominates near the surface, R9 is more important on a column-integrated basis by a factor of eight. HO_x radicals are lost chiefly through

(R40) $$OH + HO_2 \longrightarrow H_2O + O_2.$$

Balancing the rates of R9 and R40 we obtain the steady-state equation for the production and loss of odd hydrogen:

$$J_9[H_2O] = k_{40}[OH][HO_2]. \tag{3}$$

Molecular hydrogen is produced in the lower atmosphere by

(R30) $$H + HO_2 \longrightarrow H_2 + O_2$$

and is chemically destroyed via

(R23) $$O(^1D) + H_2 \longrightarrow H + OH$$

and

(R39) $$OH + H_2 \longrightarrow H + H_2O$$

at roughly equal rates, integrated over the atmospheric column (Fig. 5b). The destruction by CO_2^+ in the ionosphere will be discussed in a later section. As was the case with CO, the chemical lifetime of H_2 in the lower atmosphere, a few hundred years, is far longer than the transport timescale ($\tau \sim H^2/K$ = days to weeks). Thus in order to properly consider the hydrogen balance in the atmosphere, we must integrate the full continuity equation for H_2 :

$$\frac{\partial \phi_{H_2}}{\partial z} = P_{H_2} - L_{H_2}.$$

For convenience, we will say that the production rate of molecular hydrogen is some function of the oxygen escape flux, based on the postulate of McElroy (1972):

$$\begin{aligned} P_{H_2} &= k_{30}[H][HO_2] & (4a) \\ &= f(\phi_O). & (4b) \end{aligned}$$

This quantity should be relatively insensitive to variations in the water abundance (McElroy 1973). The mechanism by which the escape of atomic oxygen regulates P_{H_2} will be considered in more detail in the following section.

Combining Eqs. 2a, 2c, 3, and 4b, we obtain an equation for the $[CO]/[O_2]$ ratio in terms of physical processes in the martian atmosphere and basic chemical parameters:

$$\frac{[CO]}{[O_2]} = \frac{k_{27}\, k_{40}\, [CO_2]\, f(\phi_O)}{J_9\, k_{30}\, k_{42}\, [H_2O]}. \tag{5}$$

This is similar to expression (27) in McElroy (1973), where the production rates of water and molecular hydrogen were left as parameters. As Fig. 6 shows, Eq. 5 reproduces the model calculation reasonably well between 10 and 35 km, where Eq. 3 is valid and the bulk of CO production and loss occurs (Fig. 4b). We have used the rate of R30 for $f(\phi_O)$.

The abundance of O_2 is heavily dependent upon the value of the eddy diffusion coefficient (McElroy and Hunten 1970). If downward transport of O atoms formed through CO_2 photolysis high in the atmosphere is slow (Fig. 7a), large amounts of O_2 are able to form through

(R15) $$O + O + M \longrightarrow O_2 + M$$

and

(R33) $$O + OH \longrightarrow O_2 + H.$$

Conversely, if O is rapidly brought down (Fig. 7b), as several previous photochemical models have assumed (e.g., McElroy and Donahue 1972, Liu and Donahue 1976,

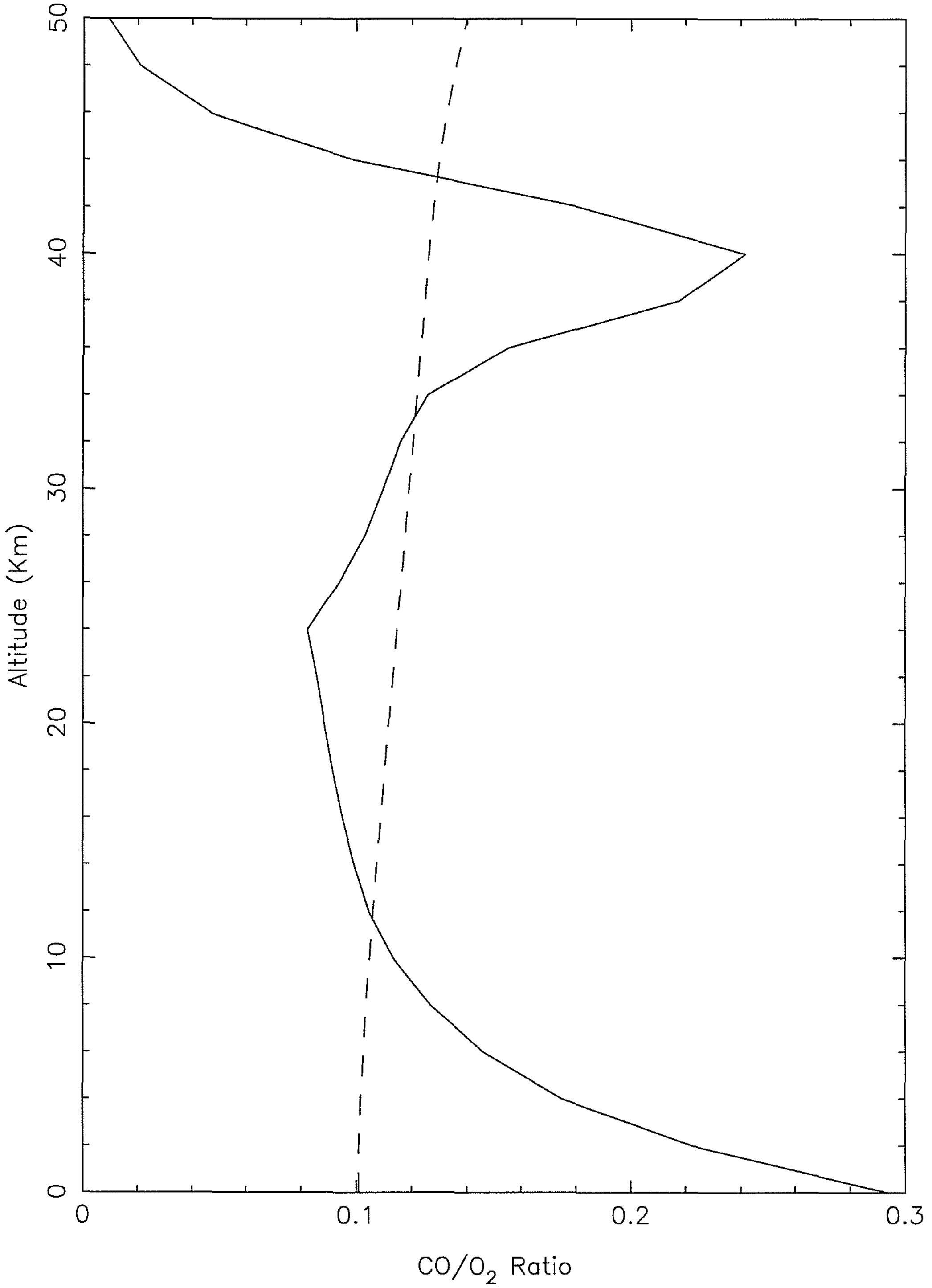

Figure 6. Comparison between the analytic expression Eq. 5 (solid line) and model output (dashed line) for the CO/O$_2$ ratio.

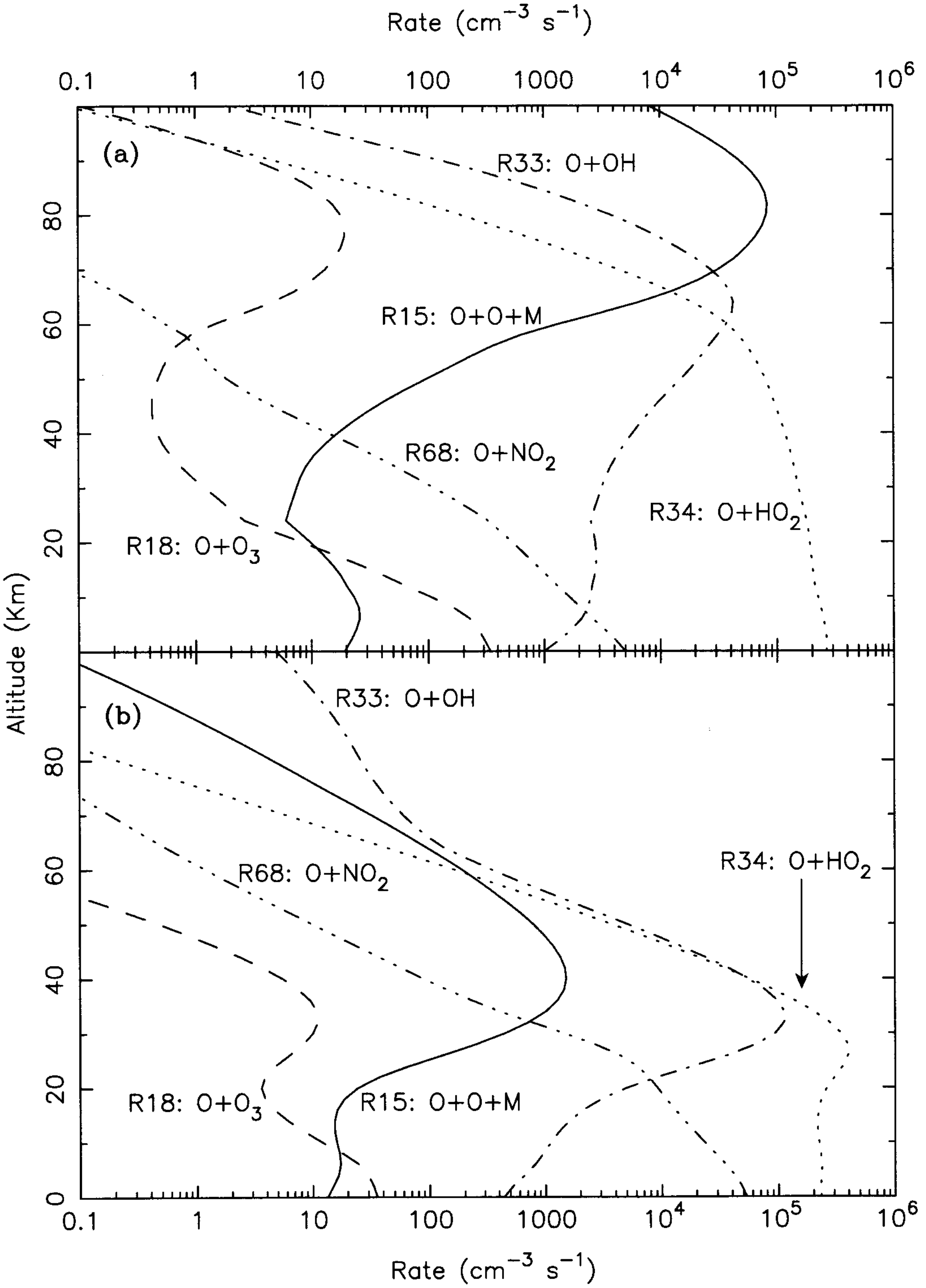

Figure 7. The loss rates for oxygen atoms for two different eddy diffusivity profiles, assumed constant with height. (a) $K = 10^5\,\mathrm{cm}^2\,\mathrm{s}^{-1}$, (b) $K = 10^8\,\mathrm{cm}^2\,\mathrm{s}^{-1}$.

Kong and McElroy 1977a, Yung *et al.* 1988), it will react with HO_2 (R34), ultimately reforming CO_2. This is not a production mechanism for O_2 as one oxygen molecule is required to produce the HO_2 radical. Another source for O_2 is the reaction with NO_2,

$$\text{(R68)} \qquad O + NO_2 \longrightarrow NO + O_2,$$

which is enhanced with faster downward transport, but cannot compensate for the smaller (column-integrated) rates of R15 and R33. In the standard model, the eddy diffusion coefficient between 40 and 70 km is set to the intermediate value of $10^7\ \mathrm{cm}^2\ \mathrm{s}^{-1}$ in order to match the observed O_2 abundance. The important contributors to the O_2 production rate are shown in Figure 8a.

The O_2 bond may be broken by the photolysis of O_2 (R1, R2), HO_2 (R8), or H_2O_2 (R12), or by the reaction of NO with HO_2 (R77) (Parkinson and Hunten 1972). As shown in Fig. 8b, R1 is the dominant sink of O_2 when integrated over the column, but the other reactions mentioned above provide a substantial contribution to the destruction of the O_2 molecule, particularly R77 near the surface.

The consideration of the oxygen budget on Mars is a complex problem that does not lend itself to an analytic solution, hence Eq. 5 cannot be further simplified to eliminate $[O_2]$ in terms of model inputs such as K. We will employ Eq. 5 to identify sources of disagreement between the model and observations of the CO/O_2 ratio in a later section.

The photochemistry of ozone in the martian atmosphere has been extensively modeled over the past two decades (in addition to previously mentioned papers, see Kong and McElroy 1977b, Shimazaki and Shimuzu 1979, Krasnopolsky and Parshev 1979, Shimazaki 1981, and Lindner 1988) and the inverse relationship between ozone amounts and atmospheric water vapor has been well known both from observations and modeling for the past two decades. A simple analytical expression for the

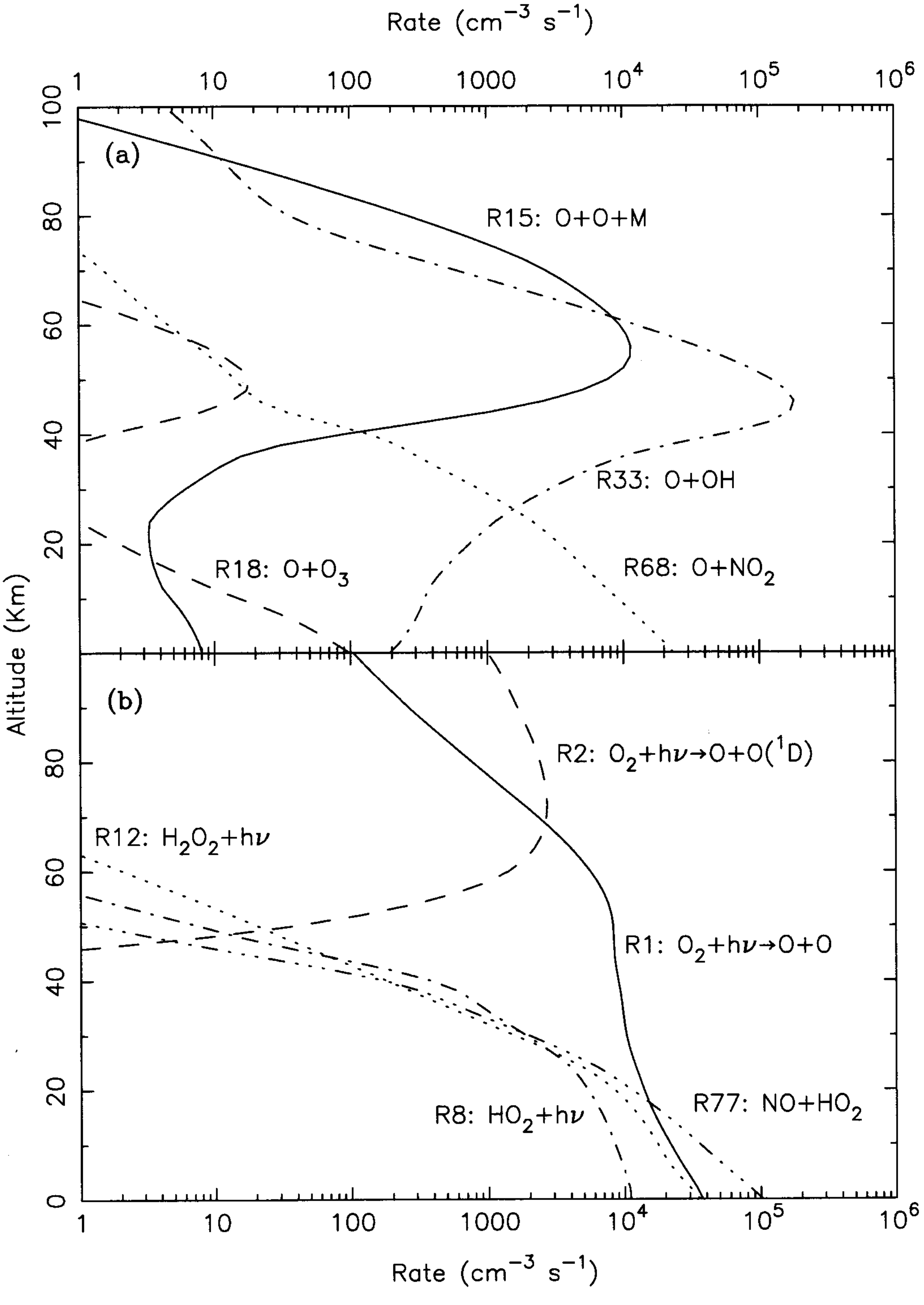

Figure 8. Reaction rates for the (a) production and (b) loss of the O-O bond in the standard model.

diurnally averaged ozone density may be derived if we assume that ozone is in photochemical equilibrium during daylight hours. This is a good approximation as the photochemical lifetime of ozone is roughly ten minutes while the transport timescale near the surface is of order weeks to months. The steady-state expression for the production and loss of ozone is

$$(J_3 + J_4)[\mathrm{O_3}] = k_{17}[\mathrm{O}][\mathrm{O_2}][\mathrm{CO_2}]. \tag{6}$$

Since ozone is mostly produced and destroyed near the surface, Eq. 3 should be modified to include the production of odd hydrogen due to R25 ($O(^1D) + H_2O$) :

$$(J_9 + k_{25}[\mathrm{O}(^1\mathrm{D})])[\mathrm{H_2O}] = k_{40}[\mathrm{OH}][\mathrm{HO_2}]. \tag{7}$$

Combining this equation with Eqs. 2b, 2c, and 6, we obtain

$$[\mathrm{O_3}] = \frac{J_9\, k_{24}\, [\mathrm{CO_2}]}{2\, J_4\, k_{25}} \left\{ \left(1 + \frac{4\, J_4\, k_{17}\, k_{25}\, k_{40}\, (J_{13}\, [\mathrm{CO_2}])^2}{(J_3 + J_4)\, J_9^2\, k_{24}\, k_{34}\, k_{42}\, [\mathrm{H_2O}]} \frac{[\mathrm{O_2}]}{[\mathrm{CO}]} \right)^{1/2} - 1 \right\}. \tag{8}$$

This is somewhat different from the expression presented by Barth (1985), as we have included photolysis along with reaction with $O(^1D)$ as pathways for water decomposition. The ozone abundance is indeed anticorrelated with the water abundance over *short* timescales; i.e., timescales short enough that the CO/O_2 ratio remains constant. Curiously, the expression for O_3 resulting from the substitution of Eq. 5 into Eq. 8 suggests that the ozone abundance over long timescales is to first order independent of the water concentration:

$$[\mathrm{O_3}] = \frac{J_9\, k_{24}\, [\mathrm{CO_2}]}{2\, J_4\, k_{25}} \left\{ \left(1 + \frac{4\, J_4\, k_{17}\, k_{25}\, k_{30}\, J_{13}^2\, [\mathrm{CO_2}]}{(J_3 + J_4)\, J_9\, k_{24}\, k_{27}\, k_{34}\, f(\phi_{\mathrm{O}})} \right)^{1/2} - 1 \right\}. \tag{9}$$

The seasonally varying ozone abundance may thus be taken to reflect fluctuations driven by HO_x chemistry about a mean ozone value that is explicitly tied to the escape flux of O and the production rate of H_2 and implicitly tied to the O_2 abundance (see next section). Equation 9 will be useful for understanding the sensitivity of computed O_3 values to changes in model parameters, which will be considered later in this paper.

3.2 The regulation of hydrogen escape

McElroy (1972) put forth the interesting suggestion that the nonthermal escape of energetic oxygen atoms produced via

$$\text{(R96)} \qquad O_2^+ + e^- \longrightarrow 2\,O$$

regulates the escape of hydrogen from the atmosphere such that two hydrogen atoms escape for each oxygen atom. The net result is that a water molecule escapes, leaving the oxidation state of the atmosphere unchanged.

McElroy argued that an imbalance in the escape rates would modify the amounts of CO and O_2, which in turn would alter the rate of production of H_2 in the following way: if O were escaping at a rate larger than what was necessary to balance the hydrogen escape, CO would rapidly increase as it was left behind while O_2 would rapidly decrease. Rewriting Eq. 5 to solve for the production rate of hydrogen, it is clear that an increase in CO and a decrease in O_2 ratio lead to an increase in P_{H_2}. The reason for this is that P_{H_2} is proportional to the product of the concentrations of H and HO_2. The H concentration in the lower atmosphere is determined by the reaction

$$\text{(R27)} \qquad H + O_2 + M \longrightarrow HO_2 + M.$$

Hence the concentration of atomic hydrogen is inversely proportional to the molecular oxygen abundance. Since HO_2 is far more abundant than H in this region, a rise in the H concentration translates to a rise in P_{H_2}. This increased rate of H_2 production causes the hydrogen escape rate to rise until the postulated imbalance is removed. (A similar argument can be made for the case where the hydrogen escape flux is more than twice the oxygen escape flux.) However, this premise was not confirmed by a detailed numerical model until the work of Liu and Donahue (1976), who demonstrated that the escape of oxygen does indeed regulate the hydrogen escape flux. Due to computational limitations, Liu and Donahue were not able to simply alter the oxygen escape flux and examine the response of the hydrogen escape flux as it relaxed to a new value. Instead a steady-state model was employed where the oxygen mixing ratio was varied in stages from 1.3×10^{-3} to 2.6×10^{-3}, presumably due to variations in the oxygen escape flux, and the impact on the hydrogen escape flux was noted.

We have performed a time dependent calculation in order to confirm the arguments of McElroy (1972) and Liu and Donahue (1976) and to numerically demonstrate the timescale over which variations in the O escape flux can influence the composition of the lower atmosphere. The molecular oxygen abundance was computed self consistently with the other species by solution of the continuity equation; no relationship was assumed to exist between the escape flux of atomic oxygen and the bulk mixing ratio of molecular oxygen in the lower atmosphere. The O escape flux is set to half of the value in our standard model, where the O escape flux of 1.2×10^8 cm^{-2} s^{-1} is balanced by an atomic hydrogen escape flux of 1.8×10^8 cm^{-2} s^{-1} and a molecular hydrogen flux of 2.8×10^7 cm^{-2} s^{-1}. Figure 9 plots the surface CO and O_2 mixing ratios, the column production rate of H_2, and the hydrogen escape fluxes respectively as a function of time after the reduction of the O escape flux. Initially, hydrogen continues to escape at a rate of 2.4×10^8 atoms cm^{-2} s^{-1}. This causes oxygen atoms to accumulate at a rate of 6×10^7 cm^{-2} s^{-1}, the deficit between the actual oxygen escape flux and that required to balance the hydrogen escape. Since the initial O_2 column abundance is 2.7×10^{20} cm^{-2}, the O_2 amount increases with a time constant of $\sim 3 \times 10^5$ years. As predicted by McElroy (1972), this is accompanied by a drop in the CO mixing ratio, as seen in Fig. 9a. The increasing O_2 abundance causes the H_2 production rate to decrease through the mechanism described earlier, consequently leading to a lower surface mixing ratio for H_2. As the H_2 abundance decreases, the hydrogen escape flux likewise decreases, hence lowering the accumulation

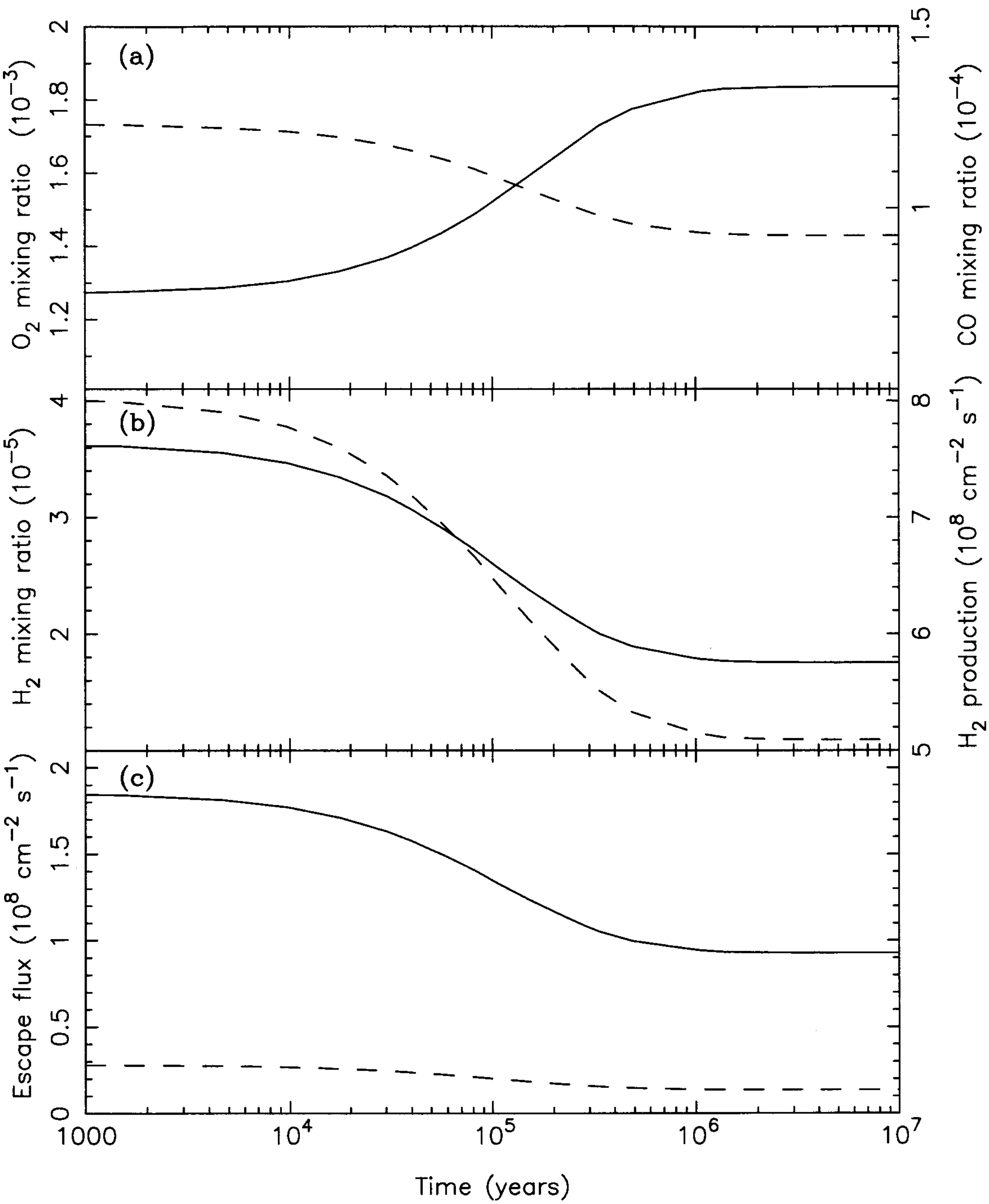

Figure 9. Response of the atmosphere to an abrupt decrease in the atomic oxygen escape flux by a factor of two. (a) The O_2 (solid line) and CO (dashed line) mixing ratios, (b) the H_2 mixing ratio (solid line) and H_2 production rate (dashed line), and (c) the atomic (solid line) and molecular (dashed line) hydrogen escape fluxes.

rate of oxygen. The O_2 mixing ratio continues to increase and the hydrogen escape flux continues to decrease until the accumulation rate becomes zero; i.e., when the hydrogen escape flux drops to become exactly twice the oxygen escape flux. A new equilibrium with a higher f_{O_2} is reached after 10^6 years, with the lower oxygen escape flux now balanced by $\phi_H = 9.3 \times 10^7$ cm^{-2} s^{-1} and $\phi_{H_2} = 1.4 \times 10^7$ cm^{-2} s^{-1}. Thus the chain of events described by McElroy (1972) and Liu and Donahue (1976) following a perturbation in the rate of O escape does indeed cause the atmosphere to respond over a timescale of $\sim 3 \times 10^5$ years. Mechanisms which remove oxygen from the atmosphere for periods longer than this timescale can influence the escape flux of hydrogen and the composition of the atmosphere as a whole. Some possible loss processes for oxygen and their impact on the balance between the escape fluxes will be discussed in a later section.

4. Comparison of standard model and observations

4.1 The standard model

Case a) of Table V summarizes the output from our standard model, where the calculations were made with the recommended rate constants of DeMore *et al.* (1990). The atomic hydrogen escape flux, the O_2 mixing ratio and the ozone amount are consistent with the observed values, although in the high water case the ozone abundance is close to the lower limit of Espenak *et al.* (1991). However, the CO mixing ratio computed in our standard model is a factor of four to five below observations. Each of these model results will be discussed in more detail in the following sections.

The homopause is defined as the altitude where the molecular diffusion coefficient D is comparable to the eddy diffusion coefficient K. As seen from Fig. 1b, the homopause is located at $\sim$ 135 km. Above this level molecular diffusion determines

Table V

Calculated abundances of CO, O_2, and O_3

	High water (8.8 pr. μm)				Low water (3.0 pr. μm)			
	f_{O_2} ($\times 10^3$)	f_{CO} ($\times 10^4$)	f_{CO}/f_{O_2}	$\int[O_3]\,dz$ (μm − amagat)	f_{O_2} ($\times 10^3$)	f_{CO} ($\times 10^4$)	f_{CO}/f_{O_2}	$\int[O_3]\,dz$ (μm − amagat)
Observations	1.2 ± 0.2	6 ± 1.5	0.50 ± 0.15	1.5 ± 0.5	1.2 ± 0.2	8 ± 1.5	0.67 ± 0.17	≤ 2
Model Results								
a) Standard chemistry	1.3	1.2	0.10	1.2	1.5	2.1	0.14	1.8
b) Increase k_{27} ($H + O_2 + M$)	1.0	1.3	0.13	0.9	1.3	2.4	0.18	1.5
c) Decrease k_{29-31} ($H + HO_2$)	0.5	1.5	0.29	0.5	0.8	3.0	0.38	0.8
d) Increase k_{40} ($OH + HO_2$)	1.2	2.0	0.17	1.2	1.4	3.4	0.24	1.8
e) Decrease k_{42} ($CO + OH$)	1.1	2.9	0.26	1.1	1.5	5.1	0.35	1.7
f) Increase k_{40}, decrease k_{42}	1.3	4.9	0.40	1.1	1.5	8.5	0.57	1.7
g) Extrapolate $\sigma_{CO_2}(T)$ for $T \leq 202$ K	1.0	0.7	0.07	1.2	1.3	1.1	0.09	2.0
h) Extrapolate $\sigma_{CO_2}(T)$, modify k_{40}, k_{42}	1.1	2.7	0.25	1.2	1.3	4.7	0.35	1.9
i) Lower T by 10 K	1.0	2.4	0.24	1.0	1.2	4.4	0.37	1.3
j) Include dust cloud ($\tau = 0.2$)	1.2	1.2	0.10	1.0	1.5	2.0	0.14	1.6
k) Include heterogeneous chemistry	1.6	6.2	0.38	6.1	0.7	120	17.9	4.6

Note: f denotes surface mixing ratio and $\int[O_3]\,dz$ denotes the column integrated ozone abundance.

the altitude distribution of long lived species. Figure 10 shows reasonable agreement between model calculations of the abundances of long lived species above the homopause with Viking 1 Lander observations (Nier and McElroy 1977). Discrepancies below this level may be due to differences between our temperature profile and that experienced by the Lander. The abundance of atomic oxygen in the thermosphere has been used as a constraint on the eddy diffusion coefficient by many previous modelers (e.g., McElroy and McConnell 1971, Shimazaki 1989, Rodrigo *et al.* 1990). We have adopted an eddy diffusion coefficient of $K = 10^8\,\mathrm{cm}^2\,\mathrm{s}^{-1}$ above 100 km, which leads to a computed atomic oxygen mixing ratio at 135 km of 0.8%, consistent with the range of 0.5 – 1.0% deduced by Strickland *et al.* (1972, 1973) and in agreement with most recent photochemical models (e.g., Shimazaki 1989, Rodrigo *et al.* 1990, Krasnopolsky 1993b).

4.2 Oxygen and hydrogen escape flux

The mixing ratio of O_2 and the escape flux of atomic hydrogen are dependent upon both the eddy diffusion profile and the magnitude of the oxygen escape flux, both of which are inputs into our photochemical model. We have chosen our eddy diffusivity profile between 40 and 70 km and oxygen escape flux through an iterative process to reproduce the observed O_2 mixing ratio and atomic hydrogen escape flux. While the agreement between our model predictions and the observed quantities is not surprising, it should be noted that our eddy diffusion coefficients are consistent with those proposed by other studies.

By analyzing the Lyman-α dayglow observations returned by Mariners 6 and 7, Anderson and Hord (1971) determined the escape flux of atomic hydrogen to be $1.8 \times 10^8\ \mathrm{cm}^{-2}\ \mathrm{s}^{-1}$. In order to reproduce the observed H escape flux, our photochemical model requires an O escape flux of 1.2×10^8 atoms $\mathrm{cm}^{-2}\ \mathrm{s}^{-1}$. Including the molecular hydrogen escape flux of $2.8 \times 10^7\ \mathrm{cm}^{-2}\ \mathrm{s}^{-1}$, the total hydrogen escape

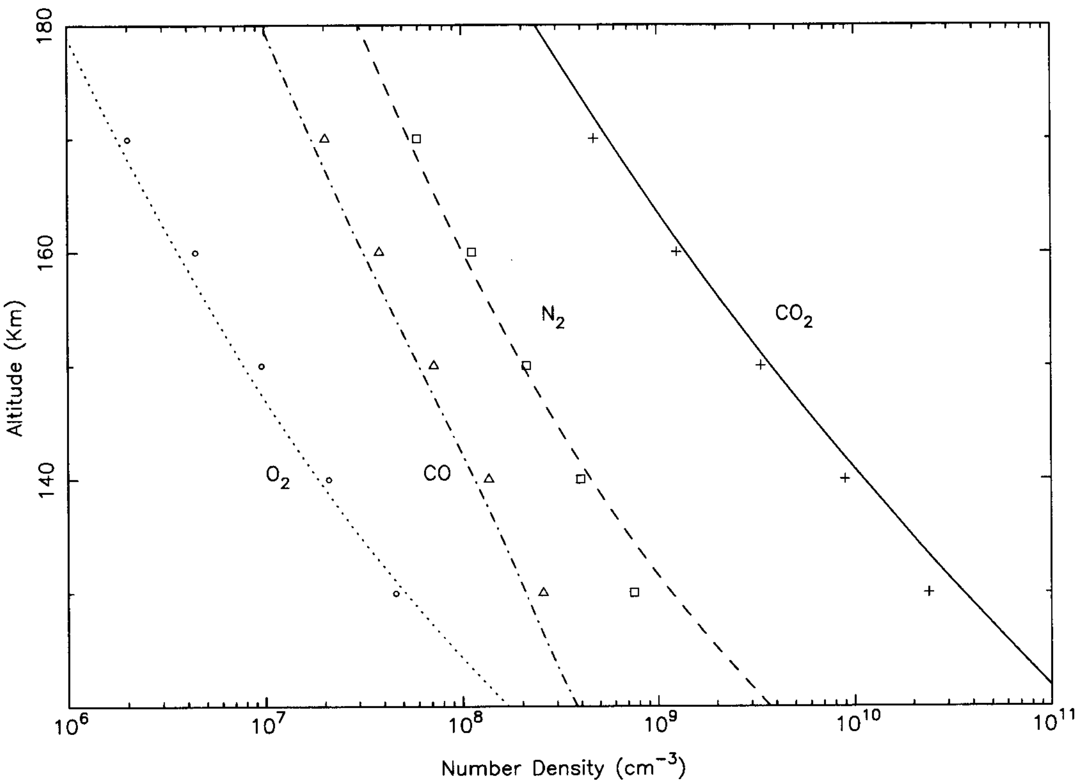

Figure 10. Computed densities (lines) and those observed by the Viking 1 Lander during its descent for CO_2 (crosses), N_2 (squares), CO (triangles) and O_2 (circles).

flux is exactly twice the oxygen escape flux, or 2.4 × 10^8 atoms cm^{-2} s^{-1}. This agrees well with the flux of 2.5 × 10^8 cm^{-2} s^{-1} found by Krasnopolsky (1993a,b).

We find a value of 3.6 × 10^{-5} for the mixing ratio of molecular hydrogen below the homopause, roughly twice the value of 2 × 10^{-5} deduced by Anderson (1974), who employed a coupled chemical-diffusive model to reproduce the observed hydrogen escape flux. The value for the rate coefficient for $CO_2^+ + H_2$ employed in his model was 1.4 × 10^{-9} cm^3 s^{-1}, which is three times larger than the value we use here. A high value for this rate coefficient would tend to lower the amount of molecular hydrogen required to produce a fixed upward flux of atomic hydrogen in a photochemical model due to the greater efficiency of H_2 destruction (see below).

Figure 11 shows our computed fluxes of H and H_2. Although the total hydrogen escape flux depends only upon the oxygen loss rate, the partitioning between thermally escaping H and H_2 is determined by the rate of vertical transport and the CO_2^+ density in the ionosphere. Molecular hydrogen transported up from the lower atmosphere is dissociated in the ionosphere via

$$\begin{array}{ll}
\text{(R94)} & CO_2 + h\nu \longrightarrow CO_2^+ + e^- \\
\text{(R102)} & H_2 + CO_2^+ \longrightarrow CO_2H^+ + H \\
\text{(R101)} & \underline{CO_2H^+ + e^- \longrightarrow CO_2 + H} \\
 & \text{net} \quad H_2 \longrightarrow 2\,H
\end{array}$$

(McElroy 1972).

Figure 12 shows our calculated ion concentration profiles with those observed by the Viking 1 Lander during its descent (Hanson *et al.* 1977). Although the observational data is poorly matched by our model, there are several differences between our model assumptions and the actual conditions experienced by the Viking 1 Lander. The descent took place at 4 pm local time with a solar zenith angle of 44°. The observations were also made at a time of low solar activity (McElroy *et al.* 1977). Our model assumes moderate solar activity and has an effective solar zenith angle of $\sim 65°$ for optical depth unity, since the optical transmission is diurnally averaged for 30° latitude at the equinox. Furthermore, we have included only a rudimentary set of ionospheric reactions; our only aim was to obtain a reasonable CO_2^+ profile. (Fox (1993a) presents a more sophisticated ionospheric model where the observations are reproduced well.)

As discussed by Hunten (1973), the diffusion limited flux is an upper limit to the flux of hydrogen that may be transported above the homopause. Its magnitude may be estimated by

$$\Phi_l \simeq \frac{b\, f_{H_2}}{H},$$

where b is the binary collision parameter, f_{H_2} is the molecular hydrogen mixing ratio,

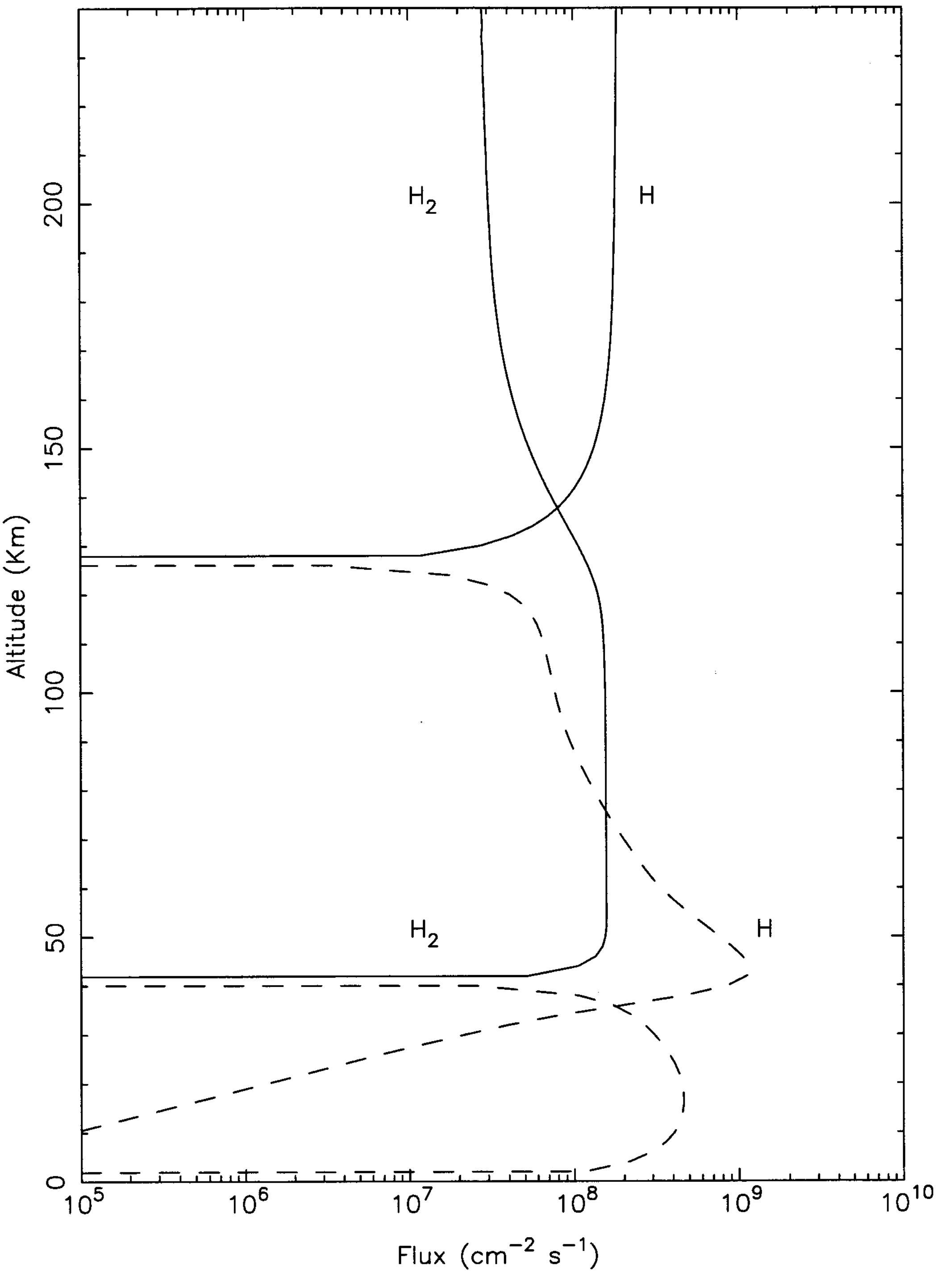

Figure 11. Computed fluxes of H and H_2. The solid lines indicate upward fluxes while the dashed lines indicate downward fluxes.

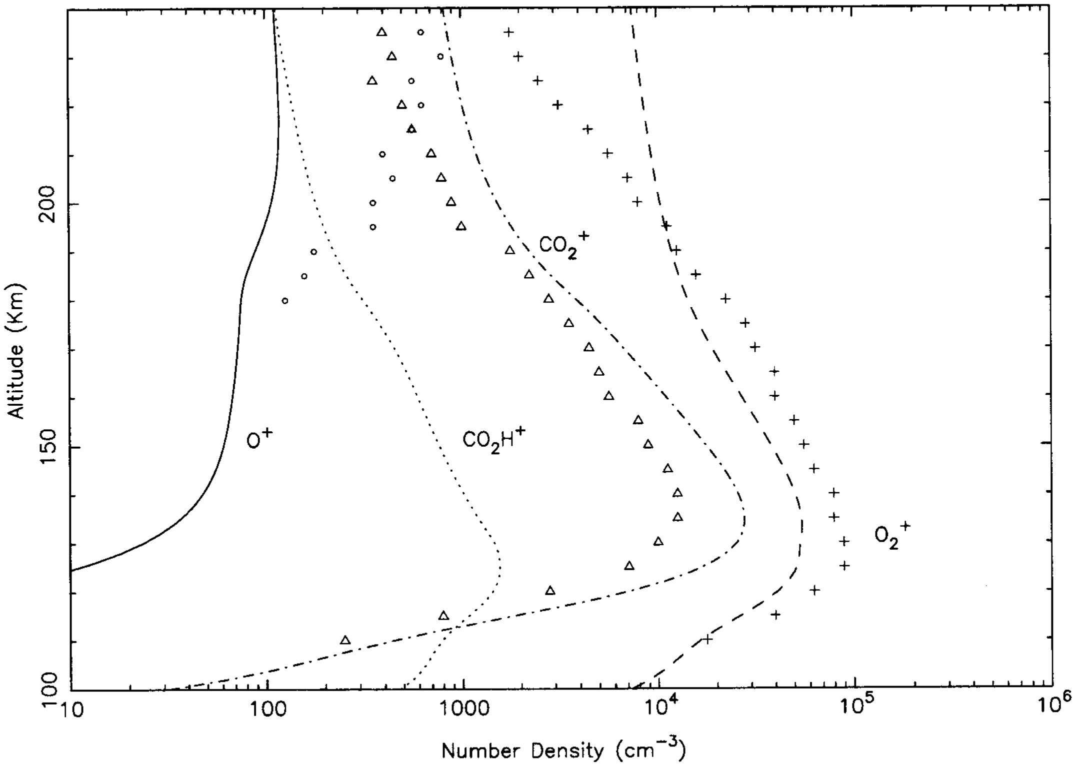

Figure 12. Computed ion densities (lines) and those observed by the Viking 1 Lander during its descent for O_2^+ (crosses), CO_2^+ (triangles), and O^+ (circles). Viking did not measure the CO_2H^+ density.

and H is the atmospheric scale height. Hunten (1973) suggested that the escape of hydrogen from Mars was indeed diffusion limited, but Liu and Donahue (1976), in their analysis of the coupling between O and H escape, found that this was not the case due to the low rate of H_2 dissociation through R102 in their model. Most recent models (e.g., Krasnopolsky 1993a,b) concur that the escape of hydrogen is not diffusion limited. Taking values appropriate for the homopause ($\sim$ 135 km), we find $\Phi_l \simeq 5 \times 10^8$ molecules cm^{-2} s^{-1} as a limiting flux for H_2 (effectively total hydrogen) from the lower atmosphere, well above the computed upward flux of 1.2×10^8 molecules cm^{-2} s^{-1} in our model. Thus our model also indicates that at the present epoch, the escape of hydrogen is limited by chemical considerations and not by transport.

The oxygen escape flux required to reproduce the observed hydrogen escape is greatly in excess of the expected flux from dissociative recombination of O_2^+, which may be computed by integrating the rate of

$$O_2^+ + e^- \longrightarrow O + O \tag{R96}$$

above the exobase, the height at which the mean free path of a particle is equal to the scale height of the background atmosphere. The original estimate of McElroy (1972) for this process was 6×10^7 cm^{-2} s^{-1}. Calculations by Zhang *et al.* (1993) indicate a comparable dissociative recombination escape flux of $\sim 5 \times 10^7$ cm^{-2} s^{-1} at the present epoch. However, Fox (1993a) pointed out that recent estimates of electron temperatures in the ionosphere range from 2000 to 3000 K, considerably larger than those used in the previously mentioned calculations. Since k_{96} is inversely proportional to T_e, estimates of the dissociative recombination of O_2^+ which incorporate high values of T_e tend to be considerably lower than previously thought. Recent Monte Carlo calculations of the oxygen escape flux from dissociative recombination by Lammer and Bauer (1991) indicate a far lower escape flux of 6×10^6 cm^{-2} s^{-1} at low solar activity and twice this at high solar activity. Fox (1993b) found a similarly low value of 3×10^6 cm^{-2} s^{-1}, a factor of forty below what is required to balance the hydrogen escape flux. Although there is some uncertainty in the H escape rate, it is unlikely that it is in error by this amount. Fox (1993b) put forth several possibilities that would increase the O escape rate to balance the observed H escape rate, such as a large loss of O through another non-thermal mechanism such as sputtering or solar wind pick-up, as suggested by Luhmann *et al.* (1992) and Zhang *et al.* (1993).

Another possibility to remove the imbalance is to postulate a substantial flux of reduced gases from the interior, such as CH_4 or H_2. Oxidation of such gases can serve as a sink for atmospheric oxygen, allowing the oxidation state of the atmosphere to be maintained without a balance in the escape rates of O and H. Although this possibility is highly unlikely, it should be noted that there has been a tentative detection of formaldehyde in the martian atmosphere from *Phobos 2* measurements (Korablev *et al.* 1993b).

Alternatively, interactions between the surface and atmosphere may account for the imbalance between the O and H escape fluxes. Indeed, Huguenin (1982) proposed that both oxidation and reduction may occur during surface weathering, and that small imbalances in the relative rates may have observable atmospheric effects, such as modifying the CO/O_2 ratio. Unfortunately, there is little data on the kinetics of such reactions on candidate martian surface materials. Photostimulated oxidation of the surface may remove up to 10^{11} atoms of oxygen and hydrogen cm^{-2} s^{-1} (Huguenin 1975, 1976), although the work of Morris and Lauer (1980) showed no evidence for UV photostimulated oxidation of magnetite. However, Morris and Lauer (1981) pointed out that the total UV irradiation in their experiments was equivalent to that received over only 10-100 years at Mars. Thus slow photooxidation of the martian surface over long timescales cannot be ruled out at this time and remains a plausible mechanism to explain the observed hydrogen escape flux.

A flux of oxygen into the surface on the order of 10^8 atoms cm^{-2} s^{-1} would be sufficient to remove the imbalance between the O and H escape fluxes. It is important to note that this flux represents the *net* loss of oxygen from the atmosphere, i.e., that in excess of the stoichiometric 1:2 flux required to balance any flux of hydrogen into the surface. Loss of oxygen through formation and deposition of nitrates and peroxynitrates is probably not a large enough sink, as Yung *et al.* (1977) estimated the magnitude of this process to be at most $\sim 10^6$ N equivalent atoms cm^{-2} s^{-1}. However, it is of interest to point out that nitrates have been found to provide a good simulation of the properties of the oxidant discovered in the martian soil during the

Viking biological experiments (Plumb *et al.* 1989).

Sizable fluxes of oxygen into the surface have a dramatic impact on the O_2 abundance, as shown by McElroy and Kong (1976), who placed an upper limit of $\sim 3.3 \times 10^7$ atoms cm^{-2} s^{-1} for the flux of oxygen into the surface over and above the 6×10^7 atoms cm^{-2} s^{-1} escaping to space in their model. We have performed a model calculation where the boundary conditions for O are a downward flux of 1.2×10^8 cm^{-2} s^{-1} at the surface and a zero flux at the top, and have found that the photochemical state of the atmosphere is unchanged from the standard model. A similar result is found if zero fluxes are imposed as boundary conditions on O and a downward flux of 6×10^7 molecules cm^{-2} s^{-1}, is assumed at the lower boundary for O_2. Thus our modeling indicates only that oxygen is irreversibly lost from the atmosphere at a rate of 1.2×10^8 atoms cm^{-2} s^{-1}, and does not discriminate between loss through either boundary. Quantification of the escape fluxes of O and H as well as laboratory studies of the rate of dry oxidation on potential martian surface materials should help resolve this question.

4.3 Ozone and carbon monoxide

The ozone abundance in our diurnally averaged model is within the observational constraints, assuming standard chemistry. However, since ozone is highly variable over the martian day, it is more appropriate to compare the observations with the computed daytime ozone abundance in a diurnally varying model. Figure 13 displays the ozone column amount over the course of a martian day for the low and high water profiles. We find that the midday ozone amount agrees well with our diurnally averaged prediction and satisfies the observational constraints, although the noontime concentration in the high water case is at the lower limit of the observed low latitude midday observations of Espenak *et al.* (1991). The temperature and water vapor profiles were not varied during the diurnal cycle in this calculation.

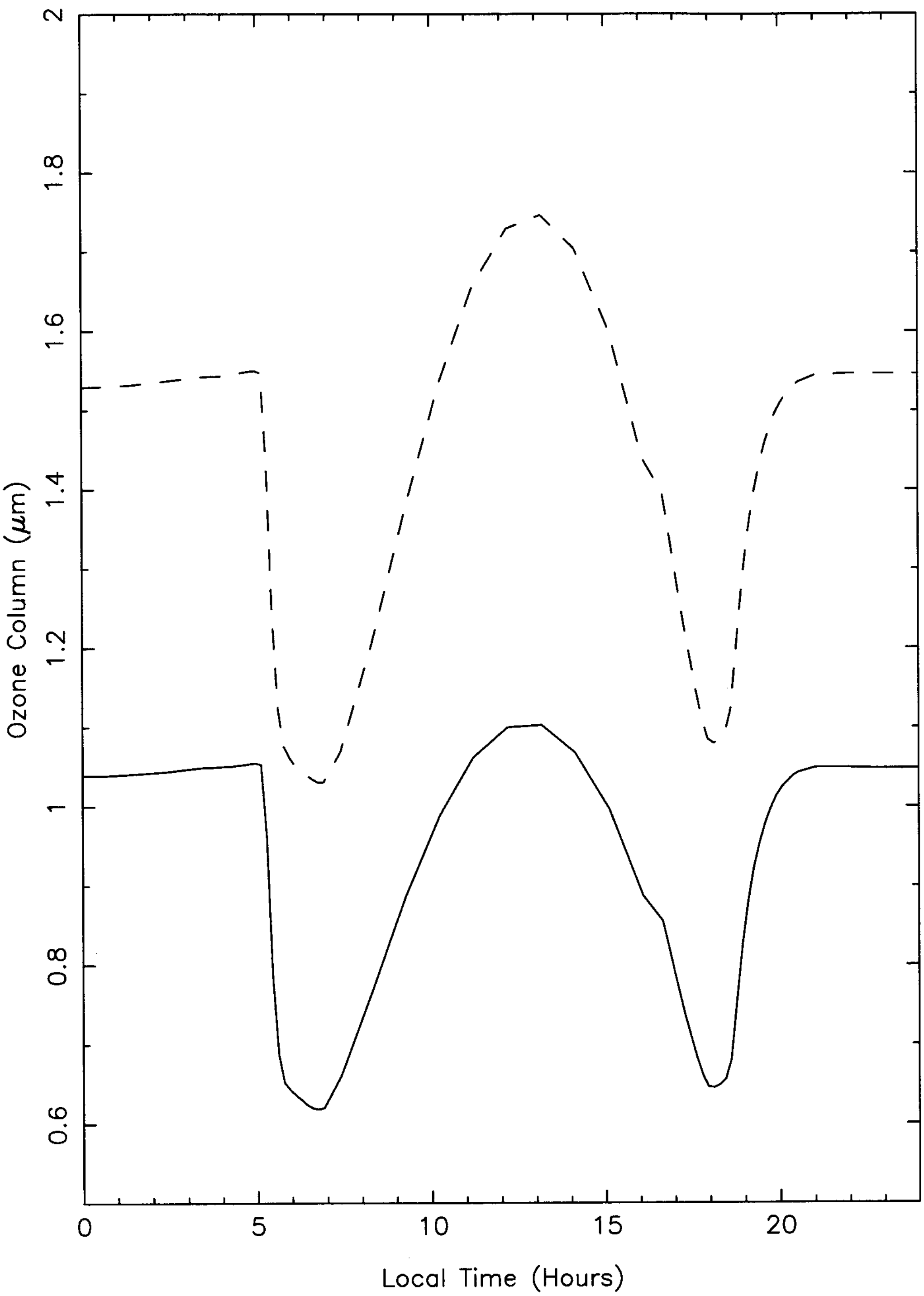

Figure 13. Diurnal variation of the ozone column abundance. The dashed line is the ozone abundance calculated with the low water profile and the solid line assumes the high water profile.

It is interesting to note that the maximum daytime and nighttime ozone column amounts are comparable despite two very different vertical profiles. Figure 14 shows the vertical profiles of atomic oxygen and ozone at noon and midnight local time, respectively, for the high water case. The loss of ozone at low altitudes at night is neatly compensated for by the large nighttime conversion of atomic oxygen to ozone at 40 to 60 km altitude. Our vertical profiles for ozone are qualitatively similar to those computed for the fall equinox by Shimazaki (1981), who performed diurnally varying calculations for 65 °N latitude over the course of an entire martian year. Krasitskii (1978) also presented a diurnal model for the martian atmosphere at 30 °N latitude and found daytime ozone column amounts of 5 to 8 $\mu\mathrm{m}$ – amagat, which are above the spectroscopic upper limit of 3 $\mu\mathrm{m}$ – amagat determined by Mariner 9, and a nighttime ozone amount of $\sim 10\,\mu\mathrm{m}$ – amagat, leading to a smaller day/night ratio than we find. Quantitative differences in our results and Krasitskii's work can be attributed to our updated rate constants and the fact that we did not account for diurnal variations in the temperature and water vapor profiles.

The ozone profile at sunset in our high water model, as shown in Fig. 15, shows a secondary peak at a concentration similar to the observed value, but is broader and higher than the peak indicated by the *Phobos 2* measurements (Blamont and Chassefière 1993), shown for comparison. Blamont and Chassefiére suggested that the observed sharp peak was due to a dramatic increase in the eddy diffusivity from $\sim 5 \times 10^5\,\mathrm{cm}^2\,\mathrm{s}^{-1}$ at 40 km to $\sim 10^7\,\mathrm{cm}^2\,\mathrm{s}^{-1}$ above 45 km. However, we do not find a better match with the *Phobos 2* ozone measurements when incorporating the preferred eddy diffusion profile of Blamont and Chassefiére in our model. Since ozone is highly variable spatially and temporally, we will not attempt to more closely match this specific profile with our globally averaged model.

The CO mixing ratio computed with the recommended rate constants is a

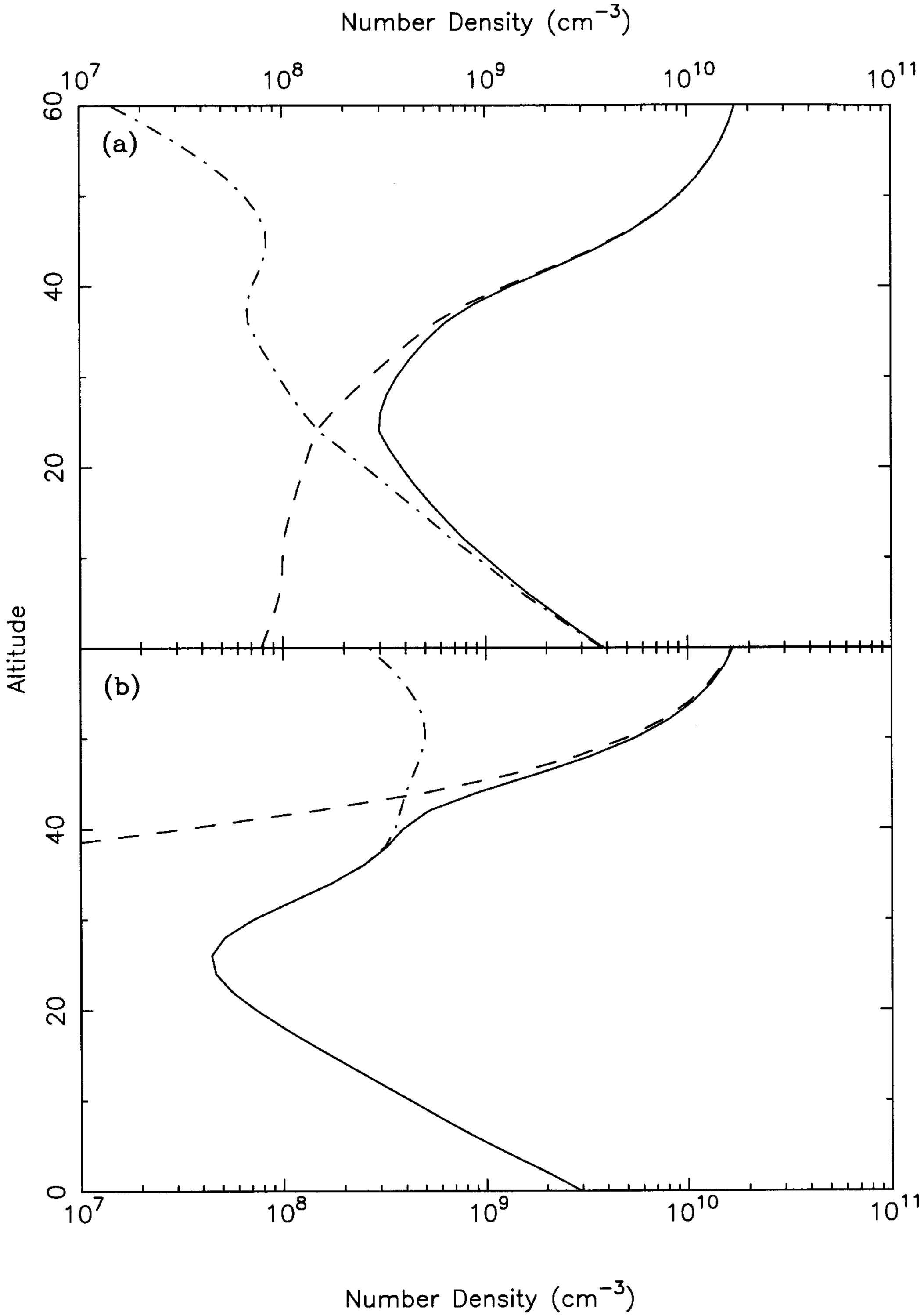

Figure 14. Odd oxygen abundances at (a) noon and (b) midnight. The solid line represents total O_x, while the dashed line represents O and the dot-dashed line represents O_3.

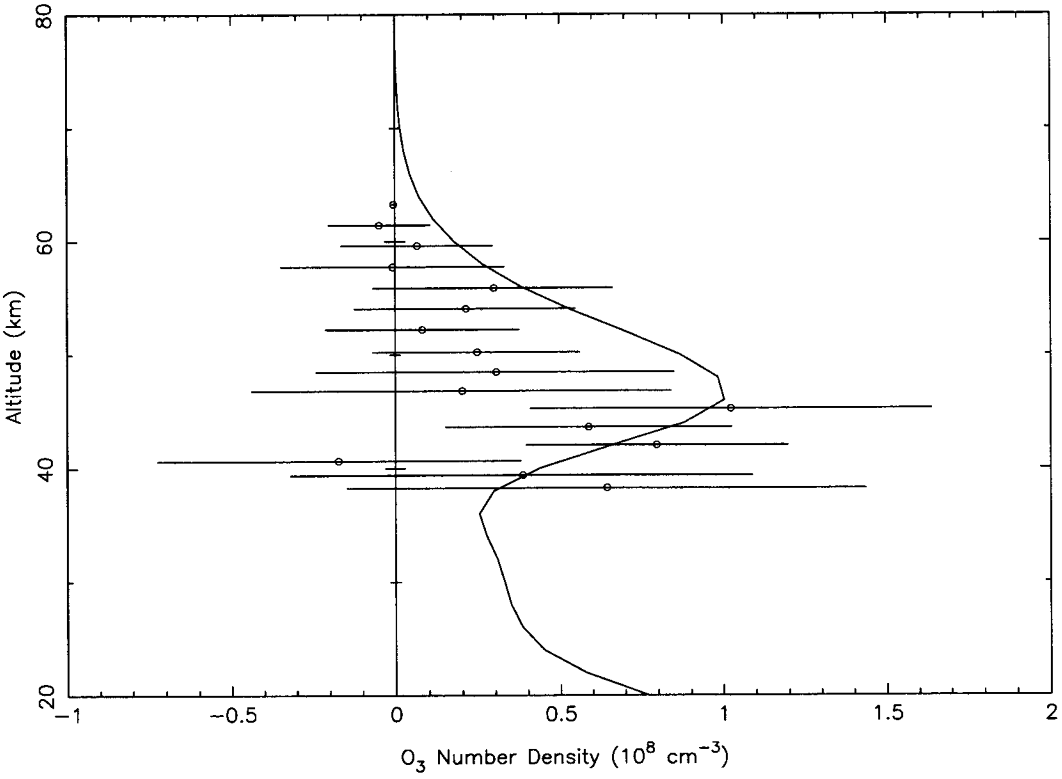

Figure 15. The computed ozone profile (solid line) at sunset compared to the *Phobos 2* measurements and 2 σ error bars.

factor of 4 to 5 below the observed amount, leading us to believe that we have either underestimated the production rate of CO or overestimated the destruction rate. Since CO is produced via photolysis of CO_2, a process for which the cross sections are well measured, it is unlikely that the production rate is in error. The destruction rate due to reaction with OH may be overestimated due to either an overabundance of OH in the model, a high value for k_{42}, or both. We shall use Eqs. 5 and 9 to guide us in the next section as we consider modifications in the input model parameters to increase the CO mixing ratio, while keeping the computed O_3 concentration unchanged.

5. Adjusted gas-phase photochemical model

5.1 Comparison with the terrestrial upper atmosphere

The failure of the model to reproduce the observed CO mixing ratio does not necessarily reflect a failure of gas phase chemistry. Most photochemical models of the terrestrial mesosphere underestimate the measured ozone density using standard chemistry. Allen *et al.* (1984) adjusted a number of rate constants, including a small (20%) increase in k_{40} ($OH + HO_2$) in order to fit Aladdin 74 observations. Rusch and Eckman (1985) found that good agreement between model and observations can be achieved only by decreasing the efficiency of HO_x catalyzed odd oxygen destruction by 30 to 50 percent. Clancy *et al.* (1987) found that a large increase in k_{40} from the JPL85 compilation (DeMore *et al.* 1985) led to markedly better agreement between modeled and observed CO and O_3 abundances. Eluszkiewicz and Allen (1993), in their analysis of the ozone budget of the upper stratosphere and lower mesosphere, suggested a 1 σ increase in k_{40} from the JPL90 recommendation to better match the ozone measurements by the LIMS instrument on the Nimbus 7 satellite. We note here that the JPL90 (DeMore *et al.* 1990) recommended rate constant for $OH + HO_2$ is 40% above the JPL85 value, which is *twice* the uncertainty quoted in JPL85! Alternatively, Clancy *et al.* (1994), in order to match observations of O_3 and HO_2 in the mesosphere, suggest a large (60 – 80%) decrease in k_{34} ($O + HO_2$).

Observations and models of CO in the terrestrial mesosphere also often disagree; the CO mixing ratio profile calculated by Allen *et al.* (1981) was substantially smaller than the observed profile. Solomon *et al.* (1985) considered the photochemistry of CO in the middle atmosphere and also found that model CO abundances are smaller than the observed amounts. They suggested that either that k_{42} ($CO + OH$) may be too high (see their Fig. 5 for the effect of reducing k_{42}) or that model OH densities are overestimated.

Shimazaki (1989) suggested revisions in k_{40} and possibly k_{29-31} ($H + HO_2$) in photochemical models of the martian atmosphere in order to balance the production and loss of CO. Krasnopolsky (1993b) examined the effect of a reduction in k_{30} on the computed hydrogen escape flux and found that a reduction larger than recommended uncertainty was required in order to bring the model into agreement with observations. Furthermore, this modification led to poor agreement between his model and the ozone data. We shall now examine the effects of adjusting these and other key rate constants in our photochemical model.

5.2 Uncertainties in kinetic rate coefficients

Contrary to the work of Yung *et al.* (1977), Krasnopolsky (1993b) has shown that NO_x chemistry is quantitatively important in the chemistry of the martian atmosphere, chiefly due to a revised rate constant for R77 ($NO + HO_2$), which is an important contributor to the breaking of the O_2 bond (refer to Table IV and Fig. 8b). However, as Krasnopolsky further showed, the impact of nitrogen chemistry on the lower atmosphere is very sensitive to the partitioning between $N(^4S)$ and $N(^2D)$ in the upper atmosphere, which is a subject of significant uncertainty. Since a detailed examination of odd nitrogen production rates is beyond the scope of this paper, we will not consider this problem here. On the other hand, while it is known that the principal loss pathway for odd nitrogen is

$$\text{(R61)} \qquad N + NO \longrightarrow N_2 + O,$$

the value of k_{61} is still somewhat uncertain. In order to match the observations of NO in the upper atmosphere made by the Viking 1 Lander, Fox (1993a) reduces the rate constant for

$$\text{(R61)} \qquad N + NO \longrightarrow N_2 + O$$

from the recommended value of 3.4×10^{-11} cm^3 s^{-1} (DeMore *et al.* 1990) to

Table VI
Proposed modifications in rate constants

Reaction	k (recommended)	k' (modified)	$\frac{k'}{k}$(200 K)
R27	$1.3 \times 10^{-27} T^{-1.6}$	$2.5 \times 10^{-26} T^{-2.1}$	1.33
R29	7.3×10^{-11}	$8.2 \times 10^{-11} e^{-100/T}$	0.68
R30	6.5×10^{-12}	$3.5 \times 10^{-12} e^{-100/T}$	0.33
R31	1.6×10^{-12}	$1.7 \times 10^{-12} e^{-100/T}$	0.64
R40	$4.8 \times 10^{-11} e^{250/T}$	$3.2 \times 10^{-11} e^{450/T}$	1.81
R42	$1.5 \times 10^{-13} (1 + 0.6\, P_{atm})$	$3.2 \times 10^{-13} e^{-300/T}$	0.48

$7.1 \times 10^{-10}\ e^{-787/T}$ cm^3 s^{-1}, the high temperature value of Davidson and Hanson (1990). We have performed a calculation where k_{61} was lowered, as suggested by Fox (1993a), and found that the O_2 mixing ratio in the model is 7.1×10^{-4}, substantially below the observed amount. In all other model calculations presented in this paper, we have adopted the recommended value of DeMore *et al.* (1990), but here we point out the importance of the assumed value for k_{61} and suggest that this rate coefficient be remeasured at temperatures appropriate to the martian atmosphere.

Many of the other rate constants we use have significant ($\sim$ 30%) uncertainties at room temperature. These uncertainties may be much larger at typical martian temperatures of $\leq$ 200 K. Table VI summarizes the modifications we have considered in the important kinetic rate constants identified in Eq. 5. The rate constants were adjusted to be consistent with the 1 σ uncertainties in both the temperature dependence and the absolute value of the rate constant at 298 K as given in the JPL90 compilation (DeMore *et al.* 1990) and to lead to an increase in the CO/O_2 ratio as would be calculated by Eq. 5.

Another uncertainty is that most of our rate constants for termolecular reactions are taken from the 1990 JPL compilation of DeMore *et al.* (1990), where the third body is assumed to be air. However, CO_2 is known to be a more efficient third body than air. We have adopted a third body efficiency of CO_2 relative to air of 2.5 in the standard model. We have also explored cases where the third body efficiency of CO_2 was as high as 3.4 relative to air. We find that changing the third body efficiency from 2.3 to 3.4 has a relatively minor effect on the CO and O_3 amounts, increasing each by less than 10%. There is a somewhat larger effect on the O_2 abundance, which decreases by $\sim$ 20%.

Table V summarizes a series of model simulations where several parameters were varied in order to better reproduce the observed abundances of CO, O_2, and O_3. The calculation made with the recommended rate constants of DeMore *et al.* (1990) is given as case a). Cases b) to f) in Table V summarize the results of our model calculations where the rate constants in Eq. 5 are varied as detailed in Table VI. All of these calculations yield an atomic hydrogen escape flux of 1.8×10^8 cm^{-2} s^{-1}, the observed value. In each case, the effect of using the suggested modified rate constant is consistent with the expected result from Eqs. 5 and 9. Figure 16 shows the mixing ratios calculated for our case f), where good agreement with all observations is achieved by increasing k_{40} and decreasing k_{42} within the recommended uncertainties. The O_3 abundance is not substantially impacted by these revisions, as expected since neither k_{40} nor k_{42} appear in Eq. 9. The column rates of some important processes in the high water case are given in Table VII. It is of interest to note the column integrated values for the dissociation of CO_2 and H_2O in the classical model of McElroy and Donahue (1972) are 1.8×10^{12} cm^{-2} s^{-1} and 2.7×10^9 cm^{-2} s^{-1}, which are a factor of 1.6 larger and a factor of 3 smaller, respectively, than in the current model, chiefly due to the incorporation of the temperature dependent cross sections of CO_2. The contributions of specific reactions to the production or loss of atmospheric constituents has been discussed previously in section IIIa.

The fact that similar revisions in k_{40} and k_{42} lead to noticeably better agree-

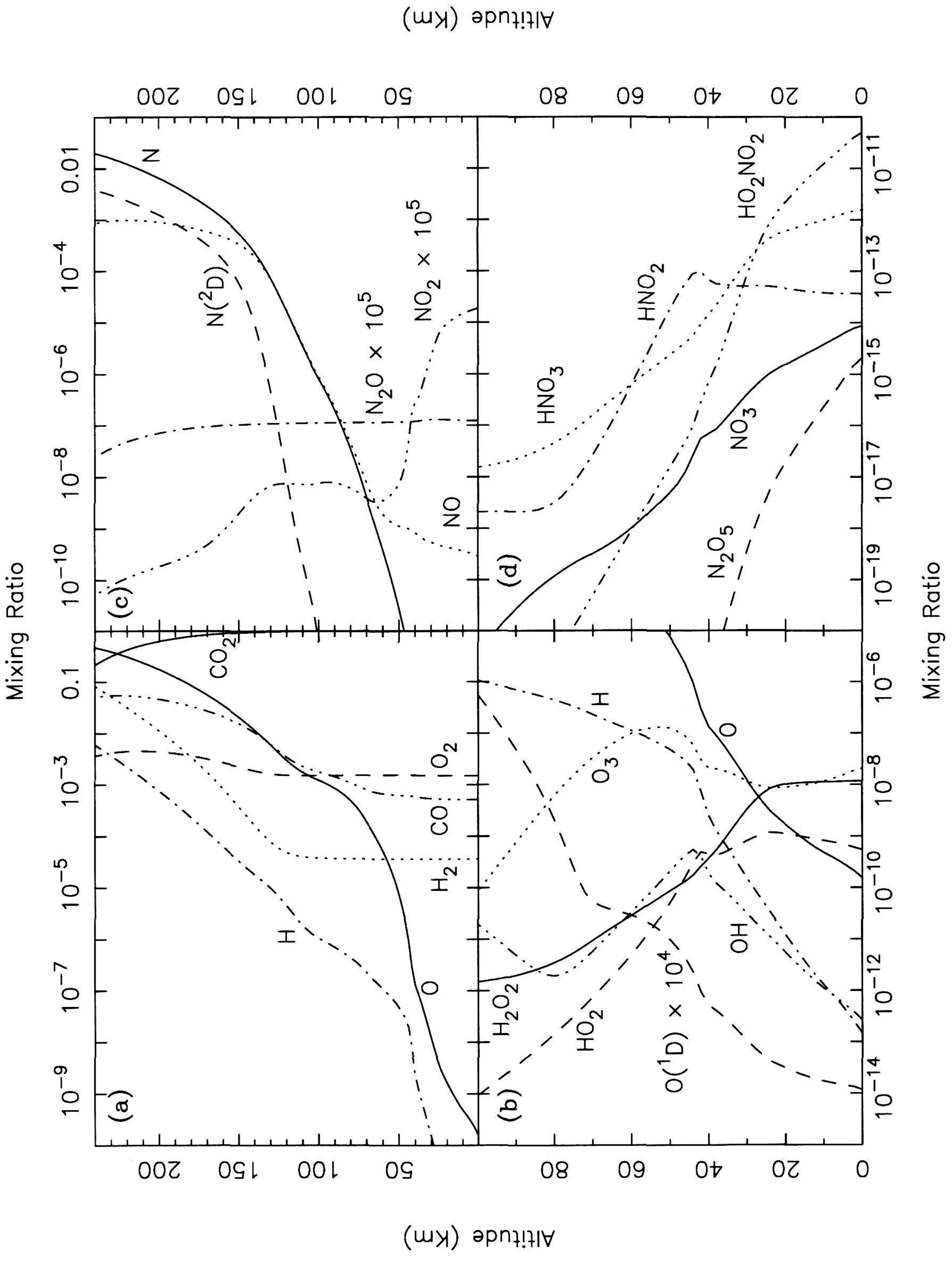

Figure 16. Altitude vs. mixing ratio profiles for the (a) major CHO, (b) HO_x and O_x, (c) major NO_x, and (d) minor NO_x species in our model, where k_{40} and k_{42} have been modified as described in the text. The integrated water abundance is 8.8 pr. μm.

Table VII
Column rates of some important reactions in the model

		Reaction			Rate (cm^{-2} s^{-1})
CO production	R13	$CO_2 + h\nu$	$\longrightarrow$	$CO + O$	9.7×10^{11}
	R14		$\longrightarrow$	$CO + O(^1D)$	1.3×10^{11}
CO loss	R42	$CO + OH$	$\longrightarrow$	$CO_2 + H$	1.1×10^{12}
O_2 production	R15	$2\,O + M$	$\longrightarrow$	$O_2 + M$	2.1×10^{10}
	R33	$O + OH$	$\longrightarrow$	$O_2 + H$	2.3×10^{11}
	R68	$O + NO_2$	$\longrightarrow$	$O_2 + NO$	2.1×10^{10}
O_2 loss	R1	$O_2 + h\nu$	$\longrightarrow$	$2\,O$	9.4×10^{10}
	R2		$\longrightarrow$	$O + O(^1D)$	1.1×10^{10}
	R8	$HO_2 + h\nu$	$\longrightarrow$	$O + OH$	2.2×10^{10}
	R12	$H_2O_2 + h\nu$	$\longrightarrow$	$2\,OH$	4.8×10^{10}
	R77	$NO + HO_2$	$\longrightarrow$	$NO_2 + OH$	8.9×10^{10}
H_2O production	R31	$H + HO_2$	$\longrightarrow$	$H_2O + O$	1.4×10^{8}
	R39	$OH + H_2$	$\longrightarrow$	$H_2O + H$	2.7×10^{8}
	R40	$OH + HO_2$	$\longrightarrow$	$H_2O + O_2$	8.4×10^{9}
	R41	$OH + H_2O_2$	$\longrightarrow$	$H_2O + HO_2$	3.1×10^{8}
H_2O loss	R9	$H_2O + h\nu$	$\longrightarrow$	$H + OH$	8.1×10^{9}
	R25	$O(^1D) + H_2O$	$\longrightarrow$	$2\,OH$	1.1×10^{9}
H_2 production	R30	$H + HO_2$	$\longrightarrow$	$H_2 + O_2$	5.7×10^{8}
H_2 loss	R23	$O(^1D) + H_2$	$\longrightarrow$	$H + OH$	1.5×10^{8}
	R39	$OH + H_2$	$\longrightarrow$	$H_2O + H$	2.7×10^{8}
N_2 production	R61	$N + NO$	$\longrightarrow$	$N_2 + O$	1.3×10^{9}
N_2 loss	R46	N_2	$\longrightarrow$	$2\,N$	6.2×10^{8}
	R47		$\longrightarrow$	$2\,N(^2D)$	7.8×10^{8}
Other HO_x cycling	R27	$H + O_2 + M$	$\longrightarrow$	$HO_2 + M$	1.2×10^{12}
	R28	$H + O_3$	$\longrightarrow$	$OH + O_2$	9.7×10^{10}
	R34	$O + HO_2$	$\longrightarrow$	$OH + O_2$	9.8×10^{11}

ment between models and observations in both the terrestrial mesosphere and martian atmosphere is remarkable. These key reaction rate constants should certainly be remeasured at temperatures and pressures appropriate to the terrestrial upper atmosphere and the martian atmosphere.

Krasnopolsky (1993b) presented a comprehensive photochemical model in which the inclusion of sulfur chemistry, a sink of odd hydrogen on aerosols, and a reduction in the water vapor absorption cross sections were required in order to bring the model into agreement with the observed state of the atmosphere. Direct comparison between Table VII and Table VIII of Krasnopolsky (1993b) yields several differences in the key reaction rates, which may be attributed to a few factors: first, Krasnopolsky employed a slower eddy diffusivity profile in his model, where K was roughly an order of magnitude smaller in the region important for O_2 formation. In order to balance the production and loss of O_2, Krasnopolsky introduced sulfur chemistry, which destroys O_2 through the reaction

$$SO + HO_2 \longrightarrow SO_2 + OH,$$

analogous to the reaction of NO and HO_2. This reaction is also an important destruction mechanism for O_2 on Venus, as first pointed out by Yung and DeMore (1982). Secondly, Krasnopolsky's water photolysis rate is smaller by a factor of five compared to our model. One reason for this is that Krasnopolsky reduced the absorption cross sections for H_2O in his model by a factor of two. As can be seen from Eq. 3, reduction of the water vapor photolysis rate constant J_9 by a factor of two is essentially equivalent to increasing k_{40} by a factor of two, as we suggest here. Also, due to a cooler temperature profile in his model, water concentrations in the middle atmosphere, where water photolysis is significant, are smaller than we assume in this paper. Finally, in order to bring the H_2 mixing ratio down to reproduce the observed atomic hydrogen escape flux, Krasnopolsky introduced a heterogeneous sink of HO_x on aerosols. However, the reaction

$$\text{(R39)} \qquad OH + H_2 \longrightarrow H_2O + H,$$

is a significant sink of H_2 that was not included in Krasnopolsky's model, which would have reduced the escape flux. Comparing these two models highlights the major uncertainties in photochemical models of the martian atmosphere, namely, the relevant rate constants, the eddy diffusivity profile, and the distribution of water vapor with altitude. The possible role of heterogeneous chemistry will be examined in a later section.

5.3 Uncertainties in photochemical cross sections

One critical assumption we have made in our previous modeling is that the absorption cross section of CO_2 is independent of temperature below 202 K. If the temperature dependence between 298 and 202 K is extrapolated to lower temperatures, the photolysis rate of water will increase beyond what we have considered previously, although Anbar *et al.* (1993a) estimated that this should not be a large effect. The water photolysis rates in each case are shown in Fig. 17.

In the standard chemistry, high water case, the integrated rate of water photolysis is 8.1×10^9 cm^{-2} s^{-1}. When we extrapolate the temperature dependence of the CO_2 cross section, we find that the column water photolysis rate jumps by nearly a factor of two, to 1.4×10^{10} cm^{-2} s^{-1}. As seen by case g) in Table V, the computed CO mixing ratio drops by a factor of two from the standard case in each of the high and low water cases. Incorporating our suggested modifications in k_{40} and k_{42}, we find that the CO mixing ratio again increases by a factor of four in each case (case h), but this is still well below the observational uncertainties.

Due to uncertainties in the cross section of water vapor longward of 1890 Å, Krasnopolsky (1993b) reduced the water vapor cross sections in his model by a factor of two and found better agreement with the computed CO mixing ratio. Atreya and Gu (1994) also examined the effect of reducing the absorption cross sections for water vapor in their photochemical model also found better agreement between the production and loss of CO_2.

The cross sections of H_2O and CO_2 longward of available measurements are

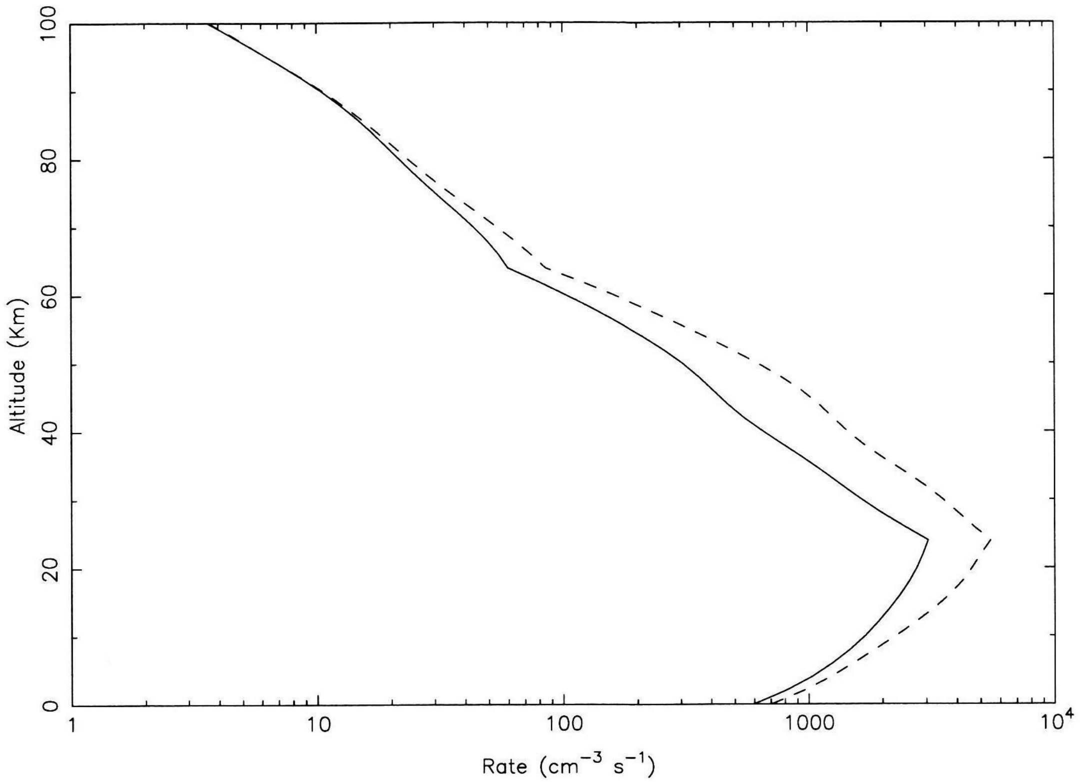

Figure 17. The effect of extrapolating the temperature dependence of the CO_2 cross section on the photolysis of H_2O. The solid line is the rate of water photolysis assuming that the cross section is independent of temperature below 202 K. The dashed line is the water photolysis rate assuming that the temperature dependence of the CO_2 cross section is equal to that between 202 and 298 K, as described in Anbar *et al.* (1993a).

also uncertainties in photochemical models. The absorption cross section of water at the long wavelength tail is taken from Thompson *et al.* (1963). We have assumed that the cross section of water is zero beyond 1975 Å. If the cross section is extrapolated out to 2100 Å, assuming a linear decrease with wavelength in the logarithm of the cross section, the column integrated photolysis rate increases 25% to 10^{10} cm^{-2} s^{-1}, accompanied by similar decreases in CO, O_2, and O_3. Most of the effect is due to the increased photolysis in the 2000-2050 Å wavelength bin. Extrapolating the cross section beyond 2100 Å has a negligible effect. Analogously extrapolating the absorption cross sections of CO_2 beyond those given by Shemansky (1972) has no appreciable effect, which is the expected result as Rayleigh scattering dominates the cross section longward of 2040 Å. Given the uncertainties in the temperature dependence of the CO_2 cross section and the long wavelength tail of the H_2O absorption, additional measurements are certainly desirable.

5.4 Uncertainties in the water profile

The rate of CO oxidation via CO + OH (R42) is dependent upon the vertical distribution of OH, which is in turn determined by the altitude distribution of water vapor. Due to the exponential dependence of the saturation vapor pressure on temperature, a small change in the temperature can provoke a large change in the water abundance in the region where water condenses. The water vapor densities measured by the *Phobos 2* spacecraft were significantly smaller at higher altitudes than the corresponding densities calculated by assuming saturation with the COSPAR temperature profile recommended by Seiff (1982), which implies a cooler thermal profile (Krasnopolsky *et al.* 1991). Clancy *et al.* (1990) showed that for cold northern spring and summer, the atmospheric temperature profile during dust free conditions leads to water vapor saturation at altitudes as low as 10 km. Recent VLA observations show the saturation altitude descending from 40 km at $L_s = 349°$ to 15 km or below at $L_s = 43°$ (Grossman *et al.* 1993, Clancy *et al.* 1993), due to variations in atmospheric temperature over the orbital period of Mars. Thus variability in the thermal structure of the lower atmosphere may have a significant impact on the photochemistry of the lower atmosphere.

Case i) in Table V shows the consequence of uniformly lowering the temperature in the lower 100 km by 10 K. As can be seen from comparing Figs. 2a and 18, this has the effect of suppressing the water density above ~ 20 km. The surface mixing ratio was increased in order to keep the column water abundance the same as in the standard cases. The column integrated water photolysis rate falls to

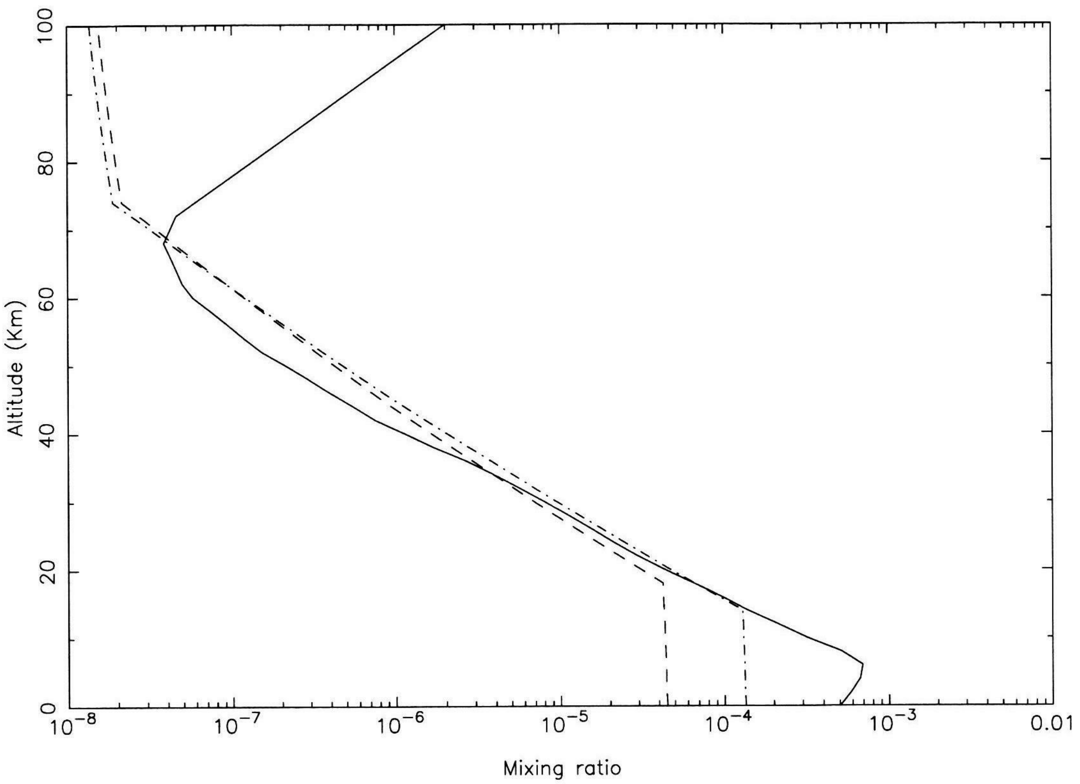

Figure 18. Water vapor profiles with temperatures in the lowest 100 km reduced by 10 K. The surface mixing ratios are the same as in Fig. 3. The dashed line is a low water profile with an integrated abundance of 8.8 pr. μm, and the dot-dashed line is a high water profile with an integrated abundance of 3.0 pr. μm. The solid line represents the saturation curve for water with the cooler temperature profile. Water densities above ~ 60 km are found by solving the coupled chemistry and transport equations.

4.4×10^9 cm^{-2} s^{-1} and the CO mixing ratio increases to 2.4×10^{-4}, a factor of two smaller and larger, respectively, from the standard chemistry, high water case. Thus a cooler thermal profile would allow us to make more moderate changes in k_{40} and k_{42} in order to bring the model CO abundance into agreement with observations. The vertical distribution of water vapor remains a significant uncertainty in the photochemistry of the martian atmosphere. Simultaneous temperature and water profiles returned by upcoming missions to Mars would be enormously useful in this regard.

6. Model with heterogeneous chemistry

One way to increase the CO/O_2 ratio might be to reduce J_9 by accounting for the absorption of solar ultraviolet radiation by aerosols in the atmosphere. Lindner (1985) examined the radiative effects of dust in the martian atmosphere and found that photolysis rates were substantially lowered in the lowest 10 km of the atmosphere. However, since the bulk of CO oxidation happens above this, where photolysis rates are largely unaffected (Fig. 4b), introducing moderate dust opacities should not have a significant impact on the CO mixing ratio in the atmosphere.

The adopted dust profile is similar to the one employed by Anbar *et al.* (1993b), which was supplied by Diane Michelangeli (private communication, 1990). The optical depth of the dust cloud is approximately 0.2. This is typical of the minimum dust loading in the atmosphere during the period of Viking observations. Recent Hubble Space Telescope images indicate that the atmosphere was considerably clearer in 1990-91 (James *et al.* 1994), with an upper limit to the optical depth of 0.1. We also account for aerosol scattering of solar radiation; we assume an average particle radius of 2.5 microns, a single scattering albedo of 0.92, and a single scattering asymmetry parameter of 0.55, after Clancy and Lee (1991). Case j) of Table V shows that incorporating the radiative effects of this dust cloud does indeed have little effect.

A more speculative notion is that HO_x radicals may be adsorbed and destroyed on aerosol surfaces, thereby reducing the sink of CO (Anbar *et al.* 1993b, Krasnopolsky 1993b, Atreya and Gu 1994). Following Anbar *et al.* (1993b), we consider the adsorption of HO_2 on dust, parameterized by:

$$\begin{array}{lrl}
\text{(R103)} & HO_2 + \text{Surface} & \longrightarrow (HO_2)_s \\
\text{(R104)} & OH + (HO_2)_s & \longrightarrow H_2O + O_2 \\
\hline
\text{net} & OH + HO_2 & \longrightarrow H_2O + O_2
\end{array}$$

We set the rate of the HO_2 adsorption reaction R103 equal to $\frac{1}{4}\gamma S v N_i$, where γ is the sticking coefficient, v the mean thermal velocity of the gas, S the mean surface area of aerosols per cm^3, and N_i the number density of HO_2. We assume a value of 0.1 for the sticking coefficient of HO_2 on dust, which is a likely upper limit (Anbar *et al.* 1993b).

This method of incorporating HO_2 adsorption is somewhat equivalent to increasing gas-phase HO_x loss via k_{40}, thus causing the CO/O_2 ratio to increase. Since HO_2 levels will be depressed, odd oxygen concentrations will rise as the reaction $O + HO_2$ (R34) is the dominant sink of O_x.

Case k) shows the results of the inclusion of heterogeneous HO_x removal reactions in the model. With the high water profile and the recommended rate constants of Table II, we find that although computed CO and O_2 abundances are in reasonable agreement with observations, the modeled ozone column is much higher than observed, as expected. Again we may invoke heterogeneous chemistry to suggest that odd oxygen is catalytically destroyed on dust grains, but we hesitate to apply heterogeneous chemistry to solve all of our modeling difficulties. In addition, the recent work of Dlugokencky and Ravishankara (1992) indicates that direct ozone loss on ice particles is insignificant. In the low water case, we find poor agreement with all three observables.

Krasnopolsky (1993b) did not find exceedingly high values for ozone when heterogeneous chemistry was incorporated into his model. This may be the result of a less vigorous eddy mixing profile, resulting in a smaller downward flux of O and hence a smaller amount of odd oxygen at low altitudes.

Thus our modeling indicates that simple scavenging of HO_x radicals on dust surfaces is an inadequate mechanism for bringing the model CO abundance back into agreement with the observations. Furthermore, there is no need to invoke a heterogeneous loss process for HO_x when reasonable modifications in a homogeneous gas-phase model provide satisfactory agreement with observations.

7. Conclusions

Following the incorporation of temperature dependent CO_2 absorption cross sections, we find that our one-dimensional photochemical model severely underestimates the mixing ratio of CO in the martian atmosphere due to a greatly enhanced water photolysis rate when purely gas phase chemistry is considered. Satisfactory agreement between our model and the observed CO abundance can be made by revising the rate constants of a few key reactions within their published recommended uncertainties. The abundances of O_2 and O_3, as well as the observed atomic hydrogen escape flux are also matched by our model. We find that it is not necessary to invoke a heterogeneous loss process for odd hydrogen, as has been suggested by several recent papers (Anbar *et al.* 1993b, Krasnopolsky 1993b, Atreya and Gu 1994). Furthermore, simple scavenging of HO_x on aerosols leads to modeled ozone amounts far higher than the observed values.

The abundances of photochemical products of CO_2 photolysis are computed self consistently; no assumptions were made regarding the surface mixing ratios of CO and/or O_2 in this model, unlike most previously published models (e.g., Liu and Donahue 1976, Kong and McElroy 1977a, Rodrigo *et al.* 1990, Krasnopolsky 1993b). Simple test cases, as summarized in Table IV, show how a minimally constrained model produces results that are consistent with intuition. Allowing the CO and O_2 abundances to be calculated self consistently also allows us to perform the first time dependent calculation demonstrating the influence of a perturbation in the oxygen escape flux on the composition of the lower atmosphere.

In order to reproduce measurements of the abundance of molecular oxygen and the escape flux of atomic hydrogen, the model calculations lead to constraints on the eddy diffusivity profile in the 40-70 km altitude range and the escape flux of atomic oxygen. We find that an oxygen escape flux of 1.2×10^8 cm^{-2} s^{-1} is required to match the observed atomic hydrogen escape flux of 1.8×10^8 cm^{-2} s^{-1} (Anderson and Hord 1971). Together with the molecular hydrogen flux of 2.8×10^7 cm^{-2} s^{-1}, the ratio of escaping H atoms to O atoms is indeed 2:1, as postulated by McElroy (1972). This O flux exceeds that expected from dissociative recombination of O_2^+, indicating that some other loss process for oxygen may be operating, such as additional escape mechanisms or weathering of oxidizable material exposed to the surface, possibly by erosion or impacts.

The fact that our postulated revisions in rate constants are similar to those proposed to resolve modeling difficulties in the terrestrial mesosphere is striking. A re-examination of the rate constants for the reactions $OH + HO_2$ and $CO + OH$ at temperatures appropriate to the martian atmosphere and the terrestrial mesosphere seems warranted. The values of these critical rate constants, the temperature dependence of the CO_2 cross section, the vertical distribution of water vapor, and the rate of vertical transport, parameterized by eddy diffusion, are major uncertainties in photochemical models of the atmosphere of Mars. Within these uncertainties, a homogeneous gas-phase model can adequately reproduce the observed abundance of CO.

Given the large fluctuations in the water vapor abundance, and the critical role odd hydrogen plays in the abundances of CO and O_2, it seems natural to suppose that the CO and O_2 mixing ratios should vary on timescales of their photochemical lifetimes, a few years. Hunten (1974) further suggested that condensation, decomposition, and sublimation of HO_2, H_2O_2, and other oxides of hydrogen may have an impact on the CO and O_2 abundances.

However, the few available observations of CO and O_2 do not suggest any significant variations. Clancy *et al.* (1983) analyzed three sets of CO observations taken over a five year period and found no compelling arguments for any variability. Furthermore, if the CO column density were to change, we would expect a similar adjustment in the O_2 column density with half the amplitude. While such a change in O_2 might be marginally detectable, observations of O_2 over the ten year period 1972-1982 (Barker 1972, Carleton and Traub 1972, Owen *et al.* 1977, and Trauger and Lunine 1983) are very consistent with one another, which may be additional evidence that the CO abundance has also remained fairly constant.

Krasnopolsky (1993a) examined the response of the CO mixing ratio to changes in solar flux over the solar cycle. He found only moderate changes in the CO mixing ratio should occur, where f_{CO} would range from 5.8×10^{-4} after solar minimum to 8.2×10^{-4} after solar maximum. All evidence thus far points to only moderate variability in the abundances of CO and O_2. In order to better resolve this question, more frequent and simultaneous measurements should be taken. Although our one-dimensional steady-state model here satisfactorily reproduces the observed state of the martian atmosphere for two quite different water abundances, a more thorough investigation of the response of the atmosphere to temporal and spatial variations in the water abundance, perhaps with a two-dimensional model, is a worthwhile endeavor.

Appendix I: Molecular diffusion coefficients

The molecular diffusion coefficient of a species i of mass m is taken to be the weighted average of the molecular diffusion coefficient of the given species through H, H_2, O, CO, and CO_2, the major constituents of the upper atmosphere of Mars. In other words:

$$D_i = \frac{[\mathrm{H}]\,D_{\mathrm{H}-i} + [\mathrm{H_2}]\,D_{\mathrm{H_2}-i} + [\mathrm{O}]\,D_{\mathrm{O}-i} + [\mathrm{CO}]\,D_{\mathrm{CO}-i} + [\mathrm{CO_2}]\,\mathrm{D}_{\mathrm{CO_2}-i}}{[\mathrm{H}] + [\mathrm{H_2}] + [\mathrm{O}] + [\mathrm{CO}] + [\mathrm{CO_2}]},$$

where

$$\begin{aligned}
D_{\mathrm{H}-i} &= \sqrt{2}\,D_{\mathrm{H}-\mathrm{H_2}} \text{ for } m_i = 1 \\
&= \frac{(D_{\mathrm{H}-\mathrm{O}} - D_{\mathrm{H}-\mathrm{H_2}})(m - m_{\mathrm{H_2}})}{m_{\mathrm{O}} - m_{\mathrm{H_2}}} + D_{\mathrm{H}-\mathrm{H_2}} \text{ for } m_i \neq 1 \\
D_{\mathrm{H_2}-i} &= \frac{\left(D_{\mathrm{H}-\mathrm{H_2}}\sqrt{m_{\mathrm{H}}/m_i} - D_{\mathrm{H_2}-\mathrm{CO_2}}\sqrt{m_{\mathrm{CO_2}}/m_i}\right)(m_{\mathrm{CO_2}} - m_i)}{m_{\mathrm{CO_2}} - m_{\mathrm{H}}} \\
D_{\mathrm{O}-i} &= D_{\mathrm{H}-\mathrm{O}}\sqrt{m_{\mathrm{H}}/m_i} \\
D_{\mathrm{CO}-i} &= D_{\mathrm{H_2}-\mathrm{CO}}\sqrt{m_{\mathrm{H_2}}/m_i} \\
D_{\mathrm{CO_2}-i} &= D_{\mathrm{H_2}-\mathrm{CO_2}}\sqrt{m_{\mathrm{H_2}}/m_i}.
\end{aligned}$$

These parameterizations fit the diffusion coefficients given in Banks and Kockarts (1973) and Mason and Marrero (1970) quite well.

The products of the pressure and binary diffusion coefficients are given by

$$\begin{aligned}
p\,D_{\mathrm{H}-\mathrm{H_2}} &= 1.13 \times 10^{-4}\,T^{1.728} \\
p\,D_{\mathrm{H}-\mathrm{O}} &= 9.87 \times 10^{-5}\,T^{1.71} \\
p\,D_{\mathrm{H_2}-\mathrm{CO}} &= \frac{1.539 \times 10^{-2}\,T}{[\log(3.16 \times 10^{7}/T)]^2}\,e^{2.8/T - 1067/T^2} \\
p\,D_{\mathrm{H_2}-\mathrm{CO_2}} &= 3.14 \times 10^{-5}\,T^{1.75}\,e^{-11.7/T},
\end{aligned}$$

where p is in atmospheres, D is in $cm^2\ s^{-1}$, and T is in Kelvin. These values are from Mason and Marrero (1970) except for $p\,D_{\mathrm{H}-\mathrm{O}}$, which is from Cooper *et al.* (1984).

Acknowledgments

We would like to express our appreciation to J.L. Fox, who provided us with odd nitrogen production rates. We also wish to thank D.M. Hunten and V.A. Krasnopolsky for helpful comments during the review process. This work was supported by NASA grant NAGW 2204 to the California Institute of Technology. Contribution number 5336 from the Division of Geological and Planetary Sciences, California Institute of Technology.

References

ALLEN, M., Y.L. YUNG, AND J.W. WATERS 1981. Vertical transport and photochemistry in the terrestrial mesosphere and lower thermosphere. *J. Geophys. Res.* **86,** 3617–3627.

ALLEN, M., AND J.E. FREDERICK 1982. Effective photodissociation cross sections for molecular oxygen and nitric oxide in the Schumann–Runge bands. *J. Atmos. Sci.* **39,** 2066–2075.

ALLEN, M., J.I. LUNINE, AND Y.L. YUNG 1984. The vertical distribution of ozone in the mesosphere and lower thermosphere. *J. Geophys. Res.* **89,** 4841–4872.

ALLEN, M., H. NAIR, Y.L. YUNG, A.D. ANBAR, AND R.T. CLANCY 1993. A homogeneous gas-phase photochemical model of the atmosphere of Mars. *Bull. Am. Astron. Soc.* **25,** 1067.

ANBAR, A.D., M. ALLEN, AND H.A. NAIR 1993a. Photodissociation in the atmosphere of Mars: Impact of high resolution, temperature-dependent CO_2 cross section measurements. *J. Geophys. Res.* **98,** 10925–10931.

ANBAR, A.D., M.T. LEU, H.A. NAIR, AND Y.L. YUNG 1993b. Adsorption of HO_x on aerosol surfaces: Implications for the atmosphere of Mars. *J. Geophys. Res.* **98,** 10933–10940.

ANDERSON, D.E. 1974. Mariner 6, 7, and 9 ultraviolet spectrometer experiment: Analysis of hydrogen Lyman-alpha data. *J. Geophys. Res.* **79,** 1513–1518.

ANDERSON, D.E., AND C.W. HORD 1971. Mariner 6 and 7 ultraviolet spectrometer experiment: Analysis of hydrogen Lyman-alpha data. *J. Geophys. Res.* **76,** 6666–6673.

ANDERSON, E., AND C. LEOVY 1978. Mariner 9 television limb observations of dust and ice hazes on Mars. *J. Atmos. Sci.* **35,** 723–734.

ANICICH, V.G. 1993. A survey of bimolecular ion-molecule reactions for use in modeling the chemistry of planetary atmospheres, cometary comae, and interstellar clouds. *Astron. Astrophys. Suppl* **84,** 215–315.

ANICICH, V.G., AND W.T. HUNTRESS 1986. A survey of bimolecular ion-molecule reactions for use in modeling the chemistry of planetary atmospheres, cometary comae, and interstellar clouds. *Astron. Astrophys. Suppl* **62,** 553–672.

ATKINSON, R., D.L. BAULCH, R.A. COX, R.F. HAMPSON JR., J.A. KERR, AND J. TROE 1989. Evaluated kinetic and photochemical data for atmospheric chemistry: Supplement III. *J. Phys. Chem. Ref. Data* **18,** 881–1097.

ATREYA, S.K. 1986. *Atmospheres and Ionospheres of the Outer Planets and Their Satellites*, Springer–Verlag, Berlin.

ATREYA, S.K., AND Z.G. GU 1994. Stability of the martian atmosphere: Is heterogeneous catalysis essential? *J. Geophys. Res.* **99** 13133–13145

BANKS, P.M., AND G. KOCKARTS 1973. *Aeronomy*, Academic Press, New York.

BARKER, E.S. 1972. Detection of molecular oxygen in the martian atmosphere. *Nature* **238,** 447–448.

BARTH, C.A. 1985. The photochemistry of the atmosphere of Mars. In *The Photochemistry of Atmospheres* (J.S. Levine, Ed.), pp. 337–392. Academic Press, Orlando, FL.

BARTH, C.A., C.W. HORD, A.I. STEWART, A.L. LANE, M.L. DUCK, AND G.P. ANDERSON 1973. Mariner 9 ultraviolet spectrometer experiment: Seasonal variation of ozone on Mars. *Science* **179,** 795–796.

BAULCH, D.L., D.D. DRYSDALE, J. DUXBURY, AND S.J. GRANT 1976. *Evaluated Kinetic Data for High Temperature Reactions. Homogeneous Gas Phase Reactions of the* O_2–O_3 *System, the* CO_2–O_2–H_2 *System and of Sulphur-Containing Species*, Butterworths, London/Boston.

BEVAN, P.L., AND G.R.A JOHNSON 1973. Kinetics of ozone formation in the pulse radiolysis of oxygen gas. *J. Chem. Soc., Faraday Trans. 2* **69,** 216–227.

BEVILACQUA, R.M., D.F. STROBEL, M.E. SUMMERS, J.J. OLIVERO, AND M. ALLEN 1990. The seasonal variation of water vapor and ozone in the upper mesosphere: Implications for vertical transport and ozone photochemistry. *J. Geophys. Res.* **95,** 883–893.

BLAMONT, J.E., AND E. CHASSEFIÈRE 1993. First detection of ozone in the middle atmosphere of Mars from solar occultation measurements. *Icarus* **104,** 324–336.

BOODAGHIANS, R.B., C.E. CANOSA-MAS, P.J. CARPENTER, AND R.P. WAYNE 1988. The reactions of NO_3 with OH and H. *J. Chem. Soc., Faraday Trans. 2* **84,** 931–948.

BROCK, J.C., AND W.T. WATSON 1980. Ozone photolysis: Determinations of the $O(^3P)$ quantum yield at 266 nm. *Chem. Phys. Lett.* **71,** 371–375.

BRUNE, W.H., J.J SCHWAB, AND J.G. ANDERSON 1983. Laser magnetic resonance, resonance fluorescence, and resonance absorption studies of the reaction kinetics $O + OH \longrightarrow H + O_2$, $O + HO_2 \longrightarrow OH + O_2$, $N + OH \longrightarrow OH + NO$, and $N + HO_2 \longrightarrow$ products at 300 K between 1 and 5 torr. *J. Phys. Chem.* **87,** 4503–4514.

Carleton, N.P., and W.A. Traub 1972. Detection of molecular oxygen on Mars. *Science* **177,** 988–992.

Chassefière, E., J.E. Blamont, V.A. Krasnopolsky, O.I. Korablev, S.K. Atreya, and R.A. West 1992. Vertical structure and size distributions of martian aerosols from solar occultation measurements. *Icarus* **97,** 46–69.

Clancy, R.T., D.O. Muhleman, and B.M. Jakosky 1983. Variability of carbon monoxide in the Mars atmosphere. *Icarus* **55,** 282–301.

Clancy, R.T, D.W. Rusch, R.J. Thomas, M. Allen, and R.S. Eckman 1987. Model ozone photochemistry on the basis of Solar Mesosphere Explorer mesospheric observations. *J. Geophys. Res.* **92,** 3067–3080.

Clancy, R.T., D.O. Muhleman, and G.L. Berge 1990. Global changes in the 0-70 km thermal structure of the Mars atmosphere derived from 1975 to 1989 microwave CO spectra. *J. Geophys. Res.* **95,** 14543–14554.

Clancy, R.T., and S.W. Lee 1991. A new look at dust and clouds in the Mars atmosphere: Analysis of emission-phase-function sequences from global Viking IRTM observations. *Icarus* **93,** 135–158.

Clancy, R.T., A.W. Grossman, and D.O. Muhleman 1992. Mapping Mars water vapor with the Very Large Array. *Icarus* **100,** 48–59.

Clancy, R.T., A.W. Grossman, and D.O. Muhleman 1993. A cold, dry, cloudy, dust-free Mars atmosphere in the 1990's. *Bull. Am. Astron. Soc.* **25,** 1060.

Clancy, R.T., B.J. Sandor, and D.W. Rusch 1994. Microwave observations and modeling of O_3, H_2O, and HO_2 in the mesosphere. *J. Geophys. Res.* **99,** 5465–5473.

COOPER, D.L., J.H. YEE, AND A. DALGARNO 1984. Energy transfer in oxygen-hydrogen collisions. *Planet. Sp. Sci.* **32,** 825–830.

DAVIDSON, D.F., AND R.K. HANSON 1990. High temperature reaction rate coefficients derived from N-atom ARAS measurements and excimer photolysis of NO. *Int. J. Chem. Kinetics* **22,** 843–861.

DEMORE, W.B., AND M. PATAPOFF 1972. Temperature and pressure dependence of CO_2 extinction coefficients. *J. Geophys. Res.* **77,** 6291–6293.

DEMORE, W.B., J.J. MARGITAN, M.J. MOLINA, R.T. WATSON, D.M. GOLDEN, R.F. HAMPSON, M.J. KURYLO, C.J. HOWARD, AND A.R. RAVISHANKARA 1985. *Chemical Kinetics and Photochemical Data for Use in Stratospheric Modeling, Evaluation Number 7,* JPL Publication 85-37.

DEMORE, W.B., S.P. SANDER, D.M. GOLDEN, M.J. MOLINA, R.F. HAMPSON, M.J. KURYLO, C.J. HOWARD, AND A.R. RAVISHANKARA 1990. *Chemical Kinetics and Photochemical Data for Use in Stratospheric Modeling, Evaluation Number 9,* JPL Publication 90-1.

DEMORE, W.B., S.P. SANDER, D.M. GOLDEN, R.F. HAMPSON, M.J. KURLYO, C.J. HOWARD, A.R. RAVISHANKARA, C.E. KOLB, AND M.J. MOLINA 1992. *Chemical Kinetics and Photochemical Data for Use in Stratospheric Modeling, Evaluation Number 10,* JPL Publication 92-20.

DLUGOKENCKY, E.J., AND A.R. RAVISHANKARA 1992. Laboratory measurements of direct ozone loss on ice and doped-ice surfaces. *Geophys. Res. Lett.* **19,** 41–44.

ELUSZKIEWICZ, J.E. AND M. ALLEN 1993. A global analysis of the ozone deficit in the upper stratosphere and lower mesosphere. *J. Geophys. Res.* **98,** 1069–1082.

ESPENAK, F., M.J. MUMMA, T. KOSTIUK, AND D. ZIPOY 1991. Ground-based infrared measurements of the global distribution of ozone in the atmosphere of Mars. *Icarus* **92,** 252–262.

FAIRCHILD, C.E., E.J. STONE, AND G.M. LAWRENCE 1978. Photofragment spectroscopy of ozone in the uv region 270-310 nm and at 600 nm. *J. Chem. Phys.* **69,** 3632–3638.

FELL, C., J.I. STEINFELD, AND S. MILLER 1990. Quenching of N(^{2}D) by O(^{3}P). *J. Chem. Phys.* **92,** 4768–4777.

FOX, J.L. 1993a. The production and escape of nitrogen atoms on Mars. *J. Geophys. Res.* **98,** 3297–3310.

FOX, J.L. 1993b. On the escape of oxygen and hydrogen from Mars. *Geophys. Res. Lett.* **20,** 1847–1850.

GROSSMAN, A.W., R.T. CLANCY, AND D.O. MUHLEMAN 1993. Microwave limb-sounding of martian water vapor. *Bull. Am. Astron. Soc.* **25,** 1060.

HALL, I.W., R.P. WAYNE, R.A. COX, M.E. JENKIN, AND G.D. HAYMAN 1988. Kinetics of the reaction of NO_3 with HO_2. *J. Phys. Chem.* **92,** 5049–5054.

HANSON, W.B., S. SANATANI, AND D.R. ZUCARRO 1977. The martian ionosphere as observed by the Viking retarding potential analyzers. *J. Geophys. Res.* **82,** 4351–4363.

HUGUENIN, R.L. 1975. Surface oxidation: A major sink for water on Mars. *Science* **192,** 138–139.

HUGUENIN, R.L. 1976. Mars: Chemical weathering as a massive volatile sink. *Icarus* **28,** 203–212.

HUGUENIN, R.L. 1982. Chemical weathering and the Viking biology experiments on Mars. *J. Geophys. Res.* **87,** 10069–10082.

HUNTEN, D.M. 1973. The escape of light gases from planetary atmospheres. *J. Atmos. Sci.* **30,** 1481–1494.

HUNTEN, D.M. 1974. Aeronomy of the lower atmosphere of Mars. *Rev. Geophys. Space Phys.* **12,** 529–535.

IZAKOV, M.N., AND O.P. KRASITSKII 1977. A model for the composition of the martian atmosphere. *Kosmicheskie Issledovaniya* **15,** 455–469.

JAKOSKY, B.M. 1985. The seasonal cycle of water on Mars. *Space Sci. Rev.* **41,** 131–200.

JAKOSKY, B.M., AND C.B. FARMER 1982. The seasonal and global behavior of water vapor in the Mars atmosphere: Complete global results of the Viking atmospheric water detector experiment. *J. Geophys. Res.* **87,** 2999–3019.

JAMES, P.B., R.T. CLANCY, S.W. LEE, L.J. MARTIN, R.B. SINGER, E. SMITH, R.A. KAHN, AND R.P. ZUREK 1994. Monitoring Mars with the Hubble Space Telescope: 1990-91 observations. *Icarus*, in press.

KAHN, R. 1990. Ice haze, snow, and the Mars water cycle. *J. Geophys. Res.* **95,** 14677–14693.

KAPLAN, L.D., J. CONNES, AND P. CONNES 1969. Carbon monoxide in the martian atmosphere. *Astrophys. J.* **157,** L187–L192.

KAUFMAN, F., AND J.R. KELSO 1967. M effect in the gas-phase recombination of O with O_2. *J. Chem. Phys.* **46,** 4541–4543.

KEYSER, L.F. 1986. Absolute rate constant and branching fractions of the $H + HO_2$ reaction from 245 to 300 K. *J. Phys. Chem.* **90,** 2994–3003.

KO, T., AND A. FONTIJIN 1991. High-temperature photochemistry kinetics study of the reaction $H + NO_2 \longrightarrow OH + NO$ from 296 to 760 K. *J. Phys. Chem.* **95,** 3984–3987.

KONG, T.Y., AND M.B. MCELROY 1977a. Photochemistry of the martian atmosphere. *Icarus* **32,** 168–189.

KONG, T.Y., AND M.B. MCELROY 1977b. The global distribution of O_3 on Mars. *Planet. Sp. Sci.* **25,** 839–857.

KORABLEV, O.I., V.A. KRASNOPOLSKY, A.V. RODIN, AND E. CHASSEFIÈRE 1993a. Vertical structure of martian dust measured by solar infrared occultations from the *Phobos* spacecraft. *Icarus* **102,** 76–87.

KORABLEV, O.I., M. ACKERMAN, V.A. KRASNOPOLSKY, V.I. MOROZ, C. MULLER, A.V. RODIN, AND S.K. ATREYA 1993b. Tentative identification of formaldehyde in the martian atmosphere. *Planet. Sp. Sci.* **41,** 441–451.

KRASITSKII, O.P. 1978. A model for the diurnal variations of the composition of the martian atmosphere. *Kosmicheskie Issledovaniya* **16,** 434–442.

KRASNOPOLSKY, V.A. 1977. Ultraviolet photometry of Mars by the satellite *Mars-5*. *Kosmicheskie Issledovaniya* **15,** 255-259.

KRASNOPOLSKY, V.A. 1986. *Photochemistry of the Atmospheres of Mars and Venus*, Springer–Verlag, Berlin.

KRASNOPOLSKY, V.A. 1993a. Solar cycle variations of the hydrogen escape rate and the CO mixing ratio on Mars. *Icarus* **101,** 33–41.

KRASNOPOLSKY, V.A. 1993b. Photochemistry of the martian atmosphere (mean conditions). *Icarus* **101,** 313–332.

KRASNOPOLSKY, V.A., AND V.A. PARSHEV 1979. Ozone and photochemistry of the martian lower atmosphere. *Planet. Sp. Sci.* **27,** 113-120.

KRASNOPOLSKY, V.A., O.I. KORABLEV, V.I. MOROZ, A.A. KRYSKO, J.E. BLAMONT, AND E. CHASSEFIÈRE 1991. Infrared solar occultation sounding of the martian atmosphere by the *Phobos* spacecraft. *Icarus* **94,** 32–44.

KRONEBUSCH, P.I., AND J. BERKOWITZ 1976. Photodissociative ionization in the 21–41 eV region: O_2, N_2, CO, NO, CO_2, H_2O, NH_3, and CH_4. *Int. J. Mass Spectrom. Ion Process* **12,** 283–306.

LAMMER, H., AND S.J. BAUER 1991. Nonthermal atmospheric escape from Mars and Titan. *J. Geophys. Res.* **96,** 1819–1825.

LEE, L.C., T.G. SLANGER, G. BLACK, AND R.L. SHARPLESS 1977. Quantum yields for the production of $O(^1D)$ from photodissociation of O_2 at 1160–1770 Å. *J. Chem. Phys.* **67,** 5602–5606.

LELLOUCH, E., G. PAUBERT, AND T. ENCRENAZ 1991. Mapping of CO millimeter-wave lines in Mars' atmosphere — the spatial variability of carbon monoxide on Mars. *Planet. Sp. Sci.* **39,** 219–254.

LEWIS, B.R., AND J.H. CARVER 1983. Temperature dependence of the carbon dioxide photoabsorption cross section between 1200 and 1970 Å. *J. Quant. Spectrosc. Radiat. Transf.* **30,** 297–309.

LIN, C.L., AND M.T. LEU 1982. Temperature and third-body dependence of the rate constant for the reaction $O + O_2 + M \longrightarrow O_3 + M$. *Int. J. Chem. Kinetics* **14,** 417–434.

LINDNER, B.L. 1985. *The aeronomy and radiative transfer of the martian atmosphere*, Ph.D. Thesis, University of Colorado..

LINDNER, B.L. 1988. Ozone on Mars: The effects of clouds and airborne dust. *Planet. Sp. Sci.* **36,** 125–144.

LIU, S.C., AND T.M. DONAHUE 1976. The regulation of hydrogen and oxygen escape from Mars. *Icarus* **28,** 231–246.

LUHMANN, J.G., R.E. JOHNSON, M.H.G. ZHANG 1992. Evolutionary impact of sputtering of the martian atmosphere by O^+ pickup ions. *Geophys. Res. Lett.*

19, 2151–2154.

MAGNOTTA, F., AND H.S. JOHNSTON 1980. Photodissociation quantum yields for the NO_3 free radical. *Geophys. Res. Lett.* **7,** 769–772.

MASON, E.A., AND T.R. MARRERO 1970. The diffusion of atoms and molecules. In *Advances in atomic and molecular physics* (D.R. Bates and I. Estermann, Eds.), pp. 155–231. Academic Press, New York.

MASUOKA, T., AND J.A.R. SAMSON 1980. Dissociative and double photoionization of CO_2 from threshold to 90 Å. *J. de Chim. Phys.* **77,** 623–630.

MCELROY, M.B. 1972. Mars: An evolving atmosphere. *Science* **175,** 443–445.

MCELROY, M.B. 1973. Atomic and molecular processes in the martian atmosphere. In *Advances in Atomic and Molecular Physics* (D.R. Bates and I. Estermann, Eds.), pp. 323–363. Academic Press, New York and London.

MCELROY, M.B., AND D.M. HUNTEN 1970. Photochemistry of CO_2 in the atmosphere of Mars. *J. Geophys. Res.* **75,** 1188–1201.

MCELROY, M.B., AND J.C. MCCONNELL 1971. Dissociation of CO_2 in the martian atmosphere. *J. Atmos. Sci.* **28,** 879–884.

MCELROY, M.B., AND T.M. DONAHUE 1972. Stability of the martian atmosphere. *Science* **177,** 986–988.

MCELROY, M.B., AND T.Y. KONG 1976. Oxidation of the martian surface: Constraints due to chemical processes in the atmosphere. *Geophys. Res. Lett.* **3,** 569–572.

MCELROY, M.B., T.Y. KONG, AND Y.L. YUNG 1977. Photochemistry and evolution of Mars' atmosphere: A Viking perspective. *J. Geophys. Res.* **82,** 4379–4388.

MELLOUKI, A., G. LEBRAS, AND G. POULET 1988. Kinetics of the reactions of NO_3 with OH and HO_2. *J. Phys. Chem.* **92,** 2229–2234.

MENTALL, J.E., AND E.P. GENTIEU 1970. Lyman-α fluorescence from the photodissociation of H_2. *J. Chem. Phys.* **52,** 5641–5645.

MICHELANGELI, D.V., M. ALLEN, Y.L. YUNG, R.L. SHIA, D. CRISP, AND J. ELUSZKIEWICZ 1992. Enhancement of atmospheric radiation by an aerosol layer. *J. Geophys. Res.* **97,** 865–874.

MORRIS, R.V., AND H.V. LAUER 1980. The case against UV photostimulated oxidation of magnetite. *Geophys. Res. Lett.* **7,** 605–608.

MORRIS, R.V., AND H.V. LAUER 1981. Stability of goethite ($\alpha-$FeOOH) and lepidocrocite ($\gamma-$FeOOH) to dehydration by UV radiation: Implications for their occurrence on the martian surface. *J. Geophys. Res.* **86,** 10893–10899.

MOUNT, G.H., AND G.J. ROTTMAN 1981. The solar spectral irradiance 1200–3184 Å near solar maximum: 15 July 1980. *J. Geophys. Res.* **86,** 9193–9198.

MOUNT, G.H., AND G.J. ROTTMAN 1982. The solar absolute spectral irradiance 1150–3173 Å: 17 May 1982. *J. Geophys. Res.* **88,** 5403–5410.

NAIR, H., M. ALLEN, AND Y.L. YUNG 1991. Regulation of CO and O_2 abundances by the escape of oxygen and hydrogen in the atmosphere of Mars. *Bull. Am. Astron. Soc.* **23,** 1213.

NAIR, H., M. ALLEN, Y.L. YUNG, AND R.T. CLANCY 1992. martian atmospheric chemistry during the time of low water abundance. *LPI Contrib.* **787,** 21.

NEE, J.B., AND L.C. LEE 1984. Photoabsorption cross sections of OH at 115-183 nm. *J. Chem. Phys.* **81,** 31–36.

NICOLET, M. 1984. On the molecular scattering in the terrestrial atmosphere: An empirical formula for its calculation in the homosphere. *Planet. Sp. Sci.* **32,** 1467–1468.

NIER, A.O., AND M.B. MCELROY 1977. Composition and structure of Mars' upper atmosphere: Results from the neutral mass spectrometers on Viking 1 and 2. *J. Geophys. Res.* **82,** 4341–4349.

OWEN, T., K. BIEMANN, D.R. RUSHNECK, J.E. BILLER, D.W. HOWARTH, AND A.L. LAFLEUR 1977. The composition of the atmosphere at the surface of Mars. *J. Geophys. Res.* **82,** 4635–4639.

PARISOT, J.P., AND J.M. ZUCCONI 1984. Temperature effect on the photodissociation rates in the atmospheres of Mars and Venus. *Icarus* **60,** 327–331.

PARKINSON, T.M., AND D.M. HUNTEN 1972. Spectroscopy and aeronomy of O_2 on Mars. *J. Atmos. Sci.* **29,** 1380–1390.

PHILLIPS, E., L.C. LEE, AND D.L. JUDGE 1977. Absolute photoabsorption cross sections for H_2O and D_2O from λ 180–790 Å. *J. Quant. Spectrosc. Radiat. Transf.* **18,** 309–313.

PIPER, L.G., M.E. DONAHUE, AND W.T. RAWLINS 1987. Rate coefficients for $N(^2D)$ reactions. *J. Phys. Chem.* **91,** 3883–3888.

PLUMB, R.C., R. TANTAYANON, M. LIBBY, AND W.W. XU 1989. Chemical model for Viking biology experiments: Implications for the composition of the martian regolith. *Nature* **338,** 633–635.

RIZK, B., W.K. WELLS, D.M. HUNTEN, C.R. STOKER, R.S. FREEDMAN, T. ROUCH, J.B. POLLACK, AND R.M. HABERLE 1991. Meridional martian water abundance profiles during the 1988–1989 season. *Icarus* **90,** 205–213.

RODRIGO, R., E. GARCÍA-ÁLVAREZ,, M.J. LÓPEZ-GONZÁLEZ, AND J.J. LÓPEZ-MORENO 1990. A nonsteady one-dimensional theoretical model of Mars' neutral atmospheric composition between 30 and 200 km. *J. Geophys. Res.* **95,** 14795–

14810.

RUSCH, D.W., AND R.S. ECKMAN 1985. Implications of the comparison of ozone abundances measured by the Solar Mesosphere Explorer to model calculations. *J. Geophys. Res.* **90,** 12991–12998.

SAMSON, J.A.R., G.H. RAYBORN, AND P.N. PAREEK 1982. Dissociative photoionization cross sections of O_2 from threshold to 120 Å. *J. Chem. Phys.* **76,** 393–397.

SAMSON, J.A.R., AND P.N. PAREEK 1985. Absolute photoionization cross sections of atomic oxygen. *Phys. Rev. A* **31,** 1470–1476.

SCHOFIELD, K. 1979. Critically evaluated rate constants for gaseous reactions of several electronically excited species. *J. Phys. Chem. Ref. Data* **8,** 723–798.

SCHÜRGERS, M., AND K.H. WELGE 1968. Absorptionskoeffizient von H_2O_2 und N_2H_4 zwischen 1200 und 2000 Å. *Z. Naturforsch.* **23a,** 1508–1510.

SEIFF, A. 1982. Post-Viking models for the structure of the summer atmosphere of Mars. *Adv. Space Res.* **2,** 3–17.

SHEMANSKY, D.E. 1972. CO_2 extinction coefficient 1700–3000 Å. *J. Chem. Phys.* **56,** 1582–1587.

SHIMAZAKI, T. 1981. A model of temporal variations in ozone density in the martian atmosphere. *Planet. Sp. Sci.* **29,** 21–33.

SHIMAZAKI, T. 1989. Photochemical stability of CO_2 in the martian atmosphere: Reevaluation of the eddy diffusion coefficient and the role of water vapor. *J. Geomag. Geoelectr.* **41,** 273–301.

SHIMAZAKI, T., AND M. SHIMUZU 1979. The seasonal variation of ozone density in the martian atmosphere. *J. Geophys. Res.* **84,** 1269–1276.

SOLOMON, S., R.R. GARCIA, J.J. OLIVERO, R.M. BEVILACQUA, P.R. SCHWARTZ, R.T. CLANCY, AND D.O. MUHLEMAN 1985. Photochemistry and transport of carbon monoxide in the middle atmosphere. *J. Atmos. Sci.* **42,** 1072–1083.

SPARKS, R.K., L.R. CARLSON, K. SHOBATAKE, M.L. KOWALCZYK, AND Y.T. LEE 1980. Ozone photolysis: A determination of the electronic and vibrational state distributions of primary products. *J. Chem. Phys.* **72,** 1401–1402.

STEWART, A.J. AND W.B. HANSON 1982. Mars' upper atmosphere: mean and variations. *Adv. Space Res.* **2,** 87–101.

STRICKLAND, D.J., G.E. THOMAS, AND P.R. SPARKS 1972. Mariner 6 and 7 ultraviolet spectrometer experiment: Analysis of the O I 1304- and 1356-Å emissions. *J. Geophys. Res.* **77,** 4052–4068.

STRICKLAND, D.J., A.I. STEWART, C.A. BARTH, C.W. HORD, AND A.L. LANE 1973. Mariner 9 ultraviolet spectrometer experiment: Mars atomic oxygen 1304-Å Emission. *J. Geophys. Res.* **78,** 4547–4559.

STROBEL, D.F., M.E. SUMMERS, R.M. BEVILACQUA, M.T. DELAND, AND M. ALLEN 1987. Vertical constituent transport in the mesosphere. *J. Geophys. Res.* **92,** 6691–6698.

TAHERIAN, M.R. AND T.G. SLANGER 1985. Products and yields from O_3 photodissociation at 1576 Å. *J. Chem. Phys.* **83,** 6246–6250.

THOMPSON, B.A., P. HARTECK, AND R.R. REEVES 1963. Ultraviolet absorption coefficients of CO_2, CO, O_2, H_2O, N_2O, NH_3, NO, SO_2 and CH_4 between 1850 and 4000 Å. *J. Geophys. Res.* **68,** 6431–6436.

TOON, O.B., J.B. POLLACK, AND C. SAGAN 1977. Physical properties of the particles composing the martian dust storm of 1971–1972. *Icarus* **30,** 663–696.

TORR, M.R., AND D.G. TORR 1985. Ionization frequencies for solar cycle 21: Revised. *J. Geophys. Res.* **90,** 6675–6678.

TRAUGER, J.T., AND J.I. LUNINE 1983. Spectroscopy of molecular oxygen in the atmospheres of Venus and Mars. *Icarus* **55,** 272–281.

TSANG, W., AND R.F. HAMPSON 1986. Chemical kinetic data base for combustion chemistry. Part 1. Methane and related compounds. *J. Phys. Chem. Ref. Data* **15,** 1087–1279.

TURNIPSEED, A.A., G.L. VAGHJIANI, T. GIERCZAK, J.E., THOMPSON, AND A.R. RAVISHANKARA 1991. The photochemistry of ozone at 193 and 222 nm. *J. Chem. Phys.* **95,** 3244–3251.

VAN DISHOECK, E.F., AND A. DALGARNO 1984. Photodissociation of OH in interstellar clouds. *Astrophys. J.* **277,** 576–580.

VAN DISHOECK, E.F., M.C. VAN HEMERT, A.C. ALLISON, AND A. DALGARNO 1984. Resonances in the photodissociation of OH by absorption into coupled $^2\Pi$ states: Adiabatic and diabatic formulations. *J. Chem. Phys.* **81,** 5709–5724.

WASHBURN, E.W. 1924. The vapor pressure of ice and of water below the freezing point. *Monthly Weather Review,* 488–490.

WINE, P.H., AND A.R. RAVISHANKARA 1982. O_3 photolysis at 248 nm and $O(^1D_2)$ quenching by H_2O, CH_4, H_2, and N_2O : $O(^3P_J)$ yields. *Chem. Phys.* **69,** 365–373.

WMO 1985. *Atmospheric Ozone*, World Meteorological Organization Report No. 16.

YUNG, Y.L., D.F. STROBEL, T.Y. KONG, AND M.B. MCELROY 1977. Photochemistry of nitrogen in the martian atmosphere. *Icarus* **30,** 26–41.

YUNG, Y.L., AND W.B. DEMORE 1982. Photochemistry of the stratosphere of Venus: Implications for atmospheric evolution. *Icarus* **51,** 199–247.

YUNG, Y.L., J.S. WEN, J.P. PINTO, M. ALLEN, K.K. PIERCE, AND S. PAULSON 1988. HDO in the martian atmosphere: Implications for the abundance of crustal water. *Icarus* **76,** 146–159.

ZHANG, M.H.G., J.G. LUHMANN, S.W. BOUGHER, AND A.F. NAGY 1993. The ancient oxygen exosphere of Mars: Implications for atmosphere evolution. *J. Geophys. Res.* **98,** 10915–10923.

Paper II

A Study of Ozone in the Northern Winter Stratosphere Using a Lagrangian Photochemical Model: An Analysis of UARS Observations

Abstract

Photochemical models have historically overestimated ozone loss rates in the upper stratosphere and lower mesosphere, where ozone is photochemically controlled. Thus it is evident that there is some missing chemistry in current models. Current understanding of the factors controlling ozone in the low to mid stratosphere is that dynamical influences play a large role in determining the ozone abundance. It is difficult to test the chemistry in the models at these altitudes since the contributions from transport and chemistry must be separated.

The Microwave Limb Sounder (MLS) aboard the Upper Atmosphere Research Satellite (UARS) has observed pockets of low ozone in the winter polar stratosphere outside the polar vortex. These pockets occur in the 6 to 10 millibar altitude range, where the effects of dynamics and chemistry on the ozone budget are comparable. The formation and evolution of these anomalies are investigated using a Lagrangian photochemical model, where the chemistry within an isolated parcel of air is simulated as it travels along a specified trajectory. Since we have decoupled the dynamics and chemistry, disagreement between the model and observations should reflect deficiencies in the chemistry.

We find that the model consistently overestimates the ozone loss rate above about 7 millibars, where the ozone deficit tends to manifest itself. Below 10 millibars altitude, the model is in good agreement with the observations, indicating that the description of chemistry is valid in the low to mid stratosphere. Individual trajectories have many uncertainties associated with them; in order to present more quantitative conclusions the results computed along many trajectories should be taken together to minimize errors.

1. Introduction

The vertical profile of ozone in the terrestrial stratosphere reflects the interaction between dynamics and chemistry. At altitudes above about 35 kilometers, or 6 millibars, ozone is in photochemical steady state. Models of this photochemically controlled region tend to underpredict the abundance of ozone relative to the observations (WMO 1985). This is known as the "ozone deficit" problem, and many studies have been undertaken examining this discrepancy (recent work includes Eluszkiewicz and Allen 1993, Siskind *et al.* 1995, and Crutzen *et al.* 1995).

Although most previous efforts concluded that there is a net loss of ozone in the photochemically controlled region above 6 millibars altitude, Crutzen *et al.* (1995) recently used observations from the Halogen Occultation Experiment (HALOE) aboard the Upper Atmosphere Research Satellite (UARS) to compute ozone loss rates and showed that there is actually a net production of ozone relative to the observations above about 2 millibars pressure. However, they note that HALOE ozone measurements are systematically somewhat lower than other correlative measurements; assimilation of low ozone measurements would reduce the magnitude of a model ozone deficit. They show that slightly increasing the ozone mixing ratio within the uncertainties of the measurements still leads to an ozone surplus above 2 millibars, but also leads to a net loss of ozone in the 3 to 10 millibar region.

Thus there still appears to be some chemical processes that are missing in current model descriptions. Several papers have called attention to the probability that the ClO/HCl ratio in the stratosphere is smaller than photochemical models seem to predict (e.g. Allen and Delitsky 1991, Stachnik *et al.* 1992). Jucks *et al.* (1995) recently used simultaneous measurements of active hydrogen, nitrogen, and chlorine radicals to show that there is no ozone deficit from 31 to 38 kilometers altitude (about 10 to 4 millibars) due to lower measurements of ClO compared to model calculations.

Michelson *et al.* (1995) also showed that photochemical models tend to underestimate the HCl/ClO ratio in the stratosphere.

At lower altitudes, transport is an important factor in determining the ozone concentration (Ko *et al.* 1989). Two-dimensional photochemical models are typically employed to properly account for the transport of ozone rich air from the tropics to the polar regions (e.g., Garcia and Solomon 1983). However, it is difficult to test the model chemistry in this region of the atmosphere due to the influence of transport. This is of importance since errors in the computed abundances may indicate that there are errors in the parameterization of transport in the models; the agreement between models and observations in this part of the atmosphere may simply be due to a fortuitous cancellation of errors.

Since the short term evolution of the ozone layer, particularly in the low to mid stratosphere, is a topic of considerable interest, establishing confidence in the description of chemical processes in the models is of high priority. One method to test the model chemistry in regions of the atmosphere where transport plays an important role is to employ a Lagrangian model (Austin *et al.* 1987), where the trajectory of a closed parcel of air (one that does not interact with surrounding air) is explicitly specified, and the net change in species abundances in the parcel is then solely due to chemistry. Recent measurements made by UARS of low ozone pockets in the winter polar stratosphere (Manney *et al.* 1995) provide an excellent opportunity to apply such a model.

During stratospheric warmings, the cyclonic polar vortex is often shifted off of the pole, and a strong, persistent anticyclone frequently forms. In the northern hemisphere, this is called the “Aleutian high”, as it often sits over the northern Pacific Ocean. Observations made by the Microwave Limb Sounder (MLS) instrument aboard UARS indicate that tongues of ozone rich air from low latitudes are drawn into the developing anticyclone. However, several days later, an area of low ozone, roughly 3 ppmv lower than typical mid-latitude extra-vortex values of 8 ppmv or so, forms near the center of the anticyclone. This bubble of low ozone is localized in the 6-10 millibar region, with higher ozone values at higher and lower pressures.

Examples of this occurrence were observed during December 1992, late February to early March 1993, and December 1993 in the northern hemisphere by MLS. Weaker events were observed during the 1993 and 1994 southern hemisphere winters. Three dimensional trajectory calculations, along with passive tracer data (UARS observations of H_2O, N_2O, and CH_4), indicate that air in these anomalies originated at lower latitudes and higher altitudes, where ozone abundances are $\sim$ 9 ppmv (Manney *et al.* 1995). Air inside the anomaly is typically isolated from outside air for a period of 1 to 3 weeks before the low ozone abundances appear.

Morris *et al.* (1995) recently investigated the February/March 1993 event with a Lagrangian photochemical model. They concluded that air in the low ozone anomalies is isolated at high latitudes for periods of time comparable to the photochemical lifetime of ozone. Since the odd oxygen production rate is low at high latitudes, the ozone abundance drops as it relaxes to the photochemical equilibrium value. Air outside the anomalies at similar latitudes meanders back and forth between mid and high latitudes over short timescales compared to the lifetime of odd oxygen. Thus the average odd oxygen production rate remains relatively high, and the ozone mixing ratio does not fall to low values. However, the ozone abundances computed by Morris *et al.* (1995) were consistently higher than the MLS observations. This ozone surplus was unexplained and may indicate a problem with their model, particularly in light of the ozone deficit issue.

We will use a Lagrangian photochemical model to calculate the ozone loss rates within parcels of air following trajectories at several altitudes leading to the

December 1992 and February/March 1993 low ozone pockets and compare them with the observed ozone loss rates. Discrepancies will highlight uncertainties in the adopted chemistry.

In this paper, measurements made by the MLS and the Cryogenic Limb Etalon Array Spectrometer (CLAES) instruments aboard UARS will be utilized to better define the species involved in the chemical destruction of ozone. The loss of ozone is dominated by several catalytic cycles:

$$\begin{array}{rr@{\;\longrightarrow\;}l}
 & O + HO_2 & O_2 + OH \\
 & OH + O_3 & HO_2 + O_2 \\ \hline
\text{net} & O + O_3 & 2\,O_2
\end{array}$$

$$\begin{array}{rr@{\;\longrightarrow\;}l}
 & O + NO_2 & O_2 + NO \\
 & NO + O_3 & NO_2 + O_2 \\ \hline
\text{net} & O + O_3 & 2\,O_2
\end{array}$$

$$\begin{array}{rr@{\;\longrightarrow\;}l}
 & O + ClO & O_2 + Cl \\
 & Cl + O_3 & ClO + O_2 \\ \hline
\text{net} & O + O_3 & 2\,O_2
\end{array}$$

along with a significant contribution from the Chapman reaction

$$O + O_3 \longrightarrow 2\,O_2.$$

The only important source of odd oxygen at these altitudes is the photolysis of molecular oxygen:

$$O_2 \longrightarrow 2\,O.$$

There are several good reviews of the detailed chemistry which controls ozone in the stratosphere, such as Johnston and Podolske (1978), Crutzen and Schmailzl (1983), and Brasseur and Solomon (1986).

The abundances of the active hydrogen, nitrogen, and chlorine radicals which participate in the catalytic cycles above may be constrained by either direct measurements or inferred from measurements of other species. Jackman *et al.* (1986)

incorporated O_3, H_2O, HNO_3, NO_2, and temperature data from the Limb Infrared Monitor of the Stratosphere (LIMS) to compute ozone production and loss rates. Froidevaux *et al.* (1989) also used LIMS observations of H_2O, NO_2, and temperature to constrain the abundances of HO_x and NO_x radicals in the calculations of the ozone profile above 6 millibars. Similar approaches have been taken using data from both LIMS and ATMOS (e.g., Natarajan *et al.* 1986, Callis *et al.* 1986, McElroy and Salawitch 1989, Allen and Delitsky 1991).

The abundance of odd hydrogen, or HO_x radicals, in the stratosphere is determined by simultaneous MLS measurements of water vapor and ozone. The active nitrogen and chlorine budgets are constrained by CLAES observations of HNO_3 and $ClONO_2$, along with estimates of total NO_y and Cl_y made from the observed abundances of tracer species such as N_2O or CH_4 from CLAES (see, for example, Fahey *et al.* 1990, Plumb and Ko 1992, and Woodbridge *et al.* 1994). The following section describes the spacecraft and the measurements.

2. UARS observations of trace species

The UARS spacecraft was deployed by the Space Shuttle Discovery on September 14, 1991 into a near-circular orbit at 585 km altitude and 57° inclination. Limb scanning instruments, such as MLS and CLAES, can observe to 80° latitude in one hemisphere and 34° in the other. The spacecraft is rotated through 180° in yaw approximately every 36 days, switching the hemisphere of highest latitude viewing. The orbiter is described in greater detail by Reber *et al.* (1993). The orbit is not sun-synchronous, but precesses through 360° approximately every 30 days, allowing measurements to be made at all local times for all covered latitudes over the course of a month. This rate of precession is slow enough that over the course of a day, each latitude has a specific (within twenty minutes) local solar time associated with the ascending track and another local time associated with the descending track. Thus, given the parcel latitude, the local times of observation may be deduced.

2.1 The Microwave Limb Sounder

The MLS instrument measures thermal emission in the microwave region of the spectrum at the atmospheric limb. A summary of the instrument is given by Barath *et al.* (1993). The Microwave Limb Sounder instrument has three radiometers which measure emission from the atmospheric limb at 63, 183, and 205 GHz. The 63 GHz radiometer provides information on pressure and temperature based on O_2 emission, the 183 GHz radiometer measures emission from H_2O and O_3, and the 205 GHz radiometer measures bands of ClO and O_3. At 1 to 10 millibar range, the 205 GHz retrievals have an estimated precision and accuracy of 0.2 to 0.3 ppmv, which is better than 10 percent at 1 millibar, and better than 5 percent at 10 millibars. The 183 GHz retrievals are less accurate due to the poorer characterization of the 183 GHz ozone band. We have employed maps made from the 205 GHz measurements for this work. Validation of the MLS ozone measurements is discussed more fully in Froidevaux *et al.* (1995).

The validity of the H_2O measurements is described in Lahoz *et al.* (1995). In the 1 to 10 millibar range of interest, the single profile precision is 0.1 to 0.2 ppmv (better than 4%) and the accuracy is 0.5 to 0.7 ppmv, or better than 10%.

Observations of chlorine monoxide (ClO) are also available from MLS (Waters *et al.* 1995). Unfortunately, the data are quite noisy; the typical single profile noise at the 1 σ level ranges from 0.4 ppbv at 10 millibars to 1.2 ppbv at 1 millbar. Typical model peak mixing ratios of ClO for the parcels of air we consider here are on the order of 0.4 ppbv or less. Given the large uncertainties in the ClO data and its short photochemical lifetime, we do not assimilate these observations but instead allow the model to compute ClO.

2.2 The Cryogenic Limb Array Etalon Spectrometer

CLAES also measures emission spectra at the atmospheric limb, and is further described by Roche *et al.* (1993). Validated data products from CLAES are CH_4, N_2O, HNO_3, and $ClONO_2$. The quality of CH_4 and N_2O measurements are discussed by Roche *et al.* (1995). In the 3 to 15 millibar range, CLAES CH_4 appears to be systematically 15 to 25 percent too high relative to correlative measurements. CLAES N_2O agrees to within 20 percent with correlative measurements, with no clear systematic bias as with CH_4. Random errors for each gas are on the order of 5 to 10 percent.

The validation of the HNO_3 measurements is described by Kumer *et al.* (1995). In the current version of the CLAES data (version 7), HNO_3 appears to be underestimated relative to correlative measurements by 15 to 25% at low mixing ratios (below 8 ppbv). The validation of $ClONO_2$ measurements is described in Mergenthaler *et al.* (1995). Although the uncertainties are on the order of 20% below 10 millibars altitude, above this level interference by other gases (chiefly O_3 and CO_2) becomes appreciable and the uncertainty approaches 100% at 6 millibars. Since the trajectories we are interested in here remain at higher pressures than 6 millibars for the most part, we have incorporated the observations of $ClONO_2$ into the model.

3. Lagrangian photochemical model

We have adapted the Caltech/JPL photochemical model to operate in a Lagrangian fashion, similar to the work of Austin *et al.* (1987), Jones *et al.* (1990), and Kawa *et al.* (1993). In this mode of calculation, the chemistry of an isolated air parcel with a specified trajectory is simulated, accounting for changes in temperature, pressure, radiation field, and other relevant physical parameters as warranted by the travel path. Since we have decoupled the chemistry and dynamics, the observed rate of ozone loss is solely due to photochemical processes. In this case, the continuity equation simply becomes

$$\frac{\partial n_i}{\partial t} = P_i - L_i$$

where n is the number density of species i, and P_i and L_i are the chemical production and loss terms, respectively, for species i. The dataset of reactions and photochemical cross sections is taken mostly from the 1994 JPL evaluation (DeMore *et al.* 1994).

Parcel positions (longitude, latitude, and pressure) are supplied by G. Manney (private communication, 1995) at noon GMT at each day over the period of the trajectory. Profiles of ozone at the parcel positions are generated for noon GMT from asynoptic maps, constructed as described by Elson and Froidevaux (1993). Temperature profiles at these times are also constructed from the UKMO data assimilation system.

The full model atmosphere consists of 40 levels from the surface to 0.316 mbar, which is the vertical range of the species profiles supplied by G. Manney. The level of the parcel is fixed to be level 20, and the continuity equation for each species is solved only at this level. The photochemical model time step is one hour except at twilight (within an hour of sunrise or sunset), where it is taken to be ten minutes. At the beginning of each time step, the position of the parcel (longitude, latitude, log pressure) is found by linear interpolation between the positions in the trajectory code output. The local solar time of the parcel is also updated to account for motion in longitude. Updated ozone and temperature profiles are also constructed by linear interpolation. The ozone concentration is otherwise not allowed to vary. The vertical structure of the atmosphere is recalculated at each time step from the assumption of hydrostatic equilibrium, to account for vertical motion of the parcel. Mixing ratios of all species at each level are assumed to be conserved as the density changes.

We will compare the computed changes in ozone with the observed changes. The net production rate of odd oxygen per day is computed by summing the rates of all reactions in the model which either produce or destroy odd oxygen (defined as the sum of O, $O(^1D)$, and O_3), as listed in Table I. ΔO_x is the net change in odd oxygen per reaction (Johnston and Podolske 1978, Allen *et al.* 1984).

The chemical composition of the parcel is initialized to be consistent with UARS observations. The total NO_y and Cl_y budgets are initialized according to the N_2O relations (Figures 6 and 7) in Plumb and Ko (1992). We assume that the parcel is in photochemical equilibrium for the initial latitude in the trajectory file. In order to determine the partitioning between members of the active nitrogen and chlorine families at the start of the run, all of the NO_y and Cl_y is assumed initially to be in the form of HNO_3 and HCl, respectively. The abundances of O_2, N_2, and O_3 are fixed to their initial values. All other species concentrations are computed self-consistently. The parcel is held at the latitude, pressure, and season at which it originated for three weeks of model time, long enough for the partitioning between members in the active nitrogen and chlorine families to reach a diurnally varying photochemical equilibrium.

4. Data assimilation

Observations of trace gases (O_3, H_2O, N_2O, HNO_3, CH_4, and $ClONO_2$) made by UARS instruments over the period of interest have been assimilated into the photochemical model. Using the proper ozone profile is important since models of the terrestrial stratosphere generally underpredict ozone abundances in the photochemically controlled region above 35 km altitude (Eluszkiewicz and Allen 1993). Below this altitude it is unclear whether the current description of photochemical parameters

Table I. Important reactions for the odd oxygen balance.

	Reaction			Rate Coefficient*	ΔO_x
R1	$O_2 + h\nu$	$\longrightarrow$	$2\,O$		+2
R2	$O_2 + h\nu$	$\longrightarrow$	$O + O(^1D)$		+2
R5	$HO_2 + h\nu$	$\longrightarrow$	$OH + O$		+1
R8	$H_2O + h\nu$	$\longrightarrow$	$2\,H + O$		+1
R10	$NO + h\nu$	$\longrightarrow$	$N + O$		+1
R11	$NO_2 + h\nu$	$\longrightarrow$	$NO + O$		+1
R12	$NO_3 + h\nu$	$\longrightarrow$	$NO_2 + O$		+1
R16	$N_2O_5 + h\nu$	$\longrightarrow$	$NO + NO_3 + O$		+1
R24	$ClO + h\nu$	$\longrightarrow$	$Cl + O$		+1
R25	$ClOO + h\nu$	$\longrightarrow$	$ClO + O$		+1
R26	$OClO + h\nu$	$\longrightarrow$	$ClO + O$		+1
R36	$ClNO_3 + h\nu$	$\longrightarrow$	$O + ClONO$		+1
R83	$CO_2 + h\nu$	$\longrightarrow$	$CO + O$		+1
R95	$2\,O + M$	$\longrightarrow$	$O_2 + M$	$4.3 \times 10^{-28}\ T^{-2.0}$	−2
R99	$O + O_3$	$\longrightarrow$	$2\,O_2$	$8.0 \times 10^{-12}\ e^{-2060/T}$	−2
R102	$O(^1D) + O_3$	$\longrightarrow$	$2\,O_2$	1.2×10^{-10}	−2
R104	$O + H_2$	$\longrightarrow$	$OH + H$	$8.5 \times 10^{-20}\ e^{-3160/T}$	−1
R105	$O + OH$	$\longrightarrow$	$O_2 + H$	$2.2 \times 10^{-11}\ e^{120/T}$	−1
R106	$O + HO_2$	$\longrightarrow$	$OH + O_2$	$3.0 \times 10^{-11}\ e^{200/T}$	−1
R107	$O + H_2O_2$	$\longrightarrow$	$OH + HO_2$	$1.4 \times 10^{-12}\ e^{-2000/T}$	−1
R108	$O(^1D) + H_2$	$\longrightarrow$	$H + OH$	1.0×10^{-10}	−1
R109	$O(^1D) + H_2O$	$\longrightarrow$	$2\,OH$	2.2×10^{-10}	−1
R112	$H + O_3$	$\longrightarrow$	$OH + O_2$	$1.4 \times 10^{-10}\ e^{-470/T}$	−1
R115	$H + HO_2$	$\longrightarrow$	$H_2O + O$	1.6×10^{-12}	+1
R116	$2\,OH$	$\longrightarrow$	$H_2O + O$	$4.2 \times 10^{-12}\ e^{-240/T}$	+1
R118	$OH + O_3$	$\longrightarrow$	$HO_2 + O_2$	$1.6 \times 10^{-12}\ e^{-940/T}$	−1
R122	$HO_2 + O_3$	$\longrightarrow$	$OH + 2\,O_2$	$1.1 \times 10^{-14}\ e^{-500/T}$	−1
R125	$O + NO_2$	$\longrightarrow$	$NO + O_2$	$6.5 \times 10^{-12}\ e^{120/T}$	−1
R126	$O + NO_2 + M$	$\longrightarrow$	$NO_3 + M$	$8.1 \times 10^{-27}\ T^{-2.0}$	−1
R127	$O + HNO_3$	$\longrightarrow$	$OH + NO_3$	3.0×10^{-17}	−1
R128	$O + HO_2NO_2$	$\longrightarrow$	$OH + NO_2 + O_2$	$7.8 \times 10^{-11}\ e^{-3400/T}$	−1
R129	$O + N_2O_5$	$\longrightarrow$	$2\,NO_2 + O_2$	3.0×10^{-16}	−1
R130	$O(^1D) + N_2 + M$	$\longrightarrow$	$N_2O + M$	$1.1 \times 10^{-35}\ T^{-0.6}$	−1
R131	$O(^1D) + N_2O$	$\longrightarrow$	$2\,NO$	6.7×10^{-11}	−1
R132	$O(^1D) + N_2O$	$\longrightarrow$	$N_2 + O_2$	4.9×10^{-11}	−1
R133	$O_3 + CH_3ONO$	$\longrightarrow$	$CH_3ONO_2 + O_2$	$6.8 \times 10^{-13}\ e^{-5315/T}$	−1
R143	$N + O_2$	$\longrightarrow$	$NO + O$	$1.5 \times 10^{-11}\ e^{-3600/T}$	+1
R144	$N + O_3$	$\longrightarrow$	$NO + O_2$	2.0×10^{-16}	−1
R147	$N + NO$	$\longrightarrow$	$N_2 + O$	$2.1 \times 10^{-11}\ e^{100/T}$	+1
R148	$N + NO_2$	$\longrightarrow$	$N_2O + O$	$5.8 \times 10^{-12}\ e^{220/T}$	+1
R149	$NO + O + M$	$\longrightarrow$	$NO_2 + M$	$4.7 \times 10^{-28}\ T^{-1.5}$	−1
R150	$NO + O_3$	$\longrightarrow$	$NO_2 + O_2$	$2.0 \times 10^{-12}\ e^{-1400/T}$	−1
R158	$NO_2 + O_3$	$\longrightarrow$	$NO_3 + O_2$	$1.2 \times 10^{-13}\ e^{-2450/T}$	−1
R166	$NO_3 + O$	$\longrightarrow$	$O_2 + NO_2$	1.0×10^{-11}	−1
R193	$O + OClO$	$\longrightarrow$	$ClO + O_2$	$2.4 \times 10^{-12}\ e^{-960/T}$	−1
R194	$O + OClO + M$	$\longrightarrow$	$ClO_3 + M$	$1.0 \times 10^{-28}\ T^{-1.1}$	−1
R195	$O + Cl_2O$	$\longrightarrow$	$2\,ClO$	$2.7 \times 10^{-11}\ e^{-530/T}$	−1

TABLE I — *Continued*

	Reaction	Rate Coefficient*	ΔO_x
R196	$\mathrm{O + ClNO_3 \longrightarrow O_2 + ClONO}$	$2.9 \times 10^{-12}\ e^{-800/T}$	-1
R197	$\mathrm{O + HCl \longrightarrow OH + Cl}$	$1.0 \times 10^{-11}\ e^{-3300/T}$	-1
R198	$\mathrm{O + HOCl \longrightarrow OH + ClO}$	$1.0 \times 10^{-11}\ e^{-1300/T}$	-1
R199	$\mathrm{O(^1D) + Cl_2 \longrightarrow Cl + ClO}$	2.1×10^{-10}	-1
R200	$\mathrm{O(^1D) + HCl \longrightarrow Cl + OH}$	1.0×10^{-10}	-1
R201	$\mathrm{O(^1D) + HCl \longrightarrow ClO + H}$	3.6×10^{-11}	-1
R202	$\mathrm{O(^1D) + CHFCl_2 \longrightarrow CFCl_2 + OH}$	1.9×10^{-10}	-1
R203	$\mathrm{O(^1D) + CHF_2Cl \longrightarrow CF_2Cl + OH}$	7.2×10^{-11}	-1
R204	$\mathrm{O(^1D) + CCl_4 \longrightarrow CCl_3 + ClO}$	2.8×10^{-10}	-1
R205	$\mathrm{O(^1D) + CFCl_3 \longrightarrow CFCl_2 + ClO}$	1.4×10^{-10}	-1
R206	$\mathrm{O(^1D) + CF_2Cl_2 \longrightarrow CF_2Cl + ClO}$	1.2×10^{-10}	-1
R207	$\mathrm{O(^1D) + CF_3Cl \longrightarrow CF_3 + ClO}$	6.0×10^{-11}	-1
R217	$\mathrm{O(^1D) + CF_3CFCl_2 \longrightarrow Cl + 4\,F + ClO}$	1.0×10^{-10}	-1
R219	$\mathrm{O(^1D) + COCl_2 \longrightarrow 2\,ClO + CO}$	3.6×10^{-10}	-1
R220	$\mathrm{O(^1D) + COFCl \longrightarrow ClO + FCO}$	1.9×10^{-10}	-1
R259	$\mathrm{Cl + O_3 \longrightarrow ClO + O_2}$	$2.9 \times 10^{-11}\ e^{-260/T}$	-1
R313	$\mathrm{ClO + O \longrightarrow Cl + O_2}$	$3.0 \times 10^{-11}\ e^{70/T}$	-1
R315	$\mathrm{ClO + O_3 \longrightarrow OClO + O_2}$	$1.0 \times 10^{-12}\ e^{-4000/T}$	-1
R316	$\mathrm{ClO + O_3 \longrightarrow ClOO + O_2}$	1.4×10^{-17}	-1
R331	$\mathrm{OClO + O_3 \longrightarrow ClO + 2\,O_2}$	$2.1 \times 10^{-12}\ e^{-4700/T}$	-1
R353	$\mathrm{O + ClCO \longrightarrow Cl + CO_2}$	3.0×10^{-11}	-1
R358	$\mathrm{O + ClCO_3 \longrightarrow Cl + O_2 + CO_2}$	1.0×10^{-11}	-1
R491	$\mathrm{O + CH_4 \longrightarrow CH_3 + OH}$	$1.1 \times 10^{-15}\ e^{-4270/T}$	-1
R494	$\mathrm{O + H_2CO \longrightarrow OH + HCO}$	$3.4 \times 10^{-11}\ e^{-1600/T}$	-1
R496	$\mathrm{O(^1D) + CH_4 \longrightarrow CH_3 + OH}$	1.1×10^{-10}	-1
R497	$\mathrm{O(^1D) + CH_4 \longrightarrow CH_3O + H}$	3.0×10^{-11}	-1
R498	$\mathrm{O(^1D) + CH_4 \longrightarrow H_2CO + H_2}$	7.5×10^{-12}	-1
R532	$\mathrm{CH_3 + O \longrightarrow H_2CO + H}$	1.1×10^{-10}	-1
R535	$\mathrm{CH_3 + O_3 \longrightarrow CH_3O + O_2}$	$5.4 \times 10^{-12}\ e^{-220/T}$	-1

*Units are $\mathrm{cm^3\ s^{-1}}$ for two-body reactions and $\mathrm{cm^6\ s^{-1}}$ for three-body reactions.

is valid. The chemical destruction rate of ozone is itself dependent upon the ozone concentration. Thus in order to compute the loss rate without introducing potential errors related to the ozone deficit problem, the observed ozone concentration in the parcel should be used. A second order effect is the sensitivity of the radiation field to the ozone profile, which impacts the abundances of active radical species.

Other species observed by UARS are also assimilated into the model. Although assimilating H_2O, N_2O, and CH_4 should not have much of an impact as they are inert tracers, updating HNO_3 and $ClONO_2$ might be important as they will affect the partitioning of the NO_y and Cl_y families.

For long-lived species (H_2O, N_2O, HNO_3, and CH_4), the concentrations in the parcel are updated at each time step in the same manner as the ozone abundance. Concentrations are found by linear interpolation in time between concentrations taken from maps made for noon GMT for each day over the period of the trajectory. The long lived species are not otherwise allowed to vary. Short lived species which have significant diurnal variations (in this case $ClONO_2$) must be treated differently, as described below.

Due to the nature of the UARS orbit, any given latitude that UARS passes over is observed at two local times per day: once during the ascending track, and once during the descending track. Two $ClONO_2$ concentration maps are produced for each day over the time period of the trajectory; one is made using only ascending track observations, and one is made from only descending track observations. Each latitude on each map thus has one specific local time associated with it. Mixing ratios of $ClONO_2$ at the parcel location are assimilated into the model twice per day at the local times corresponding to the parcel latitude; at one local time the observation is read off of the map made using only ascending track observations, at the other the observation is read from the map made from descending track observations.

We update HNO_3 at every time step as discussed above. However, modifying the HNO_3 abundance will affect the partitioning of the other NO_y species (NO, NO_2, and N_2O_5) if the total amount of active nitrogen is to be conserved. Over most of the day, we allow the model to compute the abundances of these short lived species using the standard chemistry. The HNO_3 concentration varies slowly enough that the total NO_y abundance does not change appreciably over a day. Then once per day, we update the partitioning of the short lived species to keep the NO_y abundance fixed to its initial value. In order to do this, we make two assumptions. The first is that NO is in photochemical steady state such that the NO/NO_2 ratio is given by

$$\frac{[\mathrm{NO}]}{[\mathrm{NO_2}]} = \frac{J_1}{k_1\,[\mathrm{O_3}] + k_2\,[\mathrm{ClO}]},$$

where k_1 is the rate coefficient for the reaction of NO and O_3, and k_2 is the rate coefficient for the reaction of NO and ClO (similar expressions have been used by Brasseur and Solomon 1986, Natarajan *et al.* 1986, Callis *et al.* 1986, and Froidevaux *et al.* 1989). The second is that the NO_2/N_2O_5 ratio remains constant before and after they are updated. By updating the NO_y family in this manner, we only disturb the diurnal variation of the short lived species once per day.

For Cl_y, we update $ClONO_2$ twice per day according to CLAES observations as described above. At the same time, we update the HCl and ClO concentrations by holding the ClO/HCl ratio constant. Then assuming that Cl_y = HCl + ClO + $ClONO_2$ = constant, we solve for the abundances of HCl and ClO.

5. The February/March 1993 event

Figure 1 shows two vertical profiles of ozone taken from an asynoptic map generated from MLS observations for noon GMT, March 7, 1993. The dashed line is inside the low ozone pocket at 254.5° east longitude and 71° north latitude. The solid line shows the vertical profile of ozone outside the anomaly at 174.5° east longitude and 71° north latitude. Note that the ozone peak in the anomaly is lower and sharper than for the ozone peak outside the anomaly and that the ozone in the anomaly is considerably depleted relative to the ozone outside from about 1-10 millibars.

Figure 2 shows maps of ozone, water, nitrous oxide, and methane at the 840 K level on March 7, 1993. The low ozone anomaly is centered over northern Canada at approximately 110° west longitude and 65° north latitude. Although the ozone

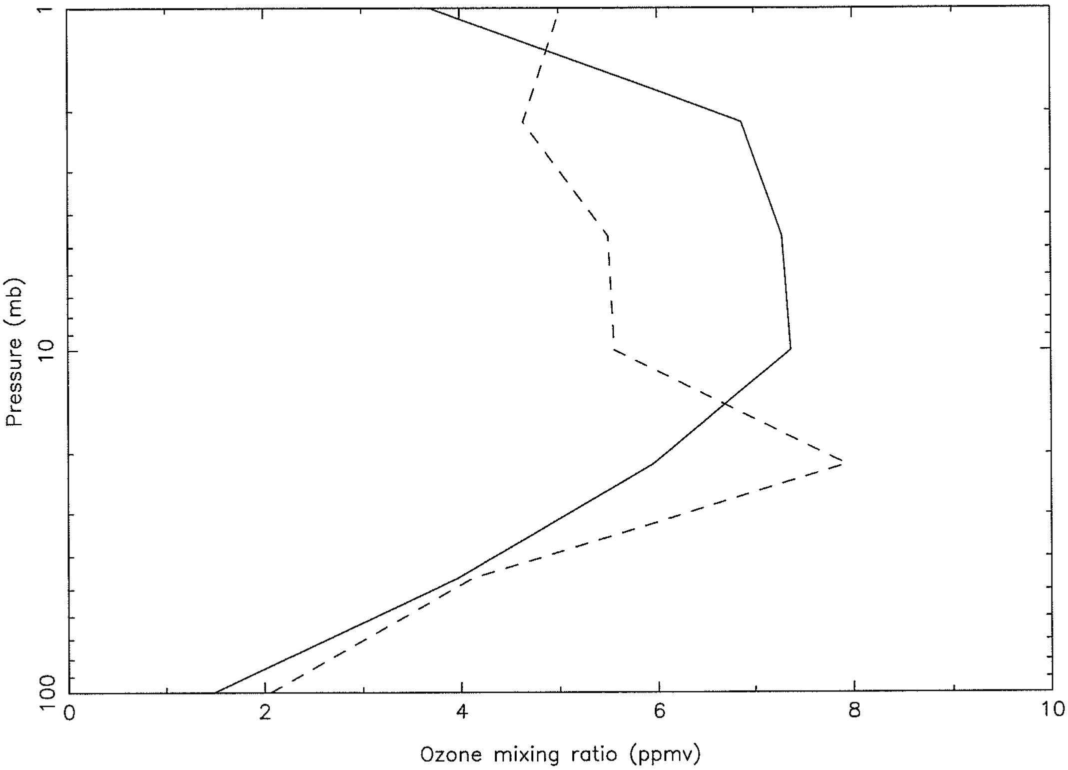

Figure 1. Ozone profiles inside (dashed line) and outside the anomaly (solid line) on March 7, 1993. Both profiles are at 71° north latitude.

abundance in the anomaly is comparable to ozone abundances in the polar vortex (located over northern Europe), note that the abundances of the tracer species H_2O, N_2O, and CH_4 are comparable to their tropical values and are quite different from the abundances observed in the polar vortex.

We have computed the chemical evolution of parcels along several different trajectories ending at the 740, 840, and 960 K potential temperature levels at the position of the anomaly (corresponding to 14.7, 10.4, and 7.1 millibars, respectively, on March 7), and also at the 840 K level outside the anomaly (11.6 millibars) at the same latitude. We will compare the magnitudes and trends of the observed and modeled ozone loss rates in parcels leading to the low ozone anomaly as well as for

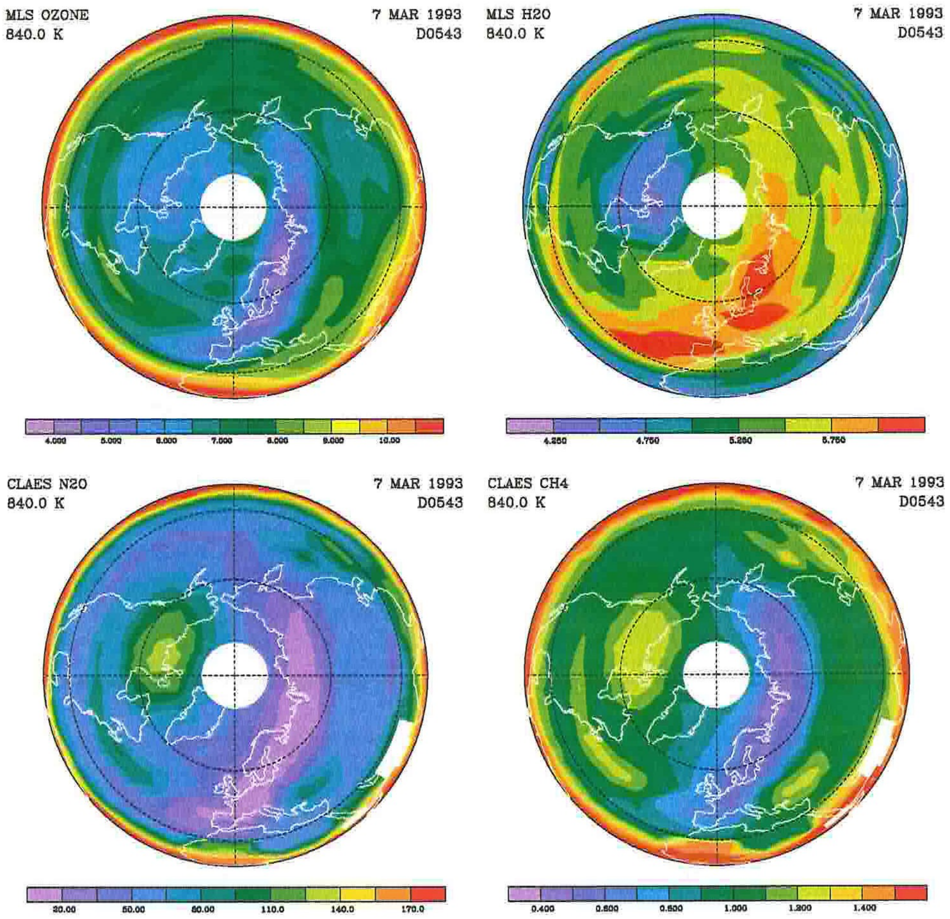

Figure 2. Maps of ozone, water, nitrous oxide, and methane on March 7, 1993 at the 840 K potential temperature level. Units on contours are ppmv except for N_2O, which is in ppbv.

parcels with trajectories ending outside the low ozone bubble, where the ozone has "normal" values with the observed changes in ozone along the computed trajectories.

Trajectories for two groups of 3200 parcels were provided by G. Manney (private communication, 1995). The trajectory model was run backwards in time for 22 days, starting at 12 noon GMT on March 7, 1993, and ending on February 14, 1993. The first group of trajectories was initialized on the 740, 840, and 960 K isentropic surfaces on a 0.5 by 0.5 degree latitude longitude grid, running from 230 to 279.5 degrees east longitude and 56 to 71.5 degrees north latitude. A second run for air outside the anomaly, with ozone values more representative of the zonal mean, was made for the same dates and latitude range, but from 150 to 199.5 east longitudes. More specific details regarding the trajectories computed for this event are given in Manney *et al.* (1995).

We shall consider one particular set of trajectories in detail below and summarize the calculation of ozone losses for the others. Figure 3 shows the calculated trajectories for three parcels ending inside the anomaly at 254.5 degrees east longitude, 71 degrees north latitude at the 740 K, 840 K, and 960 K potential temperature levels, and one parcel ending outside the anomaly at 174.5 degrees east longitude and 71 degrees north latitude at the 840 K level.

Uncertainties in the trajectory model are difficult to quantify. These errors manifest themselves not only by affecting the physical conditions of the parcel (solar zenith angle, pressure, temperature) but also in the initialization and assimilation of spatially variable species. As an estimate of the cumulative uncertainty in parcel position on February 14, 1993, which is the end of the back calculation started on March 7, 1993, we take the uncertainty in longitude to be 5 degrees, 2.5 degrees in latitude, and 30 K in potential temperature. We will employ this "uncertainty box" to estimate the errors in mixing ratios of ozone and other species along the trajectory.

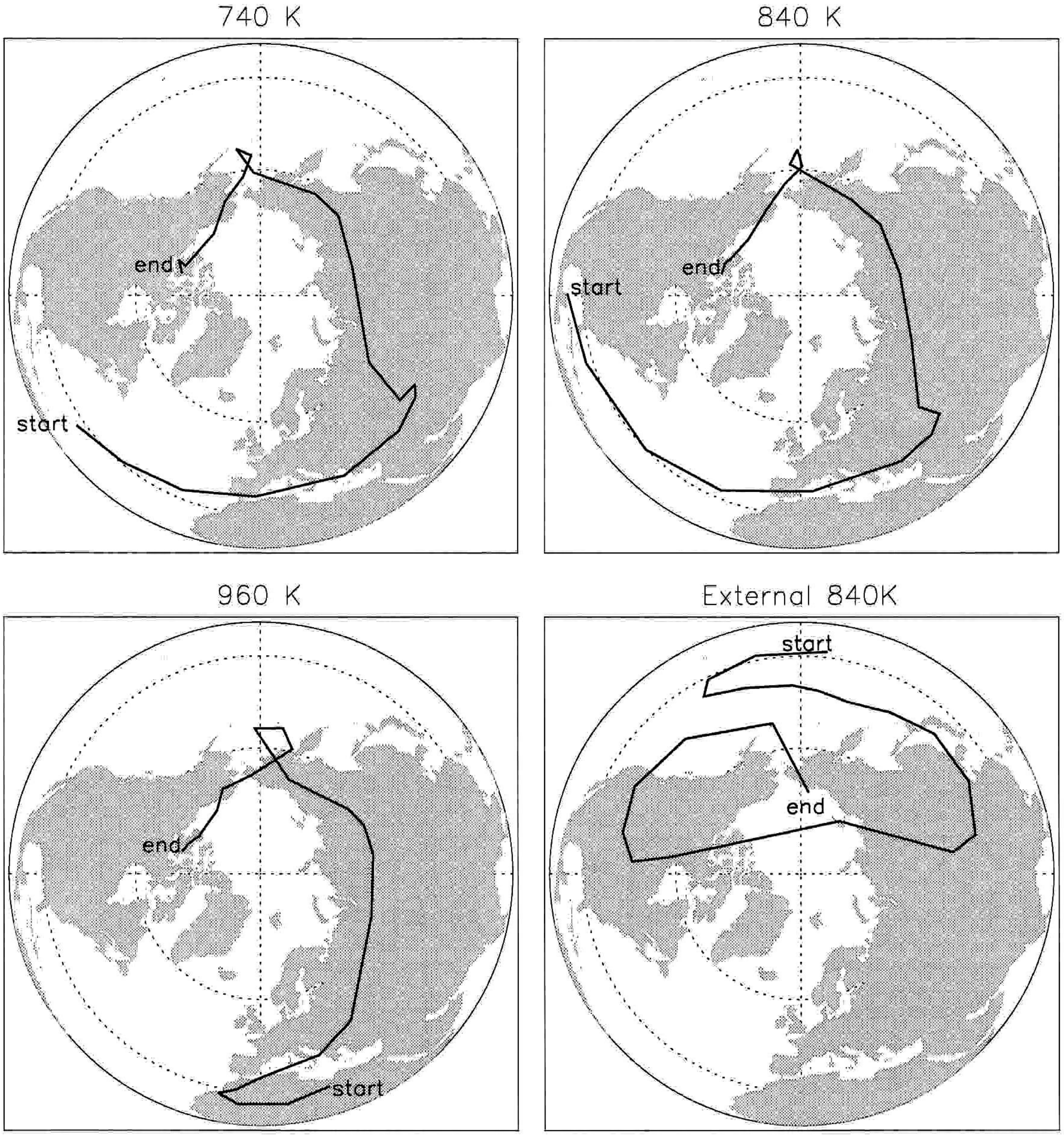

Figure 3. Four sample trajectories for the February/March 1993 event. Parcels begin on February 14, 1993 and end on March 7, 1993.

One measure of the validity of the trajectory calculations is the degree of variability in long lived tracer species. Figure 4 shows the abundances of O_3, CH_4, N_2O, and H_2O along the parcel trajectory as a function of time. The error bar for each point is calculated from both the UARS measurement uncertainty along with the spatial variability of the gas within the uncertainty box. This is a conservative

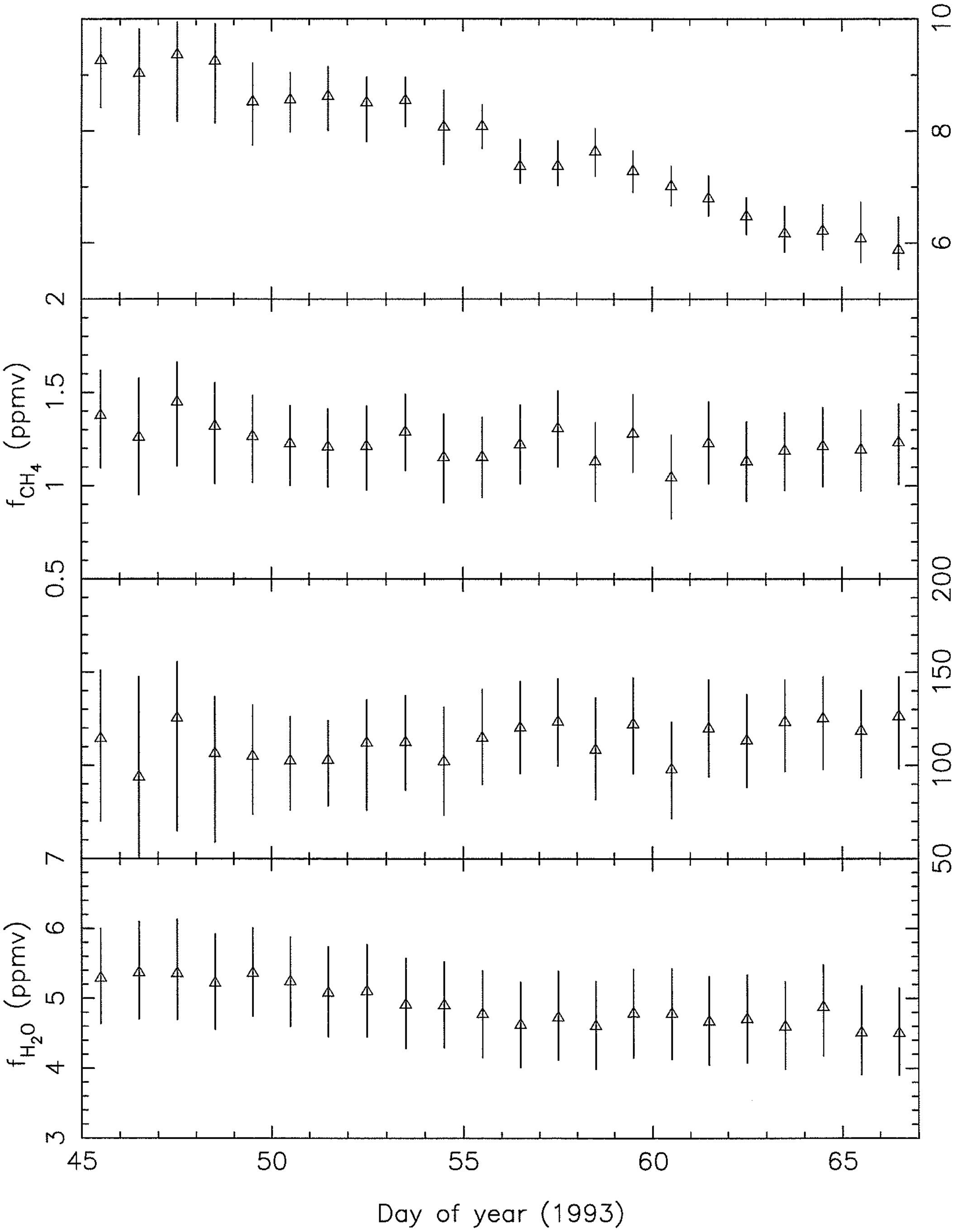

Figure 4. Trends in O_3 and the long lived tracer species CH_4, N_2O, and H_2O along the trajectory.

approach since the size of the error box was estimated for the last point of the back trajectory, which is where the uncertainty in position is largest. The ozone mixing ratio decreases by 37% over the period of the trajectory while none of the tracers show such a comparable change, although there is a decreasing trend on the order of 10% in the H_2O mixing ratio between days 50 and 55. This may be indicative of some uncertainty in the trajectory before day 55. We will return to this point shortly.

To initialize the NO_y and Cl_y partitioning, the latitude, pressure, and solar longitude are fixed to their values at noon GMT February 14, 1993 for each trajectory. The mean N_2O mixing ratio in the parcel over the trajectory is approximately 120 ppbv. From the relations given in Plumb and Ko (1992), we have initialized the parcel with 15 ppbv NO_y and 2.5 ppbv Cl_y. The mixing ratios of O_2, N_2, and O_3 are fixed to their initial values (20.9%, 78.1%, and 9.3 ppmv, respectively). All other species are computed self-consistently for three weeks of model time such that the members of the NO_y and Cl_y families converge to a diurnally varying photochemical steady state, as shown in Figure 5 for the 840 K anomalous parcel, which is held at 21.9° north and 6.8 millibars.

Figure 6a shows the observed ozone abundance along the 840 K trajectory leading to the anomaly. The ozone values have been smoothed by replacing each point with the average of the point and its two neighbors, keeping the endpoints unchanged. This makes it easier to see trends in the day-to-day change in the measured ozone. The second panel compares the day-to-day change in the smoothed ozone with the model predictions for change in ozone over the period of the trajectory. We estimate the uncertainty on the observed day-to-day change in the ozone mixing ratio to be on the order of 0.4 ppmv; since the precision of the MLS ozone measurements is on the order of 0.2 ppmv, the uncertainty in the difference between uncorrelated measurements should be somewhat more than twice this. Note that this uncertainty is in most

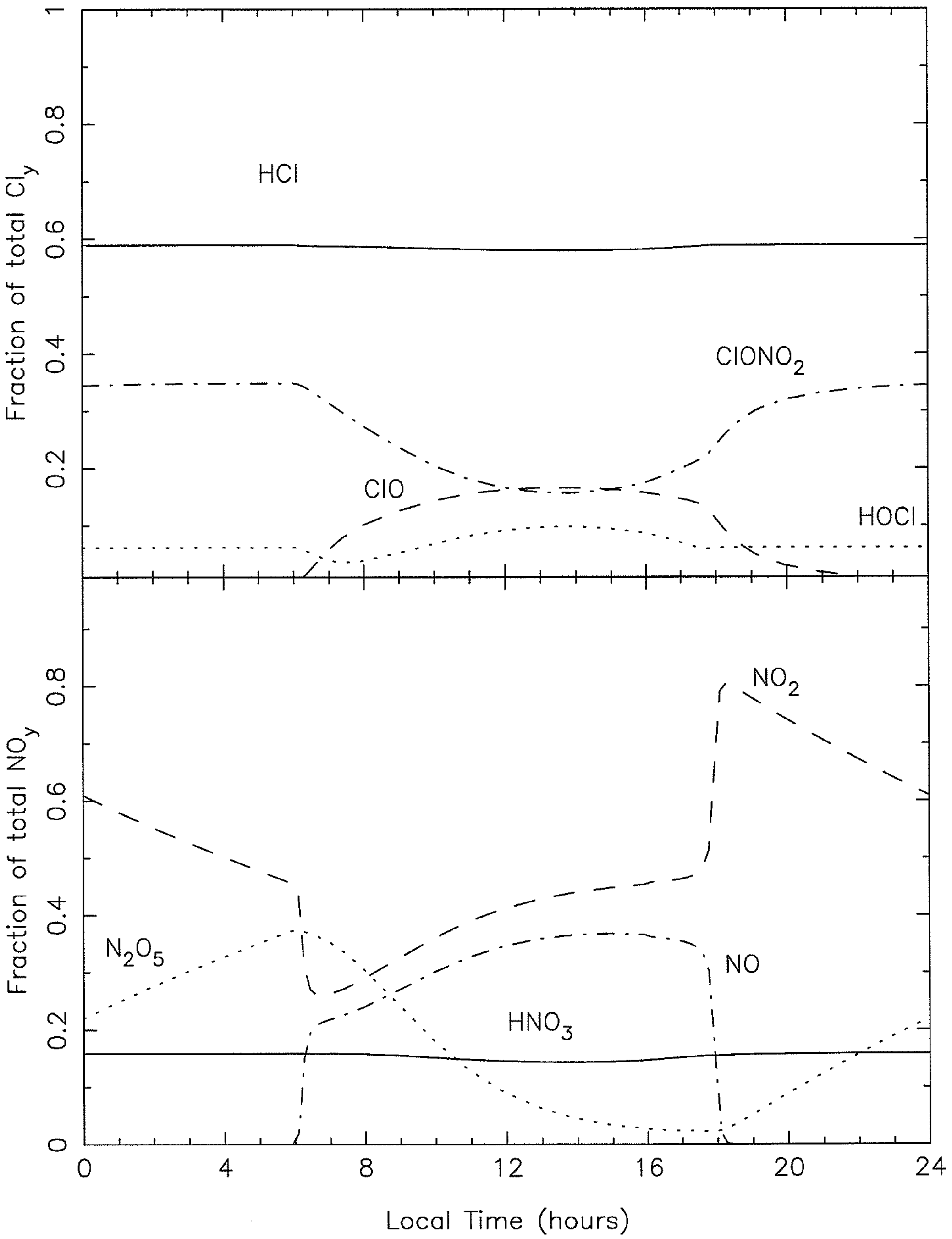

Figure 5. Equilibrium partitioning of the NO_y and Cl_y families at the initial latitude and pressure of the parcel leading to the February/March 1993 anomaly.

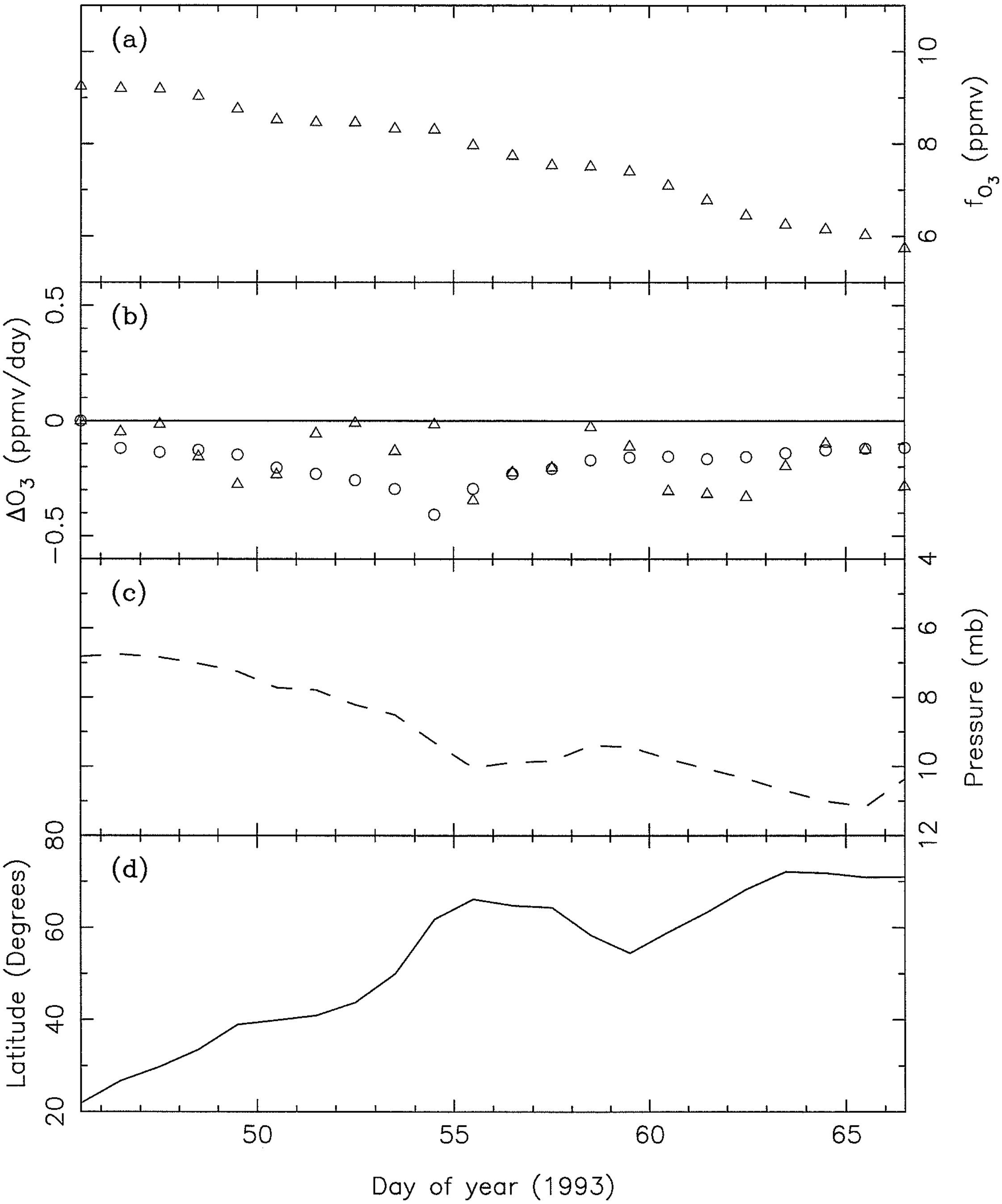

Figure 6. Calculated ozone loss for 840 K anomalous parcel. The observed loss is 3.51 ± 0.84 ppmv and the model loss is 3.97 ppmv. (a) Ozone mixing ratio as observed by MLS. (b) Observed change in ozone (triangles) and model calculation (circles). (c) Pressure and (d) latitude of the parcel as a function of time.

cases larger than the magnitude of the day-to-day change! Nonetheless, there is an obvious long term trend in the observations, and both the observed and model ozone changes are systematically negative and of roughly the same magnitude, with the notable exception of days 50 through 55, where the model ozone loss is greater than the observed loss. Recall that the water mixing ratio showed a decreasing trend over this time; this may be an indication that the trajectory was somewhat inaccurate. The observed overall decrease in ozone is 3.51 ppmv with an estimated uncertainty of 0.84 ppmv. The integrated model loss is 3.97 ppmv. The third and fourth panels show the pressure and latitude histories of the parcel, respectively.

Figure 7 is a similar plot for the trajectory leading to the point outside the anomaly. The ozone mixing ratio remains relatively constant over this time period, although a gentle oscillation with a period of about a week can be seen. The observed change in ozone is a slight decrease of 0.05 ± 0.78 ppmv, while the model predicts a slight increase of 0.03 ppmv. Looking at the day-to-day changes in ozone, we see that there is quite good agreement between the model and observations over the last ~ 10 days of the trajectory. Over the first part of the trajectory, the observed changes are much larger in magnitude than the model predictions. The trajectory calculation is probably valid since the mixing ratios of tracer species are fairly constant. Although the disagreement between model and observation is within the 0.4 ppmv error bar, the observed day-to-day changes seem to be a real feature. The discrepancy may be due to an error in the initialization of NO_y and Cl_y partitioning in the parcel. Recall that the initialization was determined based on the assumption that the parcel is in photochemical equilibrium for the initial latitude. It is possible that this particular parcel was not held at the original latitude long enough to come to steady state.

Figure 8 shows the model results at the 740 K potential temperature level within the anomaly. Note the large drop in the observed ozone over the first few days

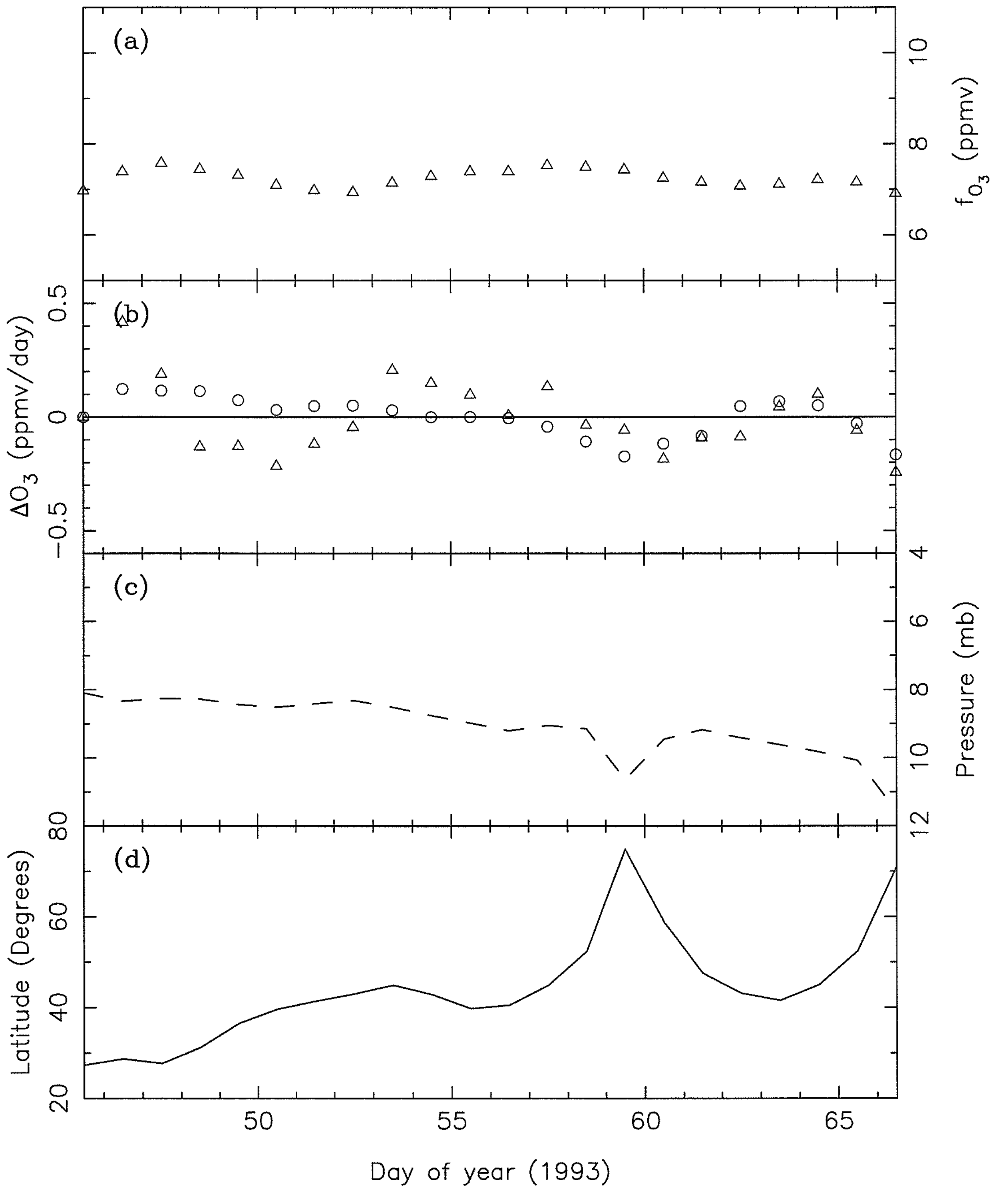

Figure 7. As Figure 6, but for the parcel ending outside the anomaly at 840 K. The observed change in ozone is -0.05 ± 0.78 ppmv and the model change is 0.03 ppmv.

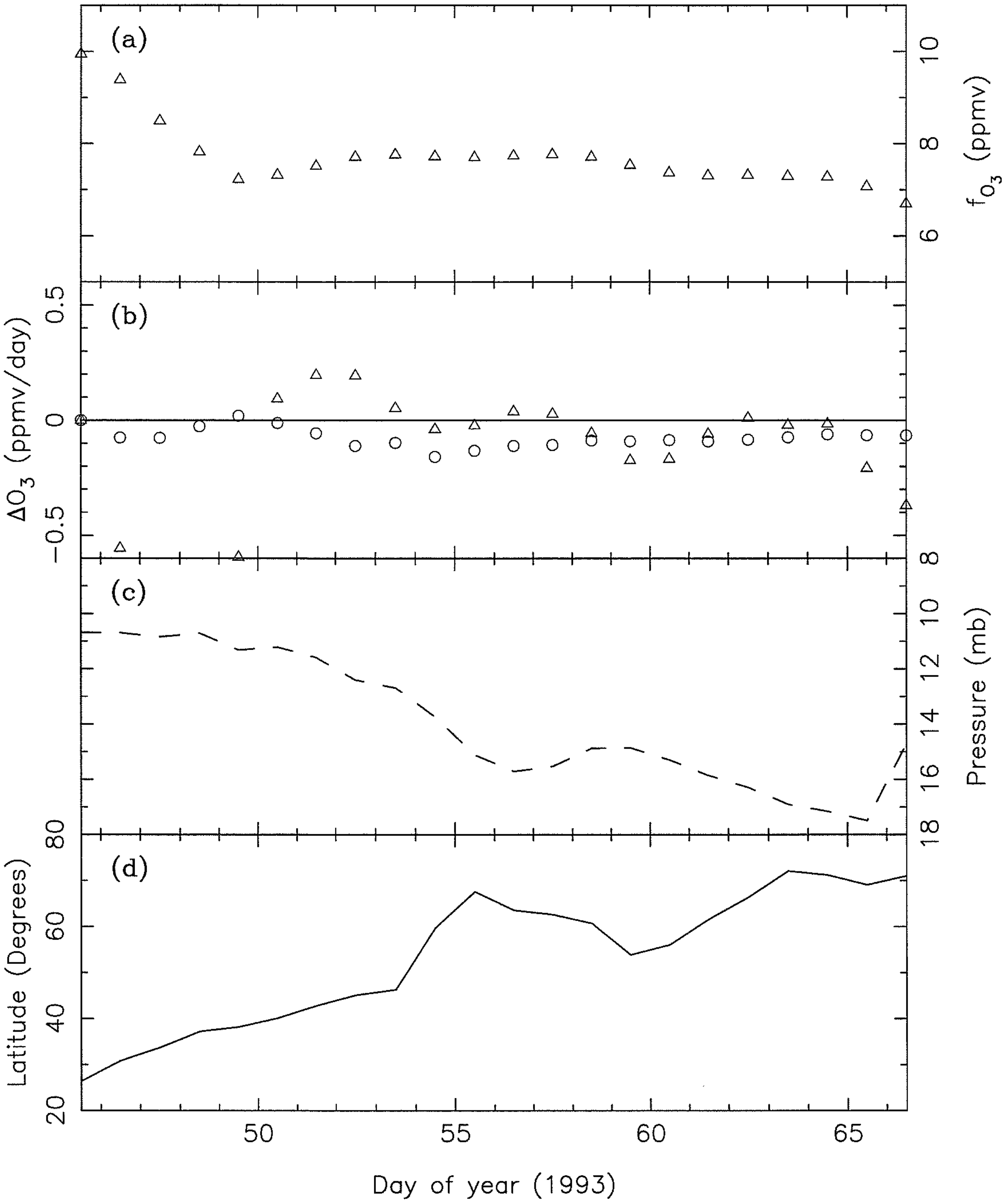

Figure 8. As Figure 6, but for the parcel ending at 740 K within the anomaly. The observed change in ozone is 3.24 ± 1.53 ppmv and the model change is -1.65 ppmv.

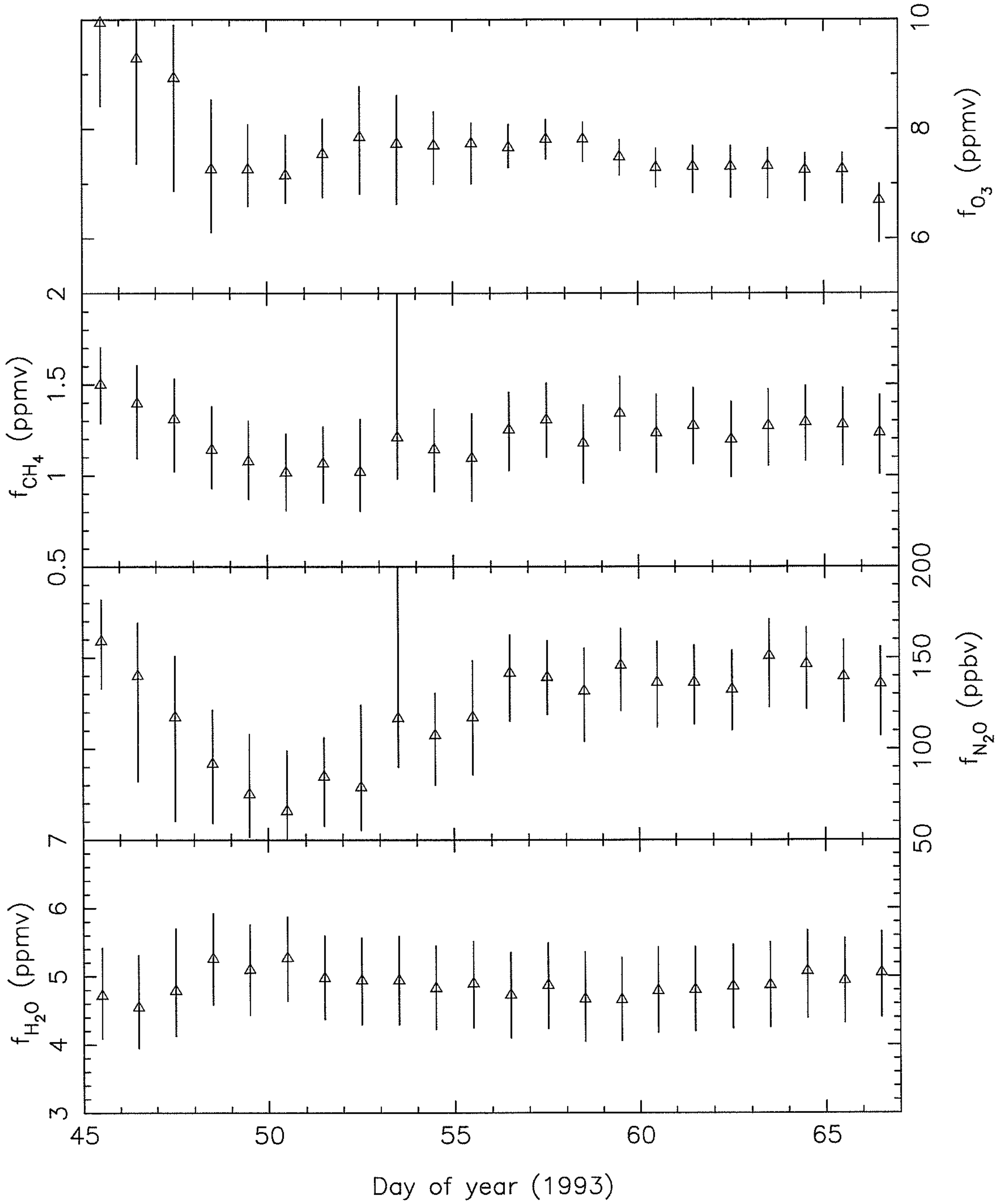

Figure 09. As Figure 4, but for the parcel ending at 740 K within the anomaly.

of the trajectory. This leads us to suspect that the trajectory may be in error for this time period. Looking at the evolution of the long lived tracers for this parcel (Figure 9), we note considerable variability over the first ten days of the trajectory. Thus this particular trajectory probably does not describe the true motion of this parcel, at least before day 55. Over the last ten days or so, the model is in better agreement up to the last day. However, it must still be noted that both the model and observed changes in ozone are small ($\sim$ 0.1 ppmv) compared to the uncertainty on the model day-to-day change (0.4 ppmv). If we ignore the first ten days of the trajectory, the observed change in ozone is -1.0 ppmv and the model prediction is -0.92 ppmv. This agreement is somewhat misleading, since half of the observed decrease occurs on the last day, while the model day-to-day decreases are relatively consistent with one another.

Finally, Figure 10 summarizes the history of the parcel ending within the anomaly at the 960 K potential temperature level. Note in the second panel that the model ozone losses are consistently much greater than the observations would indicate. In fact, the integrated model loss of ozone is 12 ppmv, greater than the initial abundance! This unphysical result occurs because the computed loss rates are based upon the observed ozone mixing ratio, which is independent of the model calculations. However, the model predictions for the day-to-day changes come into much better agreement near the end of the trajectory, as the parcel descends to around 7 millibars. This is interesting because the ozone deficit generally manifests itself in photochemical models at altitudes above about 6 millibars. This parcel appears to move from an altitude where there is an ozone deficit to one where there is not, and this is reflected in the second panel.

The results we have presented thus far do show a qualitatively interesting point, namely that the ozone deficit issue still appears to exist above about 7 mil-

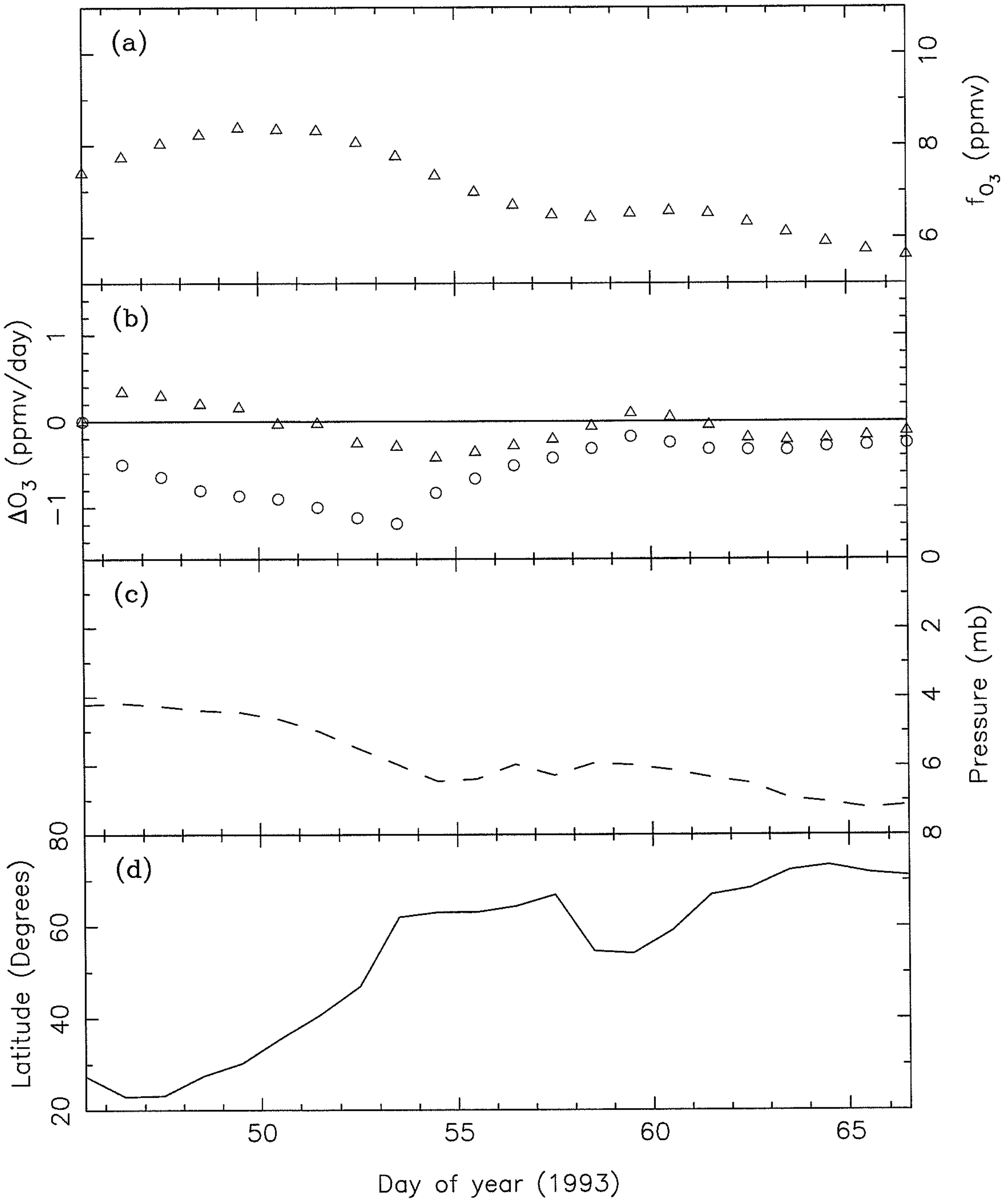

Figure 10. As Figure 6, but for the parcel ending at 960 K within the anomaly. The observed change in ozone is 1.78 ± 0.58 ppmv and the model change is -12.0 ppmv.

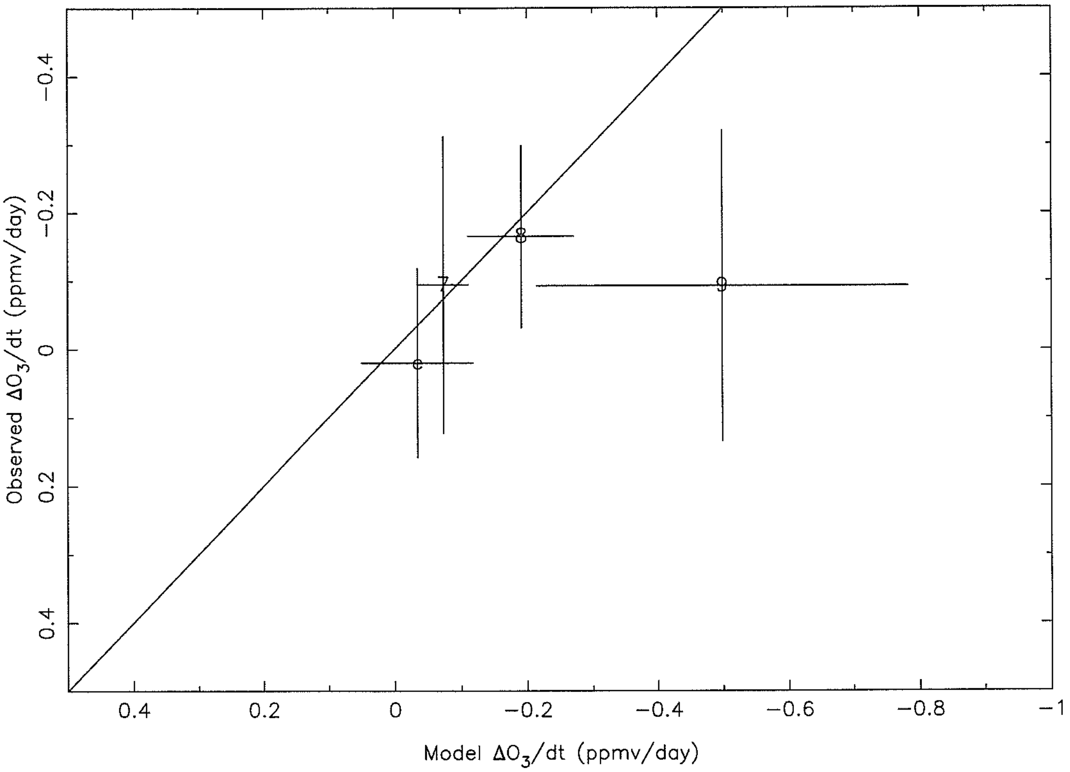

Figure 11. Scatter plot of average model vs. observed daily changes in ozone over the period of the trajectory. The solid line indicates exact agreement between model and observation. The symbols 7, 8, 9, or e indicate parcels ending at the 740, 840, 960, or external 840 K levels, respectively. The error bars extend out to one sample standard deviation in each direction.

libars altitude, and the model appears to predict reasonable changes in ozone below this altitude. However, as we have seen for all of the cases shown above, it is dangerous to draw quantitative conclusions from any one model run since there are many uncertainties. For example, individual trajectories may not properly describe the true air motion, particularly near the end of the back trajectory (day 45), or the initialization of species in the parcel may be wrong. Thus we must consider results along many different trajectories in order to minimize errors in individual cases.

We have run the chemistry along six trajectories in each of the 740, 840, 960, and external 840 K groups for the February/March 1993 event. Figure 11 is a plot of the predicted daily change in ozone against the observed daily change in ozone in each group for each of the 22 days over the trajectory period. Each group of trajectories has (6 trajectories) * (22 points/trajectory) = 132 points in it. We have plotted the average of the day-to-day changes for each group along with the sample standard deviation. Note that the predicted ozone decreases for parcels ending at 960 K are all much greater than the observed losses. The model also tends to overpredict ozone losses for the parcels which ended at the 840 K level outside the anomaly, but not to the severe degree shown for the 960 K parcels. Again, this is a relatively small sample size and more cases should be run before quantitative conclusions may be drawn. However, it does appear that the model consistently overpredicts ozone loss rates above the 840 K potential temperature level, or about 10 millibars in the polar regions.

6. Influence of vertical and latitudinal motion on ozone loss rates

A trajectory has three components, motion in longitude, motion in latitude, and motion in pressure. Since the motion in longitude is small over the course of a day, motion in latitude and pressure have a much larger impact on changing the radiation field, which in turn drives the processes which produce and destroy ozone. We have seen from the 960 K runs in the previous section that the pressure at which the parcel is located potentially has a large effect on the computed ozone loss rate. Thus it is worthwhile to distinguish the effects of motion in pressure and latitude on the loss rate of ozone.

We have performed a series of numerical experiments where we examine the effects of individually varying the pressure and latitude over the trajectory shown in the last section for the parcel ending at the 840 K level within the anomaly. In each model run, we either allow the pressure and/or latitude to vary according to the computed trajectory (shown in Figures 6c and 6d), or fix them to their initial values (6.82 millibars and 21.9° north, respectively). In these calculations we allow the model to compute the abundances of all species, including ozone, self-consistently. Since these are ficticious trajectories, it is not appropriate to assimilate measurements from the actual trajectory. The initialization is the same as in the previous section. The computed ozone mixing ratios and total change in ozone for each case are shown in Figure 12.

We see that allowing the pressure to vary over the range traversed by the parcel produces a negligible change in the ozone mixing ratio from the cases where the pressure is held fixed. However, allowing the latitude to vary produces a large change in ozone, comparable to the observed change along the actual trajectory. In each case, the mixing ratio of ozone in the parcel relaxes towards a photochemical equilibrium value, where production equals loss. This photochemical equilibrium value is to first order a function of latitude, with lower ozone abundances closer to the pole. This is due to the lower solar insolation, and hence lower oxygen photolysis, nearer the pole. In cases (a) and (b), where the latitude is fixed at 21.9°, the equilibrium value of ozone is about 8 ppmv. In cases (c) and (d), where the parcel rapidly moves northward and stays poleward of 60° for most of the last ten days, the equilibrium value is around 4 ppmv.

Figure 13 shows the calculated production and loss for each case. Notice that in all cases both production and loss at the beginning of the run, when the parcel is at low latitudes. In cases (c) and (d), production drops rapidly as the parcel moves to higher latitudes. The loss rate lags behind since it is to first order dependent upon the ozone concentration. The result is a net loss of ozone.

Thus if motion to high latitudes is the cause of the low ozone anomaly, why does air outside the anomaly at the same latitude have higher ozone mixing ratios?

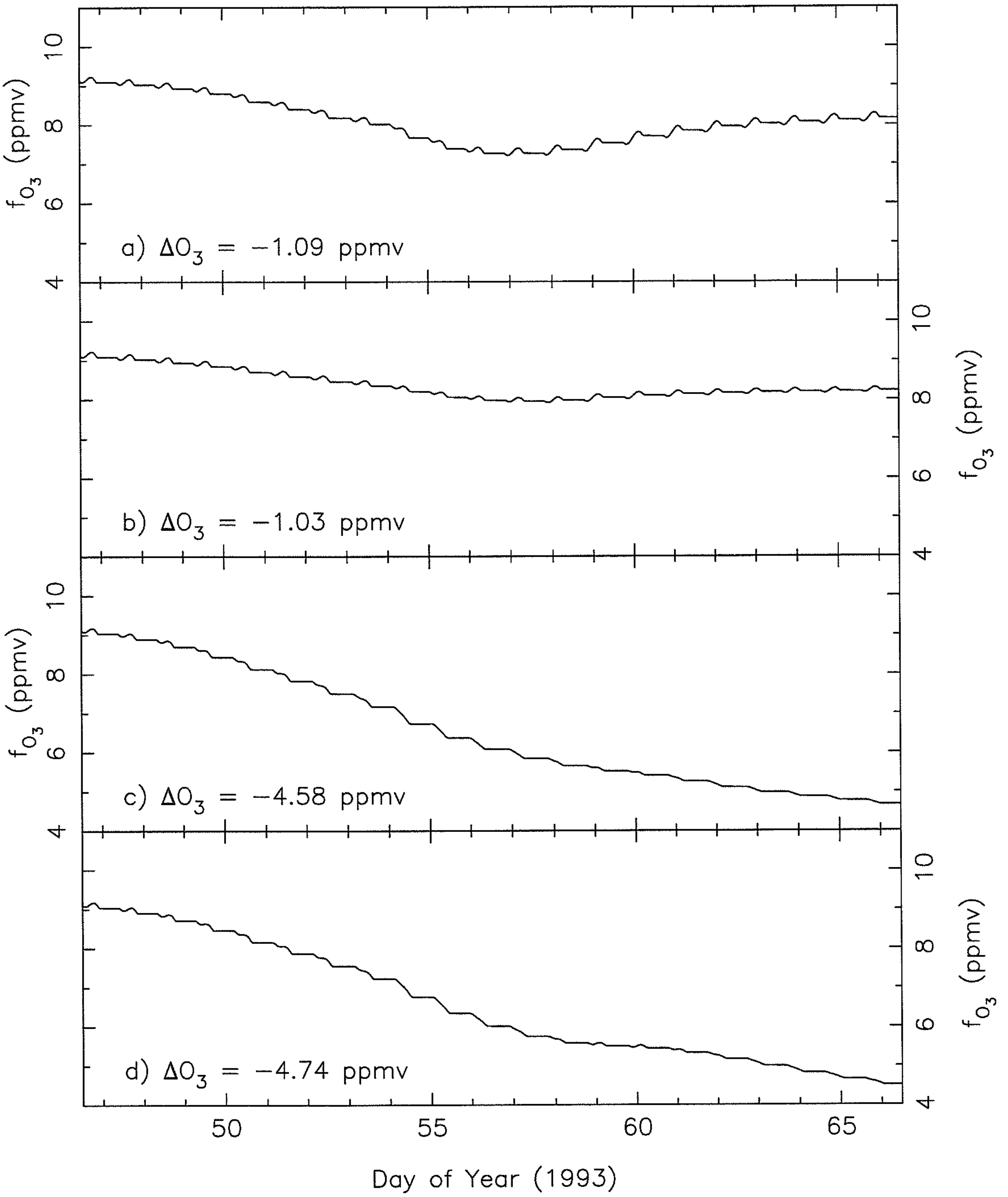

Figure 12. Computed ozone mixing ratios for four cases: (a) pressure = 6.82 millibars, latitude = 21.9°, (b) pressure varies according to Figure 6c, latitude = 21.9°, (c) pressure = 6.82 millibars, latitude varies according to Figure 6d, (d) vary pressure and latitude according to Figures 6c and 6d.

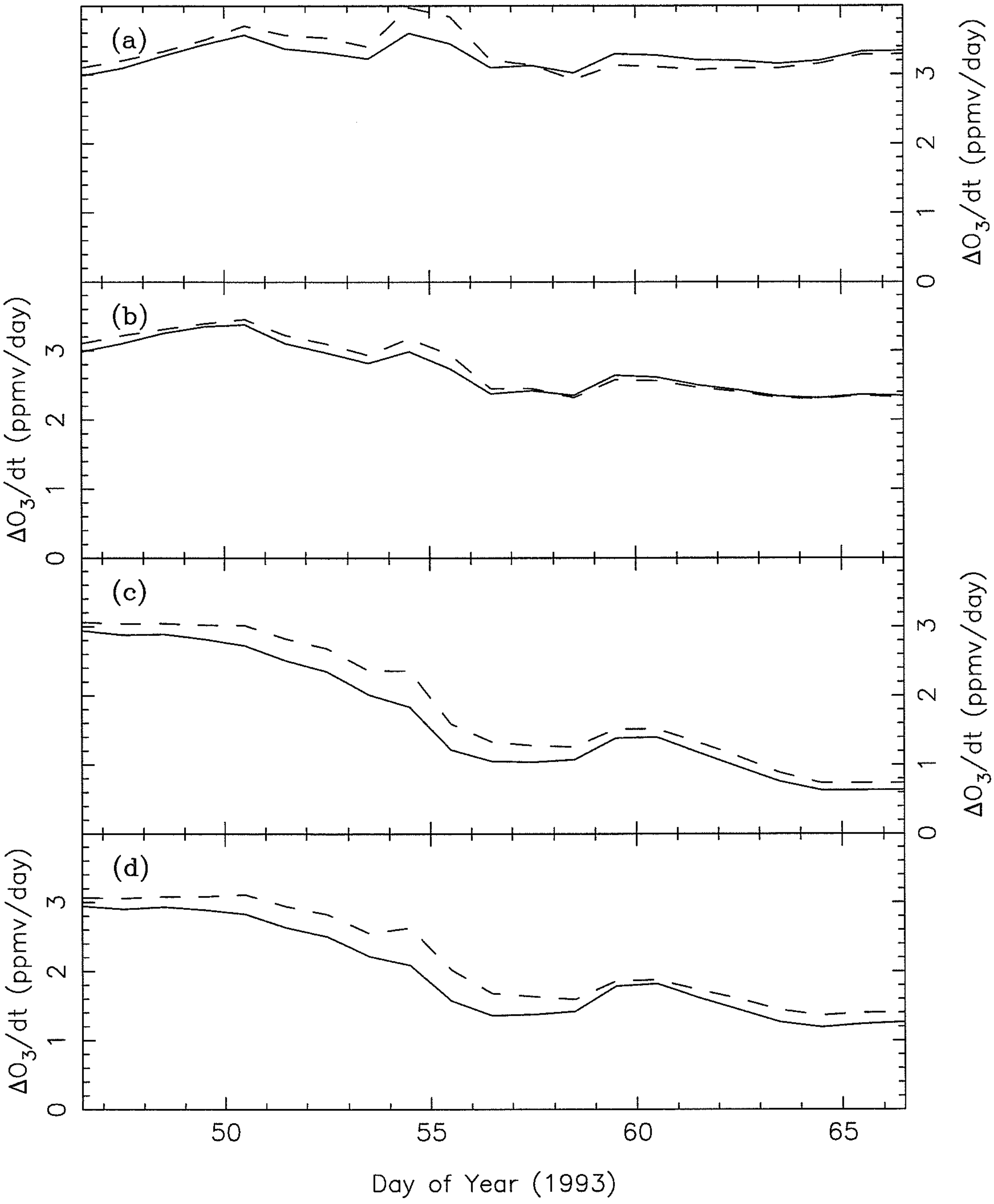

Figure 13. As figure 12, showing computed production (solid line) and loss (dashed line) of odd oxygen.

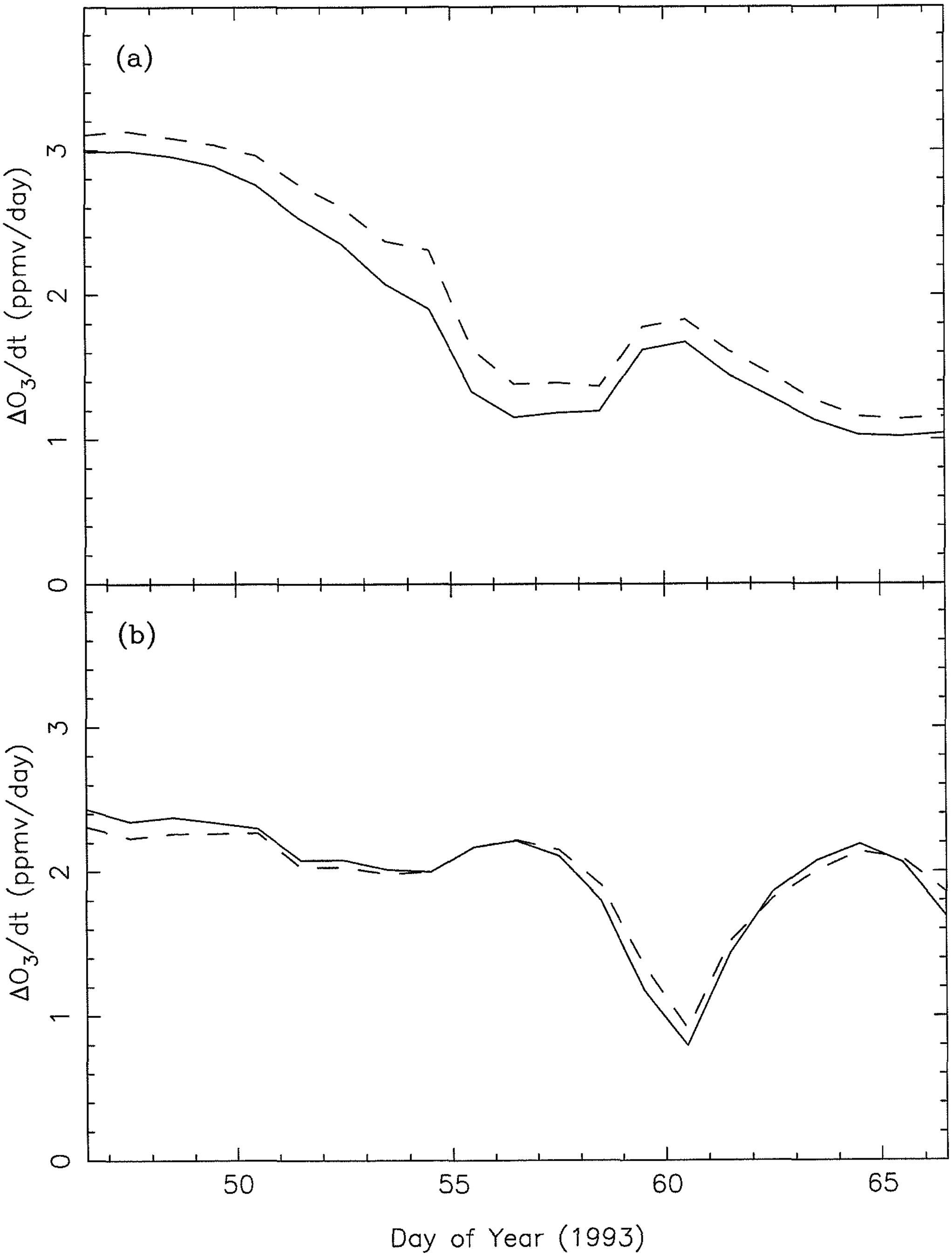

Figure 14. Production (solid line) and loss (dashed line) of odd oxygen for the two 840 K parcels: (a) parcel ending inside the anomaly, and (b) parcel ending outside.

Consider the two parcels ending at 840 K inside and outside the anomaly. From Figures 6 and 7, the parcels follow similar pressure paths, but very different latitude paths, although the final latitude is 71° north in each case. In particular, the parcel ending outside the anomaly swings between mid and high latitudes with a period of about a week. Figure 14 shows the computed production and loss for each of these two parcels. In each case, the production of odd oxygen is anti-correlated with proximity to the pole. The production and loss of odd oxygen for the parcel ending inside the anomaly are very similar to those shown in Figures 13c and d. The behavior of the production and loss for the parcel ending outside the anomaly is quite different from any of the cases we have considered thus far. When the parcel is at low latitudes, there is a slight net production of odd oxygen as the ozone concentration in the parcel is below the low latitude equilibrium value. Conversely, at high latitudes, there is a net loss of ozone. Since the parcel rapidly moves between these two regions, its ozone mixing ratio reflects a balance between the average production and loss over periods comparable to the lifetime of ozone, which is about 10 days at 35 km altitude (Ko *et al.* 1989).

7. The December 1992 event

A similar low ozone anomaly was seen in December 1992, although the latitude of formation was not as near the pole; the center of the anomaly was located at about 45° north as opposed to about 65° north latitude for the February/March 1993 event. Figure 15 shows observed vertical profiles of ozone inside the anomaly (179.5° east, 48° north) and outside the anomaly (234.5° east, 48° north) on December 24, 1992. Again, the ozone at the position of the anomaly has a low, sharp peak, and is considerably depleted relative to the external profile at the 10 millibar level.

The ozone loss rates along three trajectories both inside and outside the

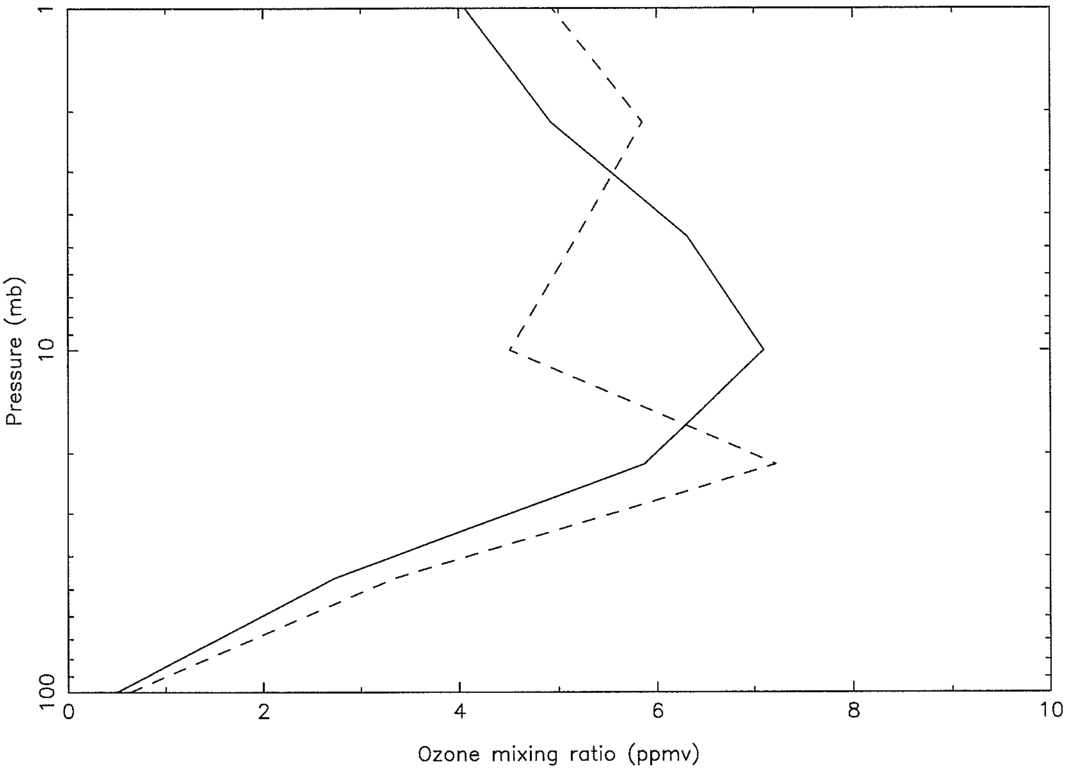

Figure 15. Ozone profiles inside (dashed line) and outside the anomaly (solid line) on December 24, 1992. Both profiles are at 48° north latitude.

anomaly were computed. Again, we follow trajectories ending at the 740, 840, and 960 K potential temperature levels within the anomaly (corresponding to 15.0, 10.6, and 7.0 millibars, respectively, on December 24) and one set of trajectories ending at the 840 K potential temperature level outside the anomaly (10.6 millibars). Figure 16 shows the calculated trajectories for three parcels ending inside the anomaly at 179.5° east longitude and 48° north latitude, and one parcel ending outside the anomaly at 234.5° east longitude, 48° north latitude at the 840 K level. The trajectories for this event are different than for the February/March 1993 event since although the air parcels reach latitudes northward of 60°, they are rapidly transported southward and stay close to 45° north latitude for the last week or so.

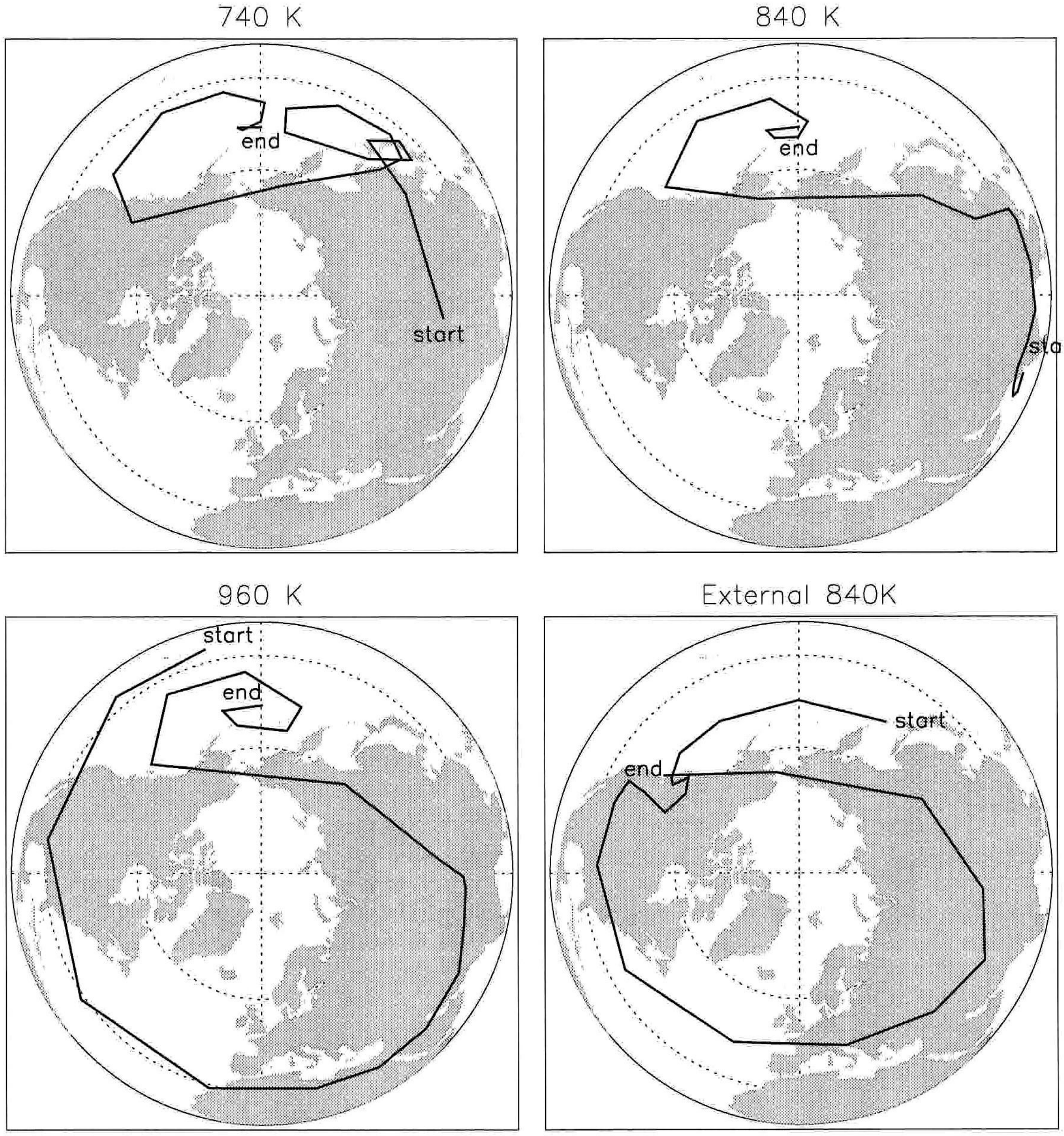
740 K

840 K

960 K

External 840K

Figure 16. Four sample trajectories for the December 1992 event. Parcels begin on December 3, 1992 and end on December 24, 1992.

Figure 17 summarizes the comparison between the observed daily changes in ozone with the model changes similar to Figure 11. Each group of trajectories contains 3*22 = 66 points. Again, the model prediction for the day-to-day ozone loss is far greater than the observations for parcels ending at the 960 K potential temperature level, although the discrepancy is not as great as for the February/March 1993 case.

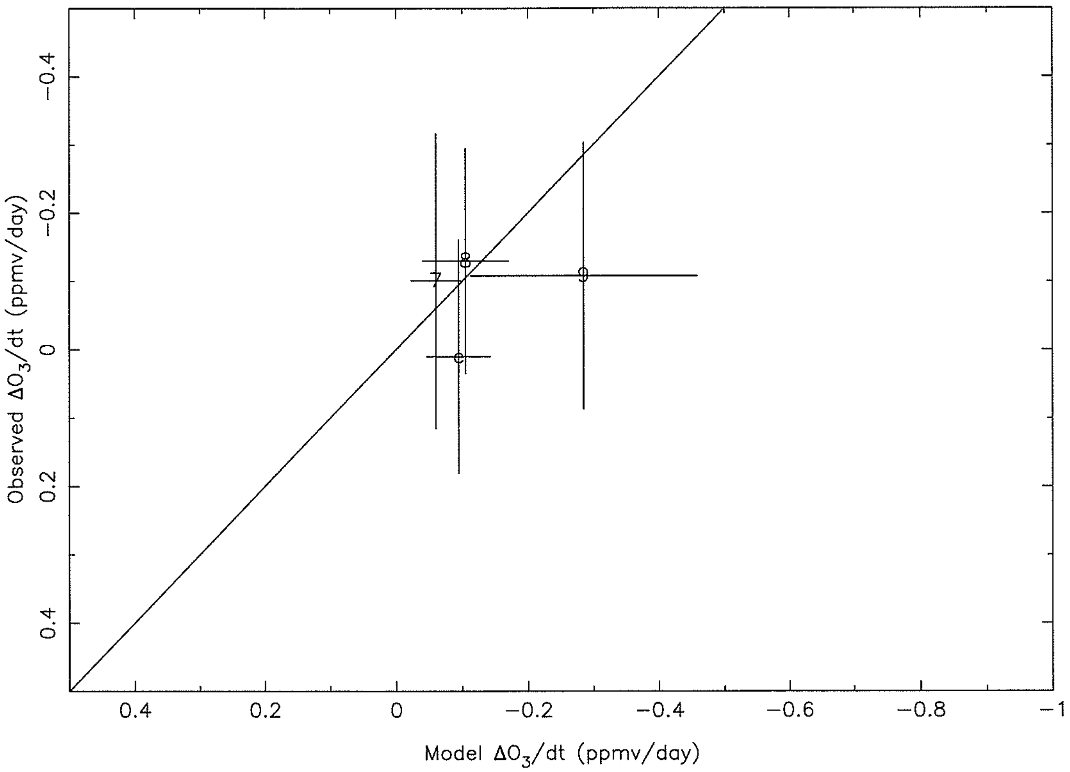

Figure 17. Scatter plot of average model vs. observed daily changes in ozone over the period of the trajectory. The solid line indicates exact agreement between model and observation. The symbols 7, 8, 9, or e indicate parcels ending at the 740, 840, 960, or external 840 K levels, respectively. The error bars extend out to one sample standard deviation in each direction.

This may be because this anomaly occurred close to the winter solstice. Although the final latitude is south of the latitude of the February/March anomaly, the solar insolation was smaller, hence leading to smaller values for both production and loss of odd oxygen. Thus the computed ozone deficit (loss minus production) is also smaller. Furthermore, the ozone mixing ratios in the anomaly over the period of the trajectory were lower than for the February/March 1993 event (Manney *et al.* 1995), which would also lead to smaller loss rates.

8. Conclusions

We have investigated the evolution of parcels of air along trajectories computed by Manney *et al.* (1995) leading to pockets of extra-vorticial, ozone poor air in the middle stratosphere in February/March 1993 and December 1992. These pockets of air occur in an altitude region where both dynamics and chemistry are important contributors to the ozone budget. In order to separate the dynamical and chemical sources of ozone in this altitude region, we use a Lagrangian photochemical model. Observations of trace species from the Microwave Limb Sounder (MLS) and the Cryogenic Limb Array Etalon Spectrometer (CLAES) aboard the Upper Atmosphere Research Satellite (UARS) were incorporated into the model to better define the species which are important in determining ozone loss.

We consider four groups of trajectories in each event; three end at the longitude and latitude of the low ozone anomaly at the 740, 840, and 960 K potential temperature levels, and the last ends at the latitude of the anomaly at the 840 K potential temperature level but at a different longitude, where the ozone mixing ratio is more representative of the zonal mean. We have modeled the chemical evolution of six distinct parcels in each group for February/March 1993, and three parcels in each group for December 1992.

Trajectory calculations for the two sample cases indicate that the air in the low ozone pockets originated in the tropics, where ozone values are high. These parcels of air rapidly move northward and are held at high northern latitudes for extended periods of time. Since the photolysis rate of oxygen at high latitudes in winter is small, the ozone mixing ratio falls to low values in order for the loss rate to balance the production of odd oxygen. Air outside of these pockets and the vortex typically swings back and forth between mid and high latitudes such that the average production rate of odd oxygen is high relative to air in the low ozone bubble. Thus the steady-state ozone mixing ratio for this "normal" air is higher than the mixing ratios found in the vortex and the low ozone anomalies. These findings agree with the conclusions of Morris *et al.* (1995).

The results are qualitatively similar for each event. We find that the photochemical model consistently overestimates the loss rate for ozone at pressures less than about 7 millibars. This is a region of the atmosphere where models have historically overpredicted ozone loss rates relative to production (the "ozone deficit"). The model prediction for ozone loss is in much better agreement with the observations at pressures above 10 millibars. If the trajectories we follow are valid, this indicates that current photochemical models may not account for some process which operates at higher altitudes that produces odd oxygen (or conversely, destroys it less efficiently) that does not operate at lower altitudes.

References

ALLEN, M., J.I. LUNINE, AND Y.L. YUNG 1984. The vertical distribution of ozone in the mesosphere and lower thermosphere. *J. Geophys. Res.* **89,** 4841–4872.

ALLEN, M., AND M.L. DELITSKY 1991. Inferring the abundances of ClO and HO_2 from Spacelab 3 Atmospheric Trace Molecule Spectroscopy Observations. *J. Geophys. Res.* **96,** 2913–2919.

AUSTIN, J., R.C. PALLISTER, J.A. PYLE, A.F. TUCK, A.M. ZAVODY 1987. Photochemical model comparisons with LIMS observations in a stratospheric trajectory coordinate system. *Q. J. R. Meteorol. Soc.* **113,** 361–392.

BARATH, F.T., M.C. CHAVEZ, R.E. COFIELD, D.A. FLOWER, M.A. FRERKING, M.B. GRAM, W.M. HARRIS, J.R. HOLDEN, R.F. JARNOT, W.G. KLOEZEMAN, G.J. KLOSE, G.K. LAU, M.S. LOO, B.J. MADDISON, R.J. MATTAUCH, R.P. MCKINNEY, G.E. PECKHAM, H.M. PICKETT, G. SIEBES, F.S. SOLTIS, R.A. Suttie, J.A. Tarsala, J.W. Waters, and W.J. Wilson 1993. The Upper Atmosphere Research Satellite Microwave Limb Sounder Instrument. *J. Geophys. Res.* **98**, 10751–10762.

Brasseur, G., and S. Solomon 1986. *Aeronomy of the middle atmosphere, second edition*, D. Reidel, Dordrecht, Holland.

Callis, L.B., M. Natarajan, R.E. Boughner, J.M. Russell III, and J.D. Lambeth 1986. Stratospheric photochemical studies using Nimbus 7 data: 2. Development of inferred trace specie distributions. *J. Geophys. Res.* **91**, 1167–1197.

Chance, K., W.A. Traub, D.G. Johnson, K.W. Jucks, P. Ciarpallini, R.A. Stachnik, R.J. Salawitch, and H.A. Michelson 1995. Simultaneous measurements of stratospheric HO_x, NO_x, and Cl_x : Comparison with a photochemical model. Submitted to *J. Geophys. Res.*

Crutzen, P.J., and U. Schmailzl 1983. Chemical budgets of the stratosphere. *Planet. Sp. Sci.* **31**, 1009–1032.

Crutzen, P.J., J.-U. Grooß, C. Brühl, R. Müller, and J.M. Russell III 1995. A reevaluation of the ozone budget with HALOE UARS data: No evidence for the ozone deficit. *Science* **268**, 705–708.

DeMore, W.B., S.P. Sander, D.M. Golden, R.F. Hampson, M.J. Kurylo, C.J. Howard, A.R. Ravishankara, C.E. Kolb, and M.J. Molina 1994. *Chemical Kinetics and Photochemical Data for Use in Stratospheric Modeling, Evaluation Number 11*, JPL Publication 94-26.

Elson, L.S., and L. Froidevaux 1993. The use of Fourier transforms for asynoptic mapping: Early results for the Upper Atmosphere Research Satellite Microwave Limb Sounder. *J. Geophys. Res.* **98**, 23039–23049.

ELUSZKIEWICZ, J.E. AND M. ALLEN 1993. A global analysis of the ozone deficit in the upper stratosphere and lower mesosphere. *J. Geophys. Res.* **98,** 1069–1082.

FAHEY, D.W., S. SOLOMON, S.R. KAWA, M. LOEWENSTEIN, J.R. PODOLSKE, S.E. STRAHAN, AND K.R. CHAN 1990. A diagnostic for denitrification in the winter polar stratospheres. *Nature* **345,** 698–702.

FROIDEVAUX, L., M. ALLEN, S. BERMAN, AND A. DAUGHTON 1989. The mean ozone profile and its temperature sensitivity in the upper stratosphere and lower mesosphere: An analysis of LIMS observations. *J. Geophys. Res.* **94,** 6389–6417.

FROIDEVAUX, L., W.G. READ, T.A. LUNGU, R.E. COFIELD, E.F. FISHBEIN, D.A. FLOWER, R.F. JARNOT, B.P. RIDENOURE, Z. SHIPPONY, J.W. WATERS, J.J. MARGITAN, I.S. MCDERMID, AND R.A. STACHNIK 1995. Validation of UARS MLS Ozone Measurements. *J. Geophys. Res.*, in press.

GARCIA, R.R., AND S. SOLOMON 1983. A numerical model of the zonally averaged dynamical and chemical structure of the middle atmosphere. *J. Geophys. Res.* **88,** 1379–1400.

JACKMAN, C.H., R.S. STOLARSKI, AND J.A. KAYE 1986. Two-dimensional monthly average ozone balance from Limb Infrared Monitor of the Stratosphere and Stratospheric and Mesospheric Sounder data. *J. Geophys. Res.* **91,** 1103–1116.

JOHNSTON, H.S., AND J. PODOLSKE 1978. Interpretations of stratospheric chemistry. *Rev. Geophys. Space Phys.* **16,** 491–519.

JONES, R.L., D.S. MCKENNA, L.R. POOLE, AND S. SOLOMON 1990. On the influence of polar stratospheric cloud formation on chemical composition during the 1988/89 Arctic winter. *Geophys. Res. Lett.* **17,** 545-548.

JUCKS, K.W., D.G. JOHNSON, K.V. CHANCE, W.A. TRAUB, R.J. SALAWITCH, AND R.A. STACHNIK 1995. Ozone production and loss rate measurements in the middle stratosphere. Submitted to *Science*

KAWA, S.R., D.W. FAHEY, J.C. WILSON, M.R. SCHOEBERL, A.R. DOUGLASS, R.S. STOLARSKI, E.L. WOODBRIDGE, H. JONSSON, L.R. LAIT, P.A. NEWMAN, M.H. PROFFITT, D.E. ANDERSON, M. LOEWENSTEIN 1993. Interpretation of NO_x/NO_y observations from AASE-II using a model of chemistry along trajectories. *Geophys. Res. Lett.* **20**, 2507–2510.

KO, M.K.W., N.D. SZE, AND D.K. WEISENSTEIN 1989. The roles of dynamical and chemical processes in determining the stratospheric concentration of ozone in one-dimensional and two-dimensional models. *J. Geophys. Res.* **94**, 9889–9896.

KUMER, J.B., J.L. MERGENTHALER, A.E. ROCHE, R.W. NIGHTINGALE, J.C. GILLE, S.T. MASSIE, P.L. BAILEY, M.R. GUNSON, M.C. ABRAMS, G.C. TOON, B. SEN, J.-F. BLAVIER, R.A. STACHNIK, C.R. WEBSTER, D.G. MURCRAY, F.H. MURCRAY, A. GOLDMAN, W.A. TRAUB, K.W. JUCKS, AND D.G. JOHNSON 1995. Comparison of correlative data with nitric acid data version v0007 from the Cryogenic Limb Array Etalon Spectrometer (CLAES) instrument deployed on the NASA Upper Atmosphere Research Satellite (UARS). *J. Geophys. Res.*, in press.

LAHOZ, W.A, M.R. SUTTIE, L. FROIDEVAUX, R.S. HARWOOD, C.L. LAU, T.A. LUNGU, G.E. PECKHAM, H.C. PUMPHREY, W.G. READ, Z. SHIPPONY, R.A. SUTTIE, J.W. WATERS 1995. Validation of UARS MLS 183 GHz H_2O Measurements. *J. Geophys. Res.*, in press.

MANNEY, G.L., L. FROIDEVAUX, J.W. WATERS, R.W. ZUREK, J.C. GILLE, J.B. KUMER, J.L. MERGENTHALER, A.E. ROCHE, A. O'NEILL, AND R. SWINBANK 1995. Formation of low ozone pockets in the middle stratospheric anticyclone during winter. *J. Geophys. Res.* **100**, 13939–13950.

McElroy, M.B., and R.J. Salawitch 1989. Stratospheric ozone: Impact of human activity. *Planet. Sp. Sci.* **37**, 1653–1672.

Mergenthaler, J.L., J.B. Kumer, A.E. Roche, R.W. Nightingale, J.F. Potter, J.C. Gille, S.T. Massie, P.L. Bailey, D. Edwards, P.S. Connell, D.E. Kinnison, M.R. Gunson, M.C. Abrams, G.C. Toon, B. Sen, J.-F. Blavier, D.G. Murcray, F.J. Murcray, and A. Goldman 1995. Validation of CLAES $ClONO_2$ measurements. *J. Geophys. Res.*, in press.

Michelson, H.A., R.J. Salawitch, M.R. Gunson, C. Aellig, N. Kaempfer, M.M. Abbas, M.C. Abrams, T.L. Brown, A.Y. Chang, A. Goldman, F.W. Irion, M.J. Newchurch, C.P. Rinsland, G.P. Stiller, and R. Zander 1995. Stratospheric chlorine partitioning: Constraints from shuttle-borne measurements of HCl, $ClNO_3$, and ClO. Submitted to *Geophys. Res. Lett.*

Morris, G.A., S.R. Kawa, A.R. Douglass, M.R. Schoeberl, L. Froidevaux, and J. Waters 1995. Chemical modeling of mid-stratospheric, low ozone pockets. Submitted to *J. Geophys. Res.*

Natarajan, M., L.B. Callis, R.E. Boughner, and J.M. Russell III 1986. Stratospheric photochemical studies using Nimbuus 7 data: 1. ozone photochemistry. *J. Geophys. Res.* **91**, 1153–1166.

Plumb, R.A, and M.K.W. Ko 1992. Interrelationships between mixing ratios of long lived stratospheric constituents. *J. Geophys. Res.* **97**, 10145–10156.

Reber, C.A., C.E. Trevathan, R.J. McNeal, and M.R. Luther 1993. The Upper Atmosphere Research Satellite (UARS) Mission. *J. Geophys. Res.* **98**, 10643–10647.

Roche, A.E., J.B. Kumer, J.L. Mergenthaler, G.A. Ely, W.G. Uplinger, J.F. Potter, T.C. James, and L.W. Sterritt 1993. The Cryogenic Limb Array Etalon Spectrometer (CLAES) on UARS: Experiment Description and Performance. *J. Geophys. Res.* **98**, 10763–10775.

Roche, A.E., J.B. Kumer, R.N. Nightingale, J.L. Mergenthaler, P.L. Bailey, S.T. Massie, J.C. Gille, M.R. Gunson, M.C. Abrams, G.C. Toon, C.R. Webster, W.A. Traub, K.W. Jucks, D.G. Johnson, R. de Zafra, D.G. Murcray, F.H. Murcray, and A. Goldman 1995. Validation of CH_4 and N_2O measurements by the CLAES instrument on the Upper Atmosphere Research Satellite.. *J. Geophys. Res.*, in press.

Siskind, D.E., B.J. Connor, R.S. Eckman, E.E. Remsberg, J.J. Tsou, and A. Parrish 1995. An intercomparison of model ozone deficits in the upper stratosphere and mesosphere from two data sets. *J. Geophys. Res.* **100**, 11191–11201.

Stachnik, R.A., J.C. Hardy, J.A. Tarsala, J.W. Waters, and N.R. Erickson 1992. Submillimeterwave heterodyne measurements of stratospheric ClO, HCl, O_3, and HO_2 : First results. *Geophys. Res. Lett.* **19**, 1931–1934.

Waters, J.W., W.G. Read, L. Froidevaux, T.A. Lungu, V.S. Perun, R.A. Stachnik, R.F. Jarnot, R.E. Cofield, E.F. Fishbein, D.A. FLower, J.R. Burke, J.C. Hardy, L.L. Nakamura, B.P. Ridenoure, Z. Shippony, R.P. Thurstans 1995. Validation of UARS MLS ClO Measurements. *J. Geophys. Res.*, in press.

Woodbridge, E.L., J.W. Elkins, D.W. Fahey, L.E. Heidt, S. Solomon, T.J. Baring, T.M. Gilpin, W.H. Pollock, S.M. Schauffler, E.L. Atlas, M. Loewenstein, J.R. Podolske, C.R. Webster, R.D. May, J.M.

GILLIGAN, S.A. MONTZKA, K.A. BOERING, AND R.J. SALAWITCH 1994. Estimates of total organic and inorganic chlorine in the lower stratosphere from in situ and flask measurements during AASE II. *J. Geophys. Res.*, in press.